An Investigation of Challenges in High Current Density CO_2 Electrolysis to Ethylene

Ph.D. Thesis by:

Asger Barkholt Moss

Supervisors:

Prof. Brian Seger
Prof. Ib Chorkendorff

Department of Physics
Technical University of Denmark

November 2022

This page intentionally left blank.

Abstract

This Ph.D. thesis investigates some of the challenges in electrochemical CO_2 Electrolysis (CO_2E), a promising technology allowing a sustainable production of hydrocarbons such as ethylene (C_2H_4). The primary focus has been on the cathode reactions, and includes an attempt of up scaling an aqueous synthesis method for $\{1\,0\,0\}$ faceted Cu Nano Particles (NP).

The work also included the design and construction of a setup for elevated temperature and pressurised experiments. These experiments show that the selectivity for CO is increases at high temperature. Pressurised CO_2E experiments at $5\,\mathrm{bar}$ did not show a large increase in selectivity for C_2H_4.

The thesis further covers a range of galvanostatic Wide Angle X-ray Scattering (WAXS) operando experiments investigating the cathode Gas Diffusion Electrode (GDE). Crystalline salt precipitations and electrolyte flooding was detected in the GDE. Salt precipitations were seen to correlate with oscillating behaviour in both potential and selectivity, and is explained by salt precipitations blocking the pores of the GDE. A following temporary flooding was seen to dissolve the salt precipitation and blockage, causing the oscillating behaviour. Experiments with CO electrolysis did not show similar oscillations and salt precipitation.

Finally, it is investigated if an ohmic resistance in the cathode GDE causes a drag of cations away from the membrane, and thereby worsening the salt precipitation, but this was inconclusive.

These findings and the better understanding of how salt precipitations in the GDE causes instability can be important in the further development of CO_2E as a technology.

Resumé

Denne ph.d. afhandling undersøger nogle af de udfordringer der er i elektrokemisk CO_2-elektrolyse, en lovende teknologi, der muliggør en bæredygtig produktion af kulbrinter såsom ethylen (C_2H_4). Det primære fokus har været på katodereaktionerne og omfatter et forsøg på at opskalere en vandig syntesemetode for $\{1\,0\,0\}$ facetteret Cu nanopartikler.

Arbejdet omfattede også designet og konstruktion af et setup, der muliggjorde eksperimenter ved øget temperatur og tryk. Disse eksperimenter viste, at selektiviteten mod CO stiger ved høj temperatur. Eksperimenter ved $5\,\mathrm{bar}$ viste ikke en synderlig stigning i selektiviteten for C_2H_4.

Afhandlingen omhandler desuden en række operando røngten spredning forsøg ved galvanostatisk, hvori katode gas-diffusions-elektroden undersøges under galvanostatisk elektrolyse. Krystallinske saltudfældninger og elektrolytoversvømmelser i gas-diffusions-elektroden blev observeret. Saltudfældningerne korrelere med oscillationer i både potentiale og selektivitet, og forklares ved at salt blokerer porerne i gas-diffusionselektroden hvilket forhindrer CO_2 diffusion til katalysatoren. En efterfølgende kortvarig oversvømmelse af elektroden blev observeret, hvilket opløser saltet og dermed blokeringen. Dette forklarer oscillationerne i potentiale og selektivitet. CO-elektrolyse eksperimenter viste ikke tegn på lignende oscillationer eller saltudfældning.

Til sidst undersøges det, om en ohmsk modstand i katode gas-diffusionelektroden forårsager et træk af kationer væk fra membranen, og derved forværrer udfældningen af salt, resultatet var ikke entydigt.

De samlede fund, og den bedre forståelse af hvordan saltudfældninger i gas-diffusions-elektroden forårsager en ustabilitet, kan være vigtige i den videre teknologiske udvikling af CO_2-elektrolyse.

Preface & Acknowledgement

The work for this thesis was carried out at The Technical University of Denmark, Department of Physics, Section of Surface Physics and Catalysis (SurfCat) between October 2019 and November 2022.

I want to thank my supervisors Professor Brian Seger and Professor Ib Chorkendorff for their guidance and good advices, and their patience when I did not follow them. My Ph.D. was part of the EcoEthylene project (Innovation fund Denmark), and I would like to thank the other partners in the project at IRD Fuelcells and DTU Energy for a good collaboration. The Covid-19 pandemic caused a change of plans, so I ended up doing my external research stay at The European Synchrotron Radiation Facility beamline ID31. Through countless zoom meetings, two beam times and a short stay, I got a taste of what its like to work at a beamline. For that I would like to thank all of the staff at ID31, especially postdoc Marta Mirolo and Beamline Scientist Jakub Drnec, who ended up playing a very important role for my time as a Ph.D. student. You all provided me with valuable knowledge and insight of X-ray Scattering and synchrotron operation, as well as memorable stays in Grenoble.
I would like to thank all the people at Surfcat. Especially the scientific floor managers Brian Peter Knudsen, Jakob Ejler Sørensen, and former floor manager Patrick Strøm-Hansen, as well as Jacqueline McAnulty and Birgit Bohn for all their help, and for ensuring that SurfCat is always running. I would like to thank my family and close friends, especially Matias, for bearing with me, and all my complaints about the GC throughout the COVID lockdown. There is no doubt that the last three years has been some of the most strange, hard and frustrating days of my life, but it has also been some of the most rewarding and fun times. Especially because of my colleagues in the CO2 reduction group. Dr. Ming Ma for being a great office mate the first year. Dr. Ezra Lee Clark and Dr. Gastón O. Larrazábal for introducing me to CO_2 reduction. Degenhart Hochfilzer, Yu Qiao, Bjørt Óladóttir Joensen, Francesco Longhin and Clara Bruun Jensen[1] for being awesome colleagues, together with Dr. Wanyu Deng and Tuğçe Yılmaz who were also some of the best officemates one can have. A special thanks goes to Dr. Qiucheng Xu, Dr. Sahil Garg and Carlos Andres Giron Rodriguez for some great trips to Grenoble. Sahil and Carlos, you have not only been close colleges, but also good friends, Thank you!

[1] Yes, I did mention you.

List of Publications Related to the Thesis

Paper 1, in appendix

Versatile high energy X-ray transparent electrolysis cell for operando measurements

Asger Barkholt Moss, Joel Hätinen, Peter Kúš, Sahil Garg, Marta Mirolo, Ib Chorkendorff, Brian Seger, Jakub Drnec
Submitted, 2022
Presented as published on ChemRxiv,
doi:10.26434/chemrxiv-2022-7v75p-v2[1]

Paper 2, in appendix

In Operando investigations of oscillatory water and carbonate effects in MEA-based CO2 electrolysis devices

Asger B. Moss*, Sahil Garg*, Marta Mirolo, Carlos A. Giron Rodriguez, Roosa Ilvonen, Ib Chorkendorff, Jakub Drnec, Brian Seger
Submitted, 2022
Presented as published on ChemRxiv,
doi:10.26434/chemrxiv-2022-54ccs[2]

**Shared first author*

Paper 3

Influence of headgroups in ETFE-based radiation-grafted anion exchange membranes for CO2 electrolysis

Carlos A. Girón Rodriguez, Bjørt Óladottir Joensen, Asger Barkholt Moss, Gastón Larrazabal, Daniel K. Whelligan, Brian Seger, John R. Varcoe, Terry R. Willson
Submitted, 2022

Paper 4

Enriching Surface-Accessible CO_2 in the Zero-Gap Anion-Exchange-Membrane-Based CO_2 Electrolyzer

Qiucheng Xu, Aoni Xu, Sahil Garg, Asger Barkholt Moss, Ib Chorkendorff, Thomas Bligaard, Brian Seger
Accepted in Angew. Chem. Int. Ed.2022, e202214383

Paper 5

How alkali cations affect salt precipitation and CO_2 electrolysis performance in membrane electrode assembly electrolyzers

Sahil Garg*, Qiucheng Xu*, Asger Barkholt Moss, Marta Mirolo, Wanyu Deng, Ib Chorkendorff, Jakub Drnec, Brian Seger
Submitted, 2022

**Shared first author*

Contents

1 Introduction **1**
- 1.1 Introduction to CO_2E . . . 3
  - 1.1.1 Fundamentals of Electrochemical CO_2R . . . 3
    - 1.1.1.1 Current & Potentials . . . 3
    - 1.1.1.2 Catalyst(s) for CO_2R . . . 5
    - 1.1.1.3 Reaction Mechanism & Influence of Local Environment . . . 6
    - 1.1.1.4 Increasing Current Density . . . 8
    - 1.1.1.5 Types of Electrolysis Cells . . . 8
    - 1.1.1.6 The MEA Cell . . . 9
- 1.2 Scope and Outline . . . 10

2 Large Scale Catalysts Synthesis **11**
- 2.1 Chapter Introduction . . . 13
- 2.2 The Original Synthesis Method . . . 13
  - 2.2.1 Growth Mechanism . . . 14
- 2.3 Initial Small Scale Tests . . . 15
  - 2.3.1 Importance of Uniform Reaction Temperature . . . 15
  - 2.3.2 Headspace in Vials . . . 15
  - 2.3.3 Effect of Stirring Rate . . . 16
- 2.4 Large Scale Synthesis . . . 17
  - 2.4.1 Designing the Large Scale Synthesis System . . . 17
  - 2.4.2 Large Scale Batch#1 . . . 20
  - 2.4.3 Effect of Temperature . . . 21
  - 2.4.4 Test of Gas Diffusion Electrodes . . . 25
  - 2.4.5 Terminating the Project . . . 25

3 The Setup & Initial Experiments **27**
- 3.1 Chapter Introduction . . . 29
- 3.2 The Standard MEA and Cell Assembly . . . 29

3.3 The Basic Setup . . . 30
3.3.1 Ag Tests . . . 32
3.4 Various Causes of Low Performance . . . 34
3.4.1 Mechanical Failure . . . 34
3.4.2 Metal Contamination . . . 35
3.5 CA vs. CP & Ref. Electrode Position . . . 36
3.5.1 CA vs. CP . . . 36
3.5.2 Selectivity Dependence on Current . . . 38
3.6 The Gas Supply System . . . 38
3.7 Humidification of CO_2 . . . 39
3.7.1 Pressure Effects from the Humidifier . . . 40
3.8 Measuring the Outlet Flow . . . 42
3.8.1 Internal N_2 Flow Reference . . . 43
3.9 Heating the System . . . 45
3.9.1 First Heated Experiment . . . 46
3.10 PTFE Based GDE . . . 47
3.11 Pressurising the Setup . . . 48
3.11.1 Heated and Pressurised Experiments . . . 48
3.12 New Back Pressure Regulators . . . 50

4 X-ray Cell & Data Analysis 51
4.1 Chapter Introduction . . . 53
4.2 Designing a Cell for X-ray Experiments . . . 54
4.2.1 Improvements to Initial Design . . . 55
4.2.2 Grazing Incident Geometry . . . 56
4.2.3 Alignment . . . 57
4.2.4 Peak Split from Parallax Effect . . . 59
4.3 Analysing Large Operando WAXS Datasets . . . 60
4.3.1 Detecting Water with WAXS . . . 61
4.3.1.1 Separating Salt & Electrolyte Content . . . 62

5 First Synchrotron Beamtime 63
5.1 Chapter Introduction . . . 65
5.2 In Situ Study of Cu_2O Reduction . . . 65
5.3 Operando WAXS Experiments . . . 66
5.3.1 Mechanism of Cyclic Behaviour . . . 72
5.4 Chapter Conclusion . . . 74

6 Second Synchrotron Beamtime **75**
6.1 Chapter Introduction . . . 76
6.2 Variation in Cations . . . 77
6.2.1 $LiHCO_3$ . . . 78
6.2.2 $NaHCO_3$ . . . 80
6.2.3 $CsHCO_3$ . . . 82
6.3 Double Membrane Experiments . . . 84
6.4 COE Experiments . . . 86
6.4.1 Double Membrane COE . . . 88
6.4.2 Higher PTFE Containing GDE . . . 90
6.5 Stability of Cu Layer . . . 92
6.6 Chapter Conclusion . . . 93

7 Cation Movement in the GDE **95**
7.1 Chapter Introduction . . . 97
7.2 Internal E-field in the GDE . . . 98
7.3 Cu Felt as GDE . . . 99
7.4 Short-circuiting the GDL . . . 101
7.5 All Metal Cell Test . . . 104
7.6 Chapter Discussion & Conclusion . . . 105

8 New Cell & Final Experiments **107**
8.1 Chapter Introduction . . . 109
8.2 Cell Design . . . 109
8.2.1 Pressure Testing the Cell . . . 110
8.3 Two Ref. at High Pressure . . . 112
8.3.1 $65\,^{\circ}\mathrm{C}\ 5\,\mathrm{bar}$ . . . 112
8.3.2 $50\,^{\circ}\mathrm{C}\ 5\,\mathrm{bar}$ . . . 114
8.3.3 Unheated 5 bar . . . 115
8.4 Chapter Discussion & Conclusion . . . 116

9 The Anode **117**
9.1 Chapter Introduction . . . 119
9.2 Standard Anode not Viable for Industrial Use . . . 119
9.2.1 Dissolving of the Anode . . . 119
9.3 Requirements for an Industrial Anode . . . 120

10 Final Conclusion & Outlook **121**

References **123**

Acronyms **128**

Symbols **133**

Constants **135**

A Design of Gas Chromatograph for CO_2E **137**
A.1 GC Configuration 137
A.2 In-line Operation & Injection 138
A.3 Flame Ionisation Detector 138
A.3.1 Column 139
A.3.2 Methanizer 139
A.4 Thermal Conductivity Detector 140
A.4.1 Columns 140
A.5 Timing and Carrier Gas Flow 141

B Appended Papers **143**
B.1 Paper 1 143
B.2 Paper 2 163

This page intentionally left blank.

Chapter 1

Introduction

It becomes still more evident that the modern worlds consumption and dependency on fossil resources is unsustainable, whether due to global warming caused by CO_2 emissions, geopolitical issues or diminishing reserves. We must find sustainable alternatives, and the transition away from fossil fuels seems unavoidable. Most of the worlds oil, gas and coal consumption goes into energy purposes, but a fairly large part ($22\,\%$[3]) is used in the production of petrochemicals. It has been estimated that 4 to $8\,\%$ of worlds oil production goes to the production of plastic. Where around half is used as fuel in the production, and the rest as material feedstock[4]. The plastic production is expected to increase and in 2050 it might as much as $20\,\%$ of the worlds oil production that is used for plastic production. Clearly large part of the modern world is based on plastics, for good and bad. It is obvious that we must prevent the spreading of plastics in the oceans and in nature, in my opinion a modern world without plastic is an utopia. It might be possible to find alternative solutions for food wrapping, plastic straws etc., but plastic is also heavily used in the medical industry, for electronics, and in infrastructure, e.g. insulation of electrical cables.

We need a sustainable, ie. non fossil based, feedstock for plastics and here I see two viable options. The first, and perhaps most mature option is electrochemical production of hydrogen, ie. water electrolysis followed by a thermal catalytic reaction with CO_2 into long hydrocarbon chains eg. through the Fischer-Tropsch process. The alternative is what can be described as direct CO_2 electrolysis where CO_2 is electrochemically reduced and hydrogenated into hydrocarbons.

The ongoing worldwide inflation driven by increased energy prises has clearly shown that price matters. The price level for renewable chemicals

must therefore be comparable to current prices. And here it is interesting to pursue the direct CO_2E.
The largest chemical used in plastic production is ethylene. The focus in this thesis is therefore CO_2E to ethylene. While it is a promising technology, it is not without challenges. Mainly lack of stability.

1.1 Introduction to CO_2 Electrolysis

When burning hydrocarbons, such as ethylene (C_2H_4), the hydrocarbon is oxidised into CO_2 and H_2O in an exothermic reaction with O_2 (which is reduced). Since this is a reversible reaction, it is possible to react CO_2 and H_2O into hydrocarbons and O_2 in which case the CO_2 is being reduced. Opposite to the burning of hydrocarbons this reaction consumes energy, which can be supplied electrically in the process known as electrochemical CO_2 Reduction (CO_2R).

1.1.1 Fundamentals of Electrochemical CO_2 Reduction

In all electrochemical systems the total reaction can be divided into two half-cell reactions, one occurring at the cathode where electrons are supplied causing a reduction reaction, and one at the anode where a (counter) oxidation reaction occurs and electrons are drawn from. In alkaline conditions the CO_2 Reduction Reaction (CO_2RR) to a given product can be written (very generalised) as:

$$\mathrm{xCO_2 + yH_2O + ze^- \longrightarrow product + zOH^-} \quad \{1\}$$

In the more specific case where ethylene is the product, the reaction is:

$$\mathrm{2\,CO_2 + 8\,H_2O + 12\,e^- \longrightarrow C_2H_4 + 12\,OH^-} \quad \{2\}$$

and the oxidation reaction could be:

$$\mathrm{4\,OH^- \longrightarrow O_2 + 2\,H_2O + 4\,e^-} \quad \{3\}$$

1.1.1.1 Current & Potentials

The produced amount of a reaction product in mol (n) can be calculated using Faraday's laws of electrolysis:

$$n = \frac{Q}{zF} \tag{1.1}$$

where Q is the charge passed in Coulomb, z is the number of electrons involved in the (half-cell) reaction, and F is the Faraday constant defined as the product of the elementary charge (e) and the Avogadro constant (N_A): $9.6485 \times 10^4\,\mathrm{C\,mol^{-1}}$. The absolute minimum energy required by the reaction is given by the change in Gibbs free energy ($\Delta G^{\ominus}$ [$\mathrm{J\,mol^{-1}}$]), and is essentially the chemical energy stored in one mol of the product.

This energy is provided by the potential loss of the supplied electrons. Equivalent to Faraday's law, the thermodynamic cell potential (E°_{Cell}) can be related to $\Delta G^{\ominus}$ in the following way:

$$-zFE^{\circ}_{Cell} = \Delta G^{\ominus} \tag{1.2}$$

The thermodynamic cell potential corresponds only to the difference between the initial and the finale state of the reaction, and is not sufficient to drive the reaction alone. An energy barrier prevents the reaction from happening, and additional energy is required to overcome this barrier. This energy is known as the activation energy, and varies for different reactions. The total cell voltage drives both the anode reaction and the cathode reaction(s), and the total potential can be distributed to each of the half-cell reactions including the respective activation energies, but the required potential for each reaction also depends on the concentration (or activity) of the reactants and products and is influenced by reaction conditions such as temperature and (local) pH as given by the Nernst equation.When including these additional energies, the potential is only just sufficient to run the reaction at equilibrium conditions, but since it is a reversible reaction the net current would be zero. This is known as the exchange current density (i_0). In order to shift the reaction away from equilibrium, and ramp up the total reaction rate, an additional driving force, i.e. potential, is needed. Together, these additional potential requirements needed to "activate" the reaction will be denoted as activation overpotential (η_{Act}). The dependency of the activation overpotential and the reaction rate, i.e. the current density (i), is given by the Butler-Volmer equation, which at high currents (or activation overpotential) can be approximated into the Tafel equation:

$$\eta_{Act} = \pm A \cdot \log_{10}\left(\frac{i}{i_0}\right) \tag{1.3}$$

where A is known as the Tafel slope. Every (half-cell) reaction is associated with an individual exchange current density and Tafel slope. One (reduction) reaction could therefore be dominant at low current while another takes over at higher currents, if its Tafel slope is steeper. The combined reactions will though, more or less, follow the same trend. Thus, at higher currents, it should be expected that an increase in cell potential would cause an exponential increase in current, this is the case at moderate current densities, but as the current increases, the relation between the current and potential becomes linear due to ohmic losses.

Since the anode and cathode cannot be in direct contact with each other, as this would cause a short circuit, they must be (electrically) separated. However, there is a need for an ionic pathway between the two, and such separation can be obtained by using an electrolyte, an ion exchange membrane, or a combination. In all cases, the ionic conductivity is not perfect and will cause an ohmic loss. The size of the potential loss depends on both distance and conductivity. For an electrolyte, the ionic conductivity increases with concentration and in all cases an increases in temperature gives a higher conductivity and thus a smaller resistance. Ionic conductivity is generally significantly lower that the electric conductivity of any metal, and the ohmic resistance in a cell will therefore be highly dominated by the separator. The ohmic losses set the requirement of an additional overpotential and to distinguish it from the activation overpotential it shall be denoted as ohmic overpotential.
For several reasons, producing ethylene from CO_2 is, unfortunately, not as simple as just placing two electrodes into carbonated water and apply a current. First of all, since a proton source is needed (here water) to form hydrocarbons, CO_2RR will compete with the production of H_2 through the Hydrogen Evolution Reaction (HER):

$$2\,H_2O + 2\,e^- \longrightarrow H_2 + 2\,OH^- \qquad \{4\}$$

Furthermore, the reduction of CO_2 can lead to a wide range of products and not only hydrocarbons, but also liquid products such as ethanol (CH_3CH_2OH), acetic acid (CH_3COOH)) or formic acid (HCOOH).Luckily, by the use of different catalyst it is possible to both enhance the reaction rate as well as steer the selectivity not only between HER and CO_2RR, but also to a certain degree towards specific products.

1.1.1.2 Catalyst(s) for CO_2R

In simple terms, a catalyst is something that participates and enhances a (electro-)chemical reaction without being consumed or changed. The role of the catalyst is to lower the activation energy of the reaction and thereby increase the reaction rate (potentially from zero). Though fundamental studies of electrochemical CO_2R ranges back to the 19th century, the idea, and scientific field, of CO_2R as an energy storage can to a large extent be attributed to Yoshio Hori and his co-workers. Already in 1981[5] (1982[6])[1] they presented a paper with the title "Energy storage by elec-

[1] I have to be honest here, I did not read the 1981 paper since it is in Japanese, but from the abstract and title I assume it is more or less identical to the English version from

trolytic reduction of carbon dioxide"[II]. Throughout the 1980s Hori et. al investigated the catalytic effects of CO_2R on a large range of metals. To gain high selectivity for CO_2RR they initially selected metals known to have a large overpotential for HER and investigated the current efficiency towards formic acid at $5.5\,\mathrm{mA\,cm^{-2}}$ (In (0.84), Pb (0.85), Sn (0.64), Zn (0.42), Hg (1.00)). Later on, they found that Au and Ag showed high selectivity towards CO[7], but more interestingly they found that Cu were capable of producing methane (CH_4) and ethylene (C_2H_4)[8] and thereby opening the possibility of producing valuable chemicals by CO_2R.

1.1.1.3 Reaction Mechanism & Influence of Local Environment

In the last decade or so, the scientific community has gained renewed interest in the field of electrochemical CO_2R as a sustainable source of valuable carbon based chemicals[9], and one of the main focuses has been to understand the reaction pathway for the different products. Although Hori et al. already in the 1980s did a lot of work investigating the reaction mechanisms and the effects of the (local) reaction environment[10], the renewed interest in combination with development of both experimental and computational methods has lead to an even wider understanding of the mechanistic pathways of the different CO_2R products as well as the influence of the reaction environment. The full description of the mechanisms is complex, and many parts are still being debated. It is not within the scope of this thesis to present a detailed description, but if desired, many reviews can be found in literature, where especially the work by Nitopi *et al.* is recommendable. Nevertheless, a few key-points are important for this work, and will be briefly presented in the following.

***CO as an Intermediate Step**

There is a consensus that the pathway to C_2H_4, and other C_{2+} products, includes *CO as an intermediate step. CO_2 is adsorbed on the Cu surface where it is reduced through an electron transfer creating a surface bound *CO. From here, the *CO either desorbs as gaseous (or dissolved) CO, or reacts with another CO forming a C−C bond. It is still debated if this reaction only occurs between bound CO (*CO + *CO), or if it can also occur between a bound and a gaseous CO (*CO + CO(g))[11]. In all cases, the binding strength of *CO predicts the probability of forming a C−C

1982.

[II]By the way, already then part of their motivation was to reduce CO_2 emissions to the atmosphere!

bond. This also explains why e.g. Au and Ag mainly produces CO, since they have a lower binding energy for CO than Cu.

Catalysts Facets

The selectivity depends not only on the catalyst material, but also on the surface facet of the catalyst. Investigations of CO_2R on single Cu crystal surfaces has shown that a $(1\,1\,1)$ favours CH_4, whereas a $(1\,0\,0)$ surface shows high selectivity towards C_2H_4 and a stepped $(1\,0\,0)$ surface, e.g. $(7\,1\,1)$, increases the selectivity further[12]. This is supported by Density Functional Theory (DFT) calculations, indicating that (relatively few) stepped or under-coordinated defect sites are responsible for the CO_2RR[13].

Influence of pH

It is expected that the $C-C$ coupling mechanism is independent of pH, whereas the protonation of carbon to CH_4 is[11]. As shown experimentally, this causes a favouring of C_2H_4 at alkaline conditions, whereas the selectivity shifts towards CH_4 at low pH[14,15]. It is also known that HER activity increases at low pH[12,16], with a (possible[III]) decrease in CO_2R as a consequence. A high pH should therefore be favourable, but since CO_2 reacts with OH^- this can lead to a mass transport limitation of CO_2[11].

Effect of Various Cations

It is well known, that the cations of the electrolyte influences the catalytic activity. An electrostatic interaction between adsorbed species with a dipole moment, and cations placed close to the catalyst surface in the outer Helmholz plane, is known to enhance the CO_2RR[18]. Due to differences in hydration shell, larger cations, i.e. Cs^+ and K^+, are known to cause a significant enhancement compared to Na^+ and especially Li^+.

Effect of Temperature

The temperature effects many aspects of the reaction, some are directly dependent on the temperature, e.g. as given in the Butler-Volmer and Nerns equations, other aspects are more indirect. The solubility of CO_2 decreases with rising temperatures, and thereby increasing problems with mass transport limitations. This is somewhat counterbalanced by an increase in diffusion, of both ions and gasses, with rising temperature.

[III] There are studies showing CO_2R in acidic conditions[17].

Effect of Pressure

The concentration of dissolved CO_2 (and other gasses) also depends on the (partial) pressure, and increases with pressure as given in Henry's Law. Likewise the surface coverage of adsorbed species also increases with (partial) pressure, but not linearly.

1.1.1.4 Increasing Current Density

Most of the fundamental work, and especially with single crystals, are done in H-cell like systems, where CO_2 is supplied by saturating the electrolyte. This creates an upper limit to the CO_2RR current, due to mass transport limitations of CO_2. To overcome this, the typical strategy is to use GDE.

Gas Diffusion Electrodes

A typical GDE consist of a Gas Diffusion Layer (GDL) with a catalyst layer added on the surface. The GDL is essentially a porous structure, typically conducting, and somewhat hydrophobic. The purpose of the GDE is to create a three phase boundary on the surface of the catalyst, where electrons can react with the gas, diffusing in and out of GDE, while produced anions can be transported away through the electrolyte.
There are significant differences between the more fundamental systems and the GDE based cells. In the GDE based cells, the operation is dependent on the whole system including membrane, electrolyte and cathode as well as anode GDE. While the terms, CO_2R and CO_2E are typically used somewhat interchangeable, I find it more appropriate to use the latter to describe the operation of the full GDE based cells. The term CO_2RR is used to describe the cathodic reaction of CO_2 alone.

1.1.1.5 Types of Electrolysis Cells

When using GDEs there are fundamentally two possible cell types. The flow cell where a liquid catholyte layer is separating the membrane from the (cathode) GDE and the Membrane Electrode Assembly (MEA) , where the GDE is in direct contact with the membrane[IV].
In the last couple of years, a number of quite impressive result has been reported in literature using the flow cell type. One of the most remarkable ones is when García de Arquer *et al.*[19] from the Sargent group broke the

[IV] For the sake of completeness, it should be mentioned that CO_2E to CO can be done by solid oxideelectrolysis, but this is beyond the scope of this thesis.

limit of $1\,\mathrm{A\,cm^{-2}}$, by enhancing the transport mechanisms to the three-phase boundary. They, as well as others reporting high current densities, typically operate using a very high concentration of alkaline electrolyte, e.g. 7 M KOH. While this is impressing, the problem of operating in KOH is, that as CO_2 crosses over, the KOH will slowly transform into (bi)carbonate. The additional electrolyte layer in the flow cell design also adds an additional resistance. The more complex design also makes it less suitable for construction of large stacks, making it harder to scale to industrial use. The MEA type cell is therefore expected to be the most likely choice for industrial use.

1.1.1.6 The MEA Cell

The MEA cell consist of two flow fields, typically with a serpentine channel. The membrane is placed between the anode and cathode GDEs and together these make up the MEA, which is compressed in between the two flowfields.
It is well known, that CO_2 is transported across the membrane during operation, causing a lower than optimal CO_2 utilisation[20,21]. It is also well known that flooding of the cathode GDE causes lack of stability[22–24]. Furthermore, reaction between CO_2, OH^- and cross over cations causes salt precipitations in the flowfield, where it in time can cause a blocking of the gas channel.

1.2 Scope and Outline

In my Ph.d. project, as well as in this thesis, my aim has not been to get "the best result" ie. high numbers[v], but to investigate (some) of the challenges in high current density CO_2E, and to understand the mechanisms behind.
My work is presented in the following chapters.
Chapter 2 covers the attempt of upscaling an aqeous synthesis method to make $\{1\,0\,0\}$ faceted Cu Nano Cubes (NC).
Chapter 3 serves as both an explanation of how the experimental set up was build, and contains details of how all experiments were performed, somewhat corresponding to a methods section.
Chapter 4 covers the design of the operando X-ray cell used in the later chapters. It also contains details on how the cell was aligned in the beam and how the data was analysed.
Chapter 5 covers the findings from the first synchrotron beamtime, where salt precipitations and flooding of the GDE was observed to exhibit an oscillating behaviour.
Chapter 6 covers the second beamtime, where electrolyte based on different cations were tested in the same way as in chapter 5. Experiments with a double membrane and a series of CO Electrolysis (COE) experiments were also performed.
Chapter 7 describes my investigation into my hypothesis, that an internal electric field in the GDE was driving the cations towards the flowfield.
Chapter 8 covers the design of a new cell and the final heated and pressurised experiments.
Chapter 9 is a brief comment on the anode. Including my observations and thoughts on what the requirements for an industrial viable anode.

Experimental research is often a collaborative work, and this case is no different. Many of the chapters therefore include work done together with others. As an acknowledgement, and to clarify my part of the work, I have included a paragraph stating my contributions in the relevant chapters.

[v] Admittedly, I am not sure I would have written this sentence, had I succeeded in operating a cell with e.g. a C_2H_4 partial current density of $2\,\mathrm{A\,cm^{-2}}$ for $1000\,\mathrm{h}$ at $60\,^{\circ}\mathrm{C}$, but I really do find it interesting to understand the mechanisms causing degradation.

Chapter 2

Large Scale Catalysts Synthesis

My Contributions

The experimental work in this chapter consists of two parts, a series of initial small scale experiments and the later attempts of large scale synthesis. The initial work was done in collaboration with the postdoctoral researcher Sangkuk Kim, who did most of the small scale experimental work, whereas I contributed in planning and designing the experiments as well as discussing and understanding the results. The work on large scale synthesis was done solely by me.

This page intentionally left blank.

2.1 Chapter Introduction

As described in section 1.1.1 there seem to be a scientific consensus that $\{1\,0\,0\}$ faceted Cu is more selective towards C2 products and especially ethylene. Due to the Face-centered Cubic (fcc) structure of Cu, one way of obtaining NP with high ratio of $\{1\,0\,0\}$ facets is NC. The EcoEthylene project therefore included a goal of attempting to develop a cost efficient and scalable synthesis of $\{1\,0\,0\}$ faceted Cu NC, and subsequently to deposit these on Gas Diffusion Electrodes, in an attempt to increase selectivity.
Several research groups have shown successful methods to synthesise such Cu NC, as well as the ability to control the size[25]. All the methods are, though based on non aqueous synthesis, relatively costly, and not necessarily suitable for large scale production, making it desirable to find an alternative. In a paper from 2011 Jin *et al.* presented a method to synthesize Cu nano crystals in an aqueous solution and the ability to control the shape, and thereby the surface facets, including $\{1\,0\,0\}$ faceted NC. Their original focus was synthesising particles for use in localised surface plasmon resonance, but they also points out that the method could find use in the field of (electro-) catalysis. As the synthesis method consists of few steps, is done in aqueous solution, and with glucose as reducing agent and Hexadecylamine (HDA) as a capping agent, it looks like a promising candidate for a scalable and cost efficient method, due to the low material cost and simplicity.

2.2 The Original Synthesis Method

Jin *et al.* presented a synthesis method where $21\,\mathrm{mg}$ $CuCl_2 \cdot 2\,H_2O$ (precursor), $50\,\mathrm{mg}$ glucose (reductant) and $180\,\mathrm{mg}$ HDA (capping agent) were mixed with $10\,\mathrm{mL}$ of H_2O in a glass vial. The vial was capped and magnetically stirred over night at room temperature. The vial was then placed in an oil bath at $100\,^{\circ}\mathrm{C}$ for $6\,\mathrm{h}$ under continuous stirring. During the $6\,\mathrm{h}$ they observed that the solution gradually changed in colour from blue to red-brown. They explain the change with the gradual reduction of Cu^{+2} to Cu^0 by the glucose.
X-ray Diffraction (XRD) of the reduced particles showed only the presence of a Cu phase, and using Inductively Coupled Plasma Mass Spectrometry (ICP-MS) they found that $93\,\%$ of the precursor was converted to atomic Cu. Scanning Electron Microscopy (SEM) images showed that the product was mainly nanowires. To get an understanding of the

growth mechanism they varied both the amount of glucose and HDA as well as the reaction time. When using the initial method, but with only $90\,\mathrm{mg}$ HDA they found that the synthesised particles were in the shape of cubes. XRD patterns indicated that the NC were single crystal $\{1\,0\,0\}$ faceted as the strongest peak corresponded to the $(2\,0\,0)$ planes where as bulk Cu had $(1\,1\,1)$ as the strongest peak. The changes is explained by the cubes showing a preferred orientation, with $\{1\,0\,0\}$ planes being parallel to the substrate. The findings were confirmed by High Resolution Transmission Electron Microscopy (HR-TEM).

2.2.1 Growth Mechanism

The growth mechanism, Jin *et al.*[26] propose is that glucose reduces Cu^{+2} ions to Cu^{0} which forms a nucleation site. As the reaction continues the crystal grows into a seed and the HDA capping agent binds preferentially to the Cu $(1\,0\,0)$ facets protecting these facets. Further growth is thereby limited to other facets resulting in a single crystal NP bound by $\{1\,0\,0\}$ facets. If the nucleation starts with a twin seed and the HDA concentration is sufficiently high, the $\{1\,1\,1\}$ facets will also be protected resulting in a wire shaped growth. The HDA also prevents re-oxidation of the surface and therefore, if the the HDA concentration is lower, the twin seeds will suffer from oxidative etching leaving behind a single grain seed that will grow further into a $\{1\,0\,0\}$ faceted NC. The main elements in the proposed mechanism seem widely accepted in literature[27], but the complete understanding and details are still debated[28]. Using DFT Fichthorn & Chen[29] found that Cl^{-} ions lowers the binding of HDA to the $\{1\,1\,1\}$ facets causing the facet selective binding of HDA to $\{1\,0\,0\}$. As a consequence they conclude that at low Cl^{-} concentrations spherical NP are more likely to form whereas at high Cl^{-} concentrations facet shapes, like nanowires, are formed.

2.3 Initial Small Scale Tests

Prior to up-scaling the method, our first step was to replicate the original method producing NC and understand the importance of various parameters such as the reaction temperature, the amount of oxygen present in the reaction vial as well as the stirring rate.

2.3.1 Importance of Uniform Reaction Temperature

Initially the small scale synthesis attempts showed varying and inconsistent results. There were clear indications that even small changes in temperature around 5 to $10\,^{\circ}\mathrm{C}$ would change the reaction conditions and the result significantly, but no clear trends were obvious due to the large inconsistency between experiments. At this point it was assumed that the oil bath would be uniform in temperature and that stirring the solution in the vial would be sufficient to ensure isothermal reaction conditions through out the sample. This was later found not to be the case. As the oil bath was heated from the bottom, and the $20\,\mathrm{mL}$ vials are quite long, a significant temperature gradient of more than $5\,^{\circ}\mathrm{C}$ could be measured between the top and the bottom of the vial.
In order to solve the issue an additional stir bar was placed in the oil bath. With the oil being stirred around, and ensuring that the vial was kept steady and away from the heating element and the sides of the oil bath, the temperature gradient across the vial was lowered to less than $1\,^{\circ}\mathrm{C}$.
After ensuring that the reaction was done under isothermal conditions the results were now consistent and reproducible. This showed that not alone is the reaction temperature important, but ensuring a uniform heating is perhaps even more important than the temperature itself.

2.3.2 Headspace in Vials

As it seems obvious that a large scale synthesis cannot be done in small vials, it was important to get a minimal understanding of how the volume and especially the (air filled) headspace influenced the reaction and the shape of the synthesised particles.
Three identical $20\,\mathrm{mL}$ vials (total volume of $23.5\,\mathrm{mL}$) were filled with respectively $4\,\mathrm{mL}$, $8\,\mathrm{mL}$ and $20\,\mathrm{mL}$ of identical solutions. Each of them was then placed in an oil bath and isothermally heated to $100\,^{\circ}\mathrm{C}$. In all cases the solution was stirred using a magnetic stir bar placed in the vial and the stirrer set to $300\,\mathrm{rpm}$. The $20\,\mathrm{mL}$ sample changed colour from

blue to completely red indicating that a full reduction of the solution had occurred. SEM images showed a mixture of Cu NC and (more) spherical NP with particle sizes in the order of 350 to $400\,\mathrm{nm}$. The $8\,\mathrm{mL}$ sample changed to a pale orange indicating that the sample was only partially reduced. This was further confirmed as SEM images showed only few NP. The $4\,\mathrm{mL}$ sample only turned greenish-yellow, with no signs of further reduction even after $12\,\mathrm{h}$. SEM images showed no signs of Cu NP. This indicated that excessive amounts of oxygen present in the vials prevented the reduction. To confirm that the observed variations were not due to differences in sample amount, or the headspace itself, two similar $4\,\mathrm{mL}$ samples were prepared, one were placed in a similar $20\,\mathrm{mL}$ vial, but deaerated by purging argon into it the other sample was not deaerated, but instead put in a $4.5\,\mathrm{mL}$ vial. Both samples reduced fully, but where the non-purged sample reduced to faceted NP (triangles and cubes) of similar size as the previous $20\,\mathrm{mL}$ sample, the deaerated sample contained smaller and more spherical NP with a size around 80 to $100\,\mathrm{nm}$.

The small sample size prevents any clear conclusions, but this indicates that small amounts of oxygen could be beneficial in preventing spherical non faceted particles whereas large amount of oxygen prevents a full reduction. This would also be in agreement with the proposed mechanism, as the small amount of oxygen could be responsible for the oxidative etching.

2.3.3 Effect of Stirring Rate

In the small vials it is possible to stir the solution quite vigorously using a magnet stir bar. As the same stirring is not easily obtained in a large volume it was interesting to investigate if the stirring rate influenced the synthesis. Three $5\,\mathrm{mL}$ samples were prepared in $20\,\mathrm{mL}$ vials and purged with Ar. They were again heated in an oil bath at $100\,^{\circ}\mathrm{C}$, but with the stirrer set to $50\,\mathrm{rpm}$, $100\,\mathrm{rpm}$ and $300\,\mathrm{rpm}$ respectively. Where the $300\,\mathrm{rpm}$ sample contained mainly larger spherical particles, the $100\,\mathrm{rpm}$ and especially the $50\,\mathrm{rpm}$ samples contained NC fairly uniform in size around $80\,\mathrm{nm}$.
It seems clear that a lower stirring rate is beneficial, but not why. Taking the findings of Fichthorn & Chen into account, it could be hypothesised that the local concentration of Cl^- plays a role, and that high stirring rate lowers the concentration at the surface of the particles due to a more uniform distribution, but this was not investigated further.

2.4 Large Scale Synthesis

The aim of the large scale synthesis was to produce $5\,\mathrm{g}$ of Cu NC per batch. In the ideal case where all of the $CuCl_2$ would be reduced to Cu, and all as NC, it would require a solution containing $78.683\,\mathrm{mmol}$ Cu $\left((5\,\mathrm{g})/\left(63.546\,\mathrm{g\,mol^{-1}}\right)\right)$ corresponding to $13.4\,\mathrm{g}$ of $CuCl_2 \cdot 2\,H_2O$ $\left(78.683\,\mathrm{mmol} \cdot 170.483\,\mathrm{g\,mol^{-1}}\right)$. Following the original method, this should be mixed with HDA and glucose in $6.38\,\mathrm{L}$ of water. For technical reasons it was decided to start out with a $5\,\mathrm{L}$ solution using $10.5\,\mathrm{g}$ of $CuCl_2 \cdot 2\,H_2O$, $25\,\mathrm{g}$ glucose and $90\,\mathrm{g}$ of HDA. This is equivalent to $61.6\,\mathrm{mmol}$ of Cu or $3.91\,\mathrm{g}$. This correspond to an up-scaling of the small synthesis by a factor of 500 and can obviously not be done using closed vials and an oil bath, so a new system design was needed.
It was considered to start out with scaling up by eg. a factor of 10 or 50, but as each step would require a new and different system and not necessarily provide any insight into the problems of further scaling steps, it was decided to go directly to the $5\,\mathrm{L}$ step and if necessary work downwards from there.

2.4.1 Designing the Large Scale Synthesis System

Given the large step scale up, there were limited expectations to the result, which parameters would be important and which problems would occur. The designing of the the system was therefore done with a "as simple as possible" philosophy, with the aim of getting sufficient knowledge to make the necessary improvements later on[1]. Given the findings in the initial small scale tests, it was though obvious that a few things had to be taken into consideration. First, it was evident that a uniform heating was necessary. I therefore assessed that the classical method using a round bottom flask heating mantle was not ideal. Instead, I decided to place a $5\,\mathrm{L}$ round bottom flask inside an oven.

To minimise thermal gradients in the solution, each experiment was started in a cold oven and the temperature was then moderately ramped (over $1.5\,\mathrm{h}$) to the desired set-point while stirring the solution. A picture of the system can be seen in fig. 2.1.
The stirring was done using a (very simple) overhead stirrer motor con-

[1] I am sure that a chemical engineer with expertise in large scale synthesis will find the result quite bizarre, but sometimes you just have to try with the means available. And hey, it worked.

nected to a flexible Perfluoroalkoxy Alkane (PFA) tubing. The motor was placed on top of the oven with the tube going through a hole in the oven, through a sealing stirrer baring in the top of the flask, and inserted so that the tube would lie on the side of the flask. Besides being a low cost and simple solution, this ensured high convection on side of the flask while still providing sufficient and uniform mixing in the bulk solution. A very high rate stirring was not obtainable using this method, but this was also not desired as the initial experiments had indicated that a lower stirring rate was to prefer.

Figure 2.1: *Left picture shows the setup in the oven. Upper right pictures show the sonification and stirring of the solution. The lower right pictures show the colour change in the solution during the reaction.*

It was also clear that avoiding, or at least minimising the amount of, oxygen present would be essential. While this is fairly easy in a closed vial, it is not as simple in a round bottom flask full of water at a temperature around $100\,^{\circ}\mathrm{C}$. The solution became to insert a tube, going to the top of the round bottom flask, and purge the flask with Ar. To avoid high pressurisation, both from the Ar flow and from the evaporating water,

an exhaust line was added. A water filled U-turn on the exhaust line, out side the oven, ensured a slight overpressure in the attempt of lowering evaporation.

As a first test of the system, a $1\,\mathrm{L}$ solution was prepared by sonification and more than $24\,\mathrm{h}$ of stirring until homogeneously mixed solution was obtained. The solution was transferred to the $5\,\mathrm{L}$ round bottom flask and heated to $100\,^{\circ}\mathrm{C}$ in the oven. Despite the continuous purging Ar, the solution only changed colour from light blue to pale green after $4\,\mathrm{h}$ (see fig. 2.1), indicating that the large headspace prevented a full reduction, similar to what was observed in the initial experiments. It is unclear if the effect is caused by too much oxygen or if the large head space plays a role in itself, eg. due to a large surface area, evaporation or other unknown effects.

Figure 2.2: *Photo series showing the change in colour of batch#1 (*$5\,\mathrm{L}$, $100\,^{\circ}\mathrm{C}$*) during the reaction. After around* $5\,\mathrm{h}$ *the flask tilted over causing the lower amount of solution seen in the last picture.*

2.4.2 Large Scale Batch#1

A new attempt at $100\,^{\circ}\mathrm{C}$ was performed using $5\,\mathrm{L}$ of solution and thereby minimising the head space. As it can be seen in fig. 2.2 the solution gradually changed in colour, from the initial light blue, over a pale orange to a more reddish brown, indicating that the $CuCl_2$ had reduced to Cu during the $6.5\,\mathrm{h}$. The observant reader will notice a significant drop in the solution on the last picture as well as the more sturdy fixation and support of the flask. Unfortunately, the flask fell down after slightly more than $5\,\mathrm{h}$ causing not only a spillage of the solution, but also an aeration and temporarily partial cooling while the oven was cleaned. After the flask was securely fixated in the oven, the experiment was resumed for the remaining time. The oven was programmed to cool down for $30\,\mathrm{min}$ while the solution was stirred and and purged with Ar. The slightly warm solution was then poured into sealed containers and left overnight. A sample taken from the bottom of the container was washed and centrifuged in ethanol several times before being inspected using SEM. As seen in fig. 2.3 the sample contained a large amount of cubic particles as well as nanowires. The NC are of various sizes, but with a side length in the order of $100\,\mathrm{nm}$. It was thereby established that the method and the system was suitable for large scale synthesis of Cu NC, though further optimization was needed.

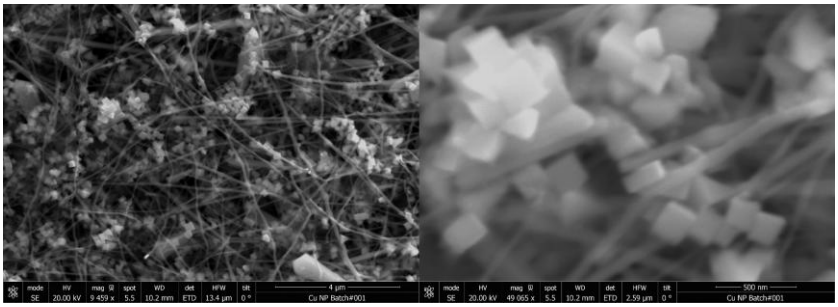

Figure 2.3: *SEM images of the particles produced in the first batch* ($5\,\mathrm{L}$, $100\,^{\circ}\mathrm{C}$)*. The images show a large amount of cubic shaped particles, but entangled in long wires.*

2.4.3 Effect of Temperature

The reaction temperature was known to be an important factor, and although the temperature in the oven is controllable and expected to be quite stable, the actual temperature of the solution was unknown. The actual temperature could of course just have been measured, but it was deemed more important to determine the effect of varying the oven temperature as this could also affect both heat transfer and evaporation and thereby change the reaction conditions.

In order to lower the consumption of chemicals used and the amount of waste produced as well as for technical reasons[II] the following test were done in a $1\,\mathrm{L}$ round bottom flask. To avoid inconsistency a $5\,\mathrm{L}$ solution was prepared and $1\,\mathrm{L}$ was used for each batch. Four experiments were performed with the oven set to $90\,^{\circ}\mathrm{C}$, $95\,^{\circ}\mathrm{C}$, $100\,^{\circ}\mathrm{C}$ and $110\,^{\circ}\mathrm{C}$ respectively. The initial ramping time (not rate) was kept identical. Pictures were taken at appropriate intervals in order to be able to compare the reaction rate based on the change in solution colour. All four batches turned to a dark red colour before $6\,\mathrm{h}$ indicating a full reduction of Cu^{+2}, but as seen in fig. 2.4 the reaction rate is heavily dependent on temperature.

SEM images reveal that samples from all four batches contain a mixture of $\mu\mathrm{m}$-sized tetrahedron shaped particles as well as agglomerations of

[II] Well, let me be honest, I accidentally broke the $5\,\mathrm{L}$ round bottom flask while cleaning it, and the delivery time for a new one was too long. Oops!

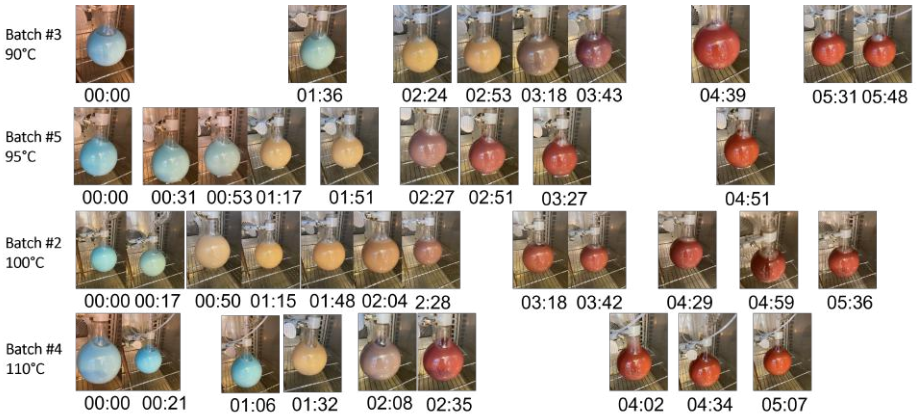

Figure 2.4: *Picture series from the four batches. Each picture is placed according to the reaction time. It can be seen how the reaction rate depends on the temperature.*

100 to 150 nm sized particles mainly cubic but also tetrahedrons, as seen in fig. 2.5. High resolution SEM imaging was difficult as the samples still contained large amounts of (expectedly) HDA. After further washing and centrifuging the samples in ethanol it was possible to increase the magnification and analyse the NC, especially when using higher acceleration voltage (30 kV vs. 30 kV) and a back scatter detector. Images from the four batches can be seen in fig. 2.6.

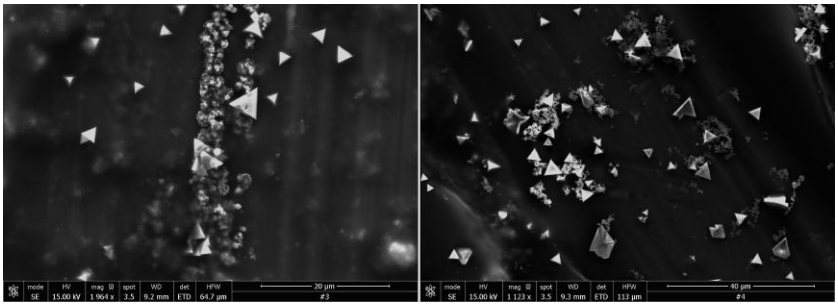

Figure 2.5: *SEM images of a mixture of* µm*-sized tetrahedron shaped particles as well as agglomerations of* 100 *to* 150 nm *sized particles. The small particles are mainly cubic, but also some tetrahedrons are seen.*

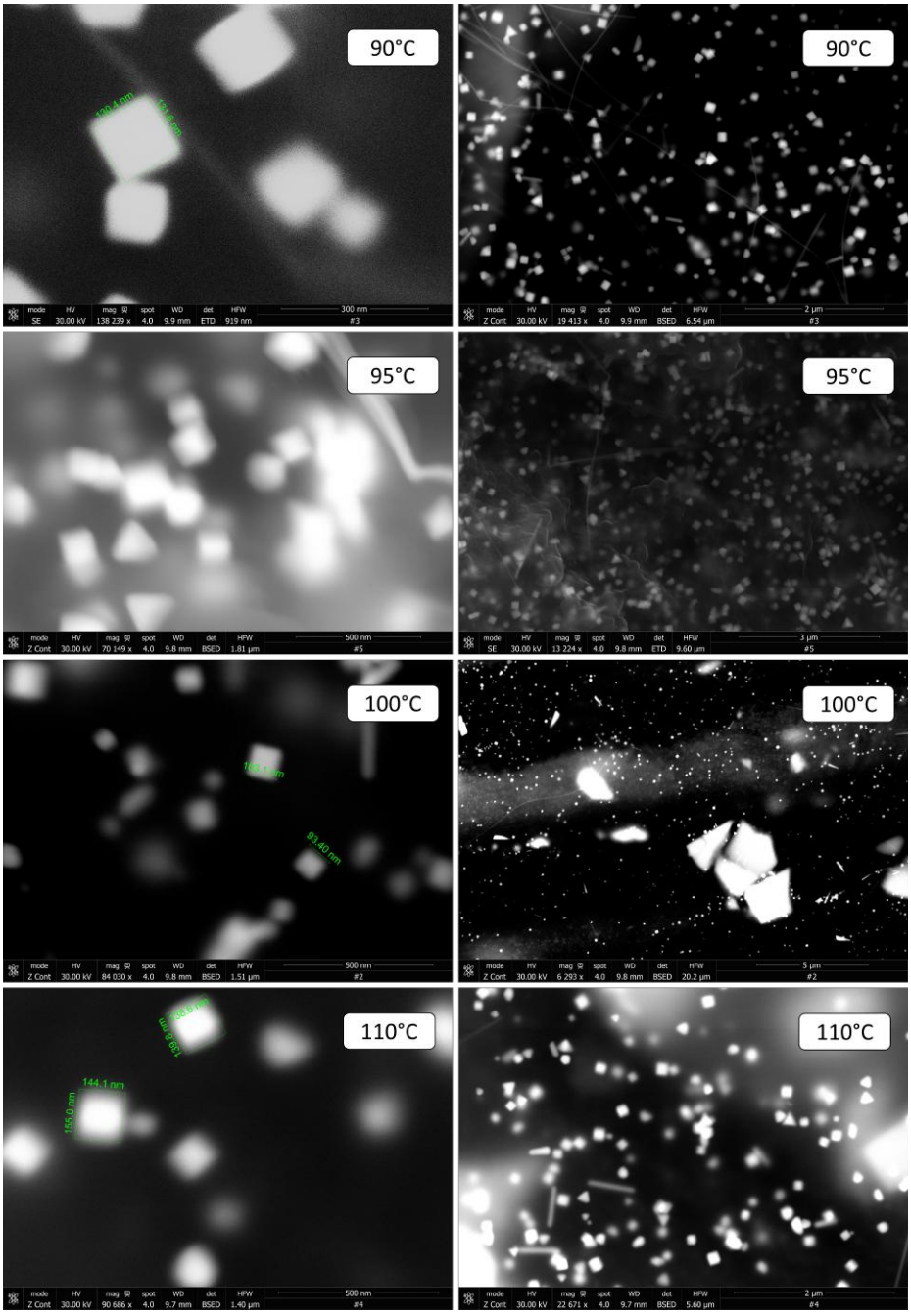

Figure 2.6: *High (left) and low (right) resolution SEM images of the four batches after cleaning.*

The images did not show any major differences between the four batches. The size of the NC seemed to be somewhat uniform in each batch, and though there was a difference between the batches ranging from 100 to $150\,\mathrm{nm}$, no clear trend indicating a correlation with temperature was found. Compared to batch 1 the amount of nanowires was significantly smaller whereas the amount of large particle was higher. It is unknown if this is due to the smaller reactor volume, the temporary cooling of the first batch or caused by accidental aeration.

2.4.4 Test of Gas Diffusion Electrodes

In order to test the Cu NC as a catalyst, GDEs were prepared by depositing various preparations of the synthesis product onto carbon based GDLs (Sigracet 39 BB).For all GDEs the sample was dropped onto the GDL using a pipette. The GDEs were then tested in an MEA type electrolysis cell using an anion exchange membrane (Sustainion® X37-50 Grade RT) and a carbon based IrO_2 anode (Dioxide Materials). All test were done at constant currents ranging from 50 to $200\,\mathrm{mA\,cm^{-2}}$.

Tests were made using both the uncleaned synthesis product (taken from the bottom) and samples washed and centrifuged in ethanol, but in all cases the GDEs showed no activity for catalysing CO_2RR as only H_2 was detected as a product of the CO_2E.

The exact cause of the lacking activity was not clear, but the depositing method was definitely not ideal. Especially for the uncleaned sample, the catalyst layer was unevenly distributed and expectedly to thick or too thin. Indicated by the SEM images, it seemed like a large amount of HDA was still present on the particles, even after thorough washing in ethanol, and I expect this also influenced the poor activity. My hope was, that by keeping a small layer of HDA on the NC, it could protect the NC against oxidation causing a loss of the faceting. It was expected that the HDA would be stripped of the surface of the NC in situ when a cathodic potential was applied, but either this did not happen, or the continued presence of HDA in the GDE or residue of the other synthesis ingredients affected the performance.

The next step planned was to attempt to prepair a more homogeneously covered GDE by spray coating the particles on the substrate using Ar or N_2. I also planned to try cleaning the samples further using Heptane, but none of it was carried out as it was decided to, at least temporarily, terminate the attempt of synthesising NC.

2.4.5 Terminating the Project

The decision on terminating the Cu NC project was made for several reasons. The other partners in the EcoEthylene project were still working on optimising the preparation of GDEs using commercial spherical Cu (and CuO) NP making it less urgent to upscale the synthesis. Furthermore, reports in literature indicated that the particles would not sustain

the cubic structure during CO_2E[30–32]. And thought it is still debated in literature[25], it made it questionable whether the strategy would provide a stable increase in selectivity towards ethylene. At the same time, there were still challenges operating the cell at elevated temperatures as well as problems maintaining long time stable operation. It was therefore prioritised to focus on understanding the degradation mechanism and raising the temperature.

Based on the work presented here, I do nevertheless believe it can be concluded, that this synthesis method is a good candidate for a cost effective and scalable production of $\{1\,0\,0\}$ faceted Cu NC, albeit it does require more research and engineering.

Chapter 3

The Setup & Initial Experiments

This page intentionally left blank.

3.1 Chapter Introduction

The design and construction of the experimental setup were an ongoing and iterative process throughout the project. The final result is a fairly complex system with capabilities of both heating and pressurising the cell, but a lot of things were altered in the process. Many experiments were performed along the way, providing not only information about the CO_2E, but also needs for altering the setup.
Therefore, this chapter serves both as a presentation of some of the early experiments as well as a description of the setup.

It is relevant to investigate the reaction at temperatures around $60\,^{\circ}\mathrm{C}$, since an industrial stack most likely will be operated around this temperature. This is because any loss will produce heat, meaning that the a cell stack must be cooled. Since it is easier to cool it down if its temperature is above the surrounding temperature, it will be beneficial to operate at these elevated temperatures.

3.2 The Standard MEA and Cell Assembly

Unless stated otherwise, the cathode GDEs used in this project is based on a Sigracet 39BB Polytetrafluoroethylene (PTFE) containing carbon paper (FuelCell Store) as GDL and a $150\,\mathrm{nm}$ thick Cu layer prepared by sputtering 6N Cu in a vacuum chamber (10^{-5} to $10^{-6}\,\mathrm{Torr}$) at a deposition rate of $1\,\mathrm{\AA\,s^{-1}}$. The deposition was done under an argon flow of $5\,\mathrm{mL\,min^{-1}}$, with a total pressure of $3\,\mathrm{mTorr}$. The anode is a commercial IrO_2 coated carbon based GDE from Dioxide Materials.
The standard membrane used is an anion exchange membrane from Dioxide Materials (Sustainion X37-50), activated in $1\,\textsc{m}$ KOH for $24\,\mathrm{h}$ then washed and stored in deionized water ($18.2\,\mathrm{M\Omega}$).
Except for the work performed using the operando X-ray cell (see chapter 4), the cathode area ranges from 1 to $2.89\,\mathrm{cm^2}$ and the anode area was $6\,\mathrm{mm}$ wider on both sides. $200\,\mu\mathrm{m}$ PFA or PTFE gaskets were used on both anode and cathode side surrounding the GDE with a $3\,\mathrm{mm}$ gap.
The cell is assembled by placing the membrane in between the gaskets and placing it on top of the cathode GDE lying on the graphite flowfield. The anode GDE is then placed on top of the membrane and the anode Ti flowfield is mounted and fastened. The cell is tightened in a star pattern first with $2\,\mathrm{N\,m}$ then with $4\,\mathrm{N\,m}$.

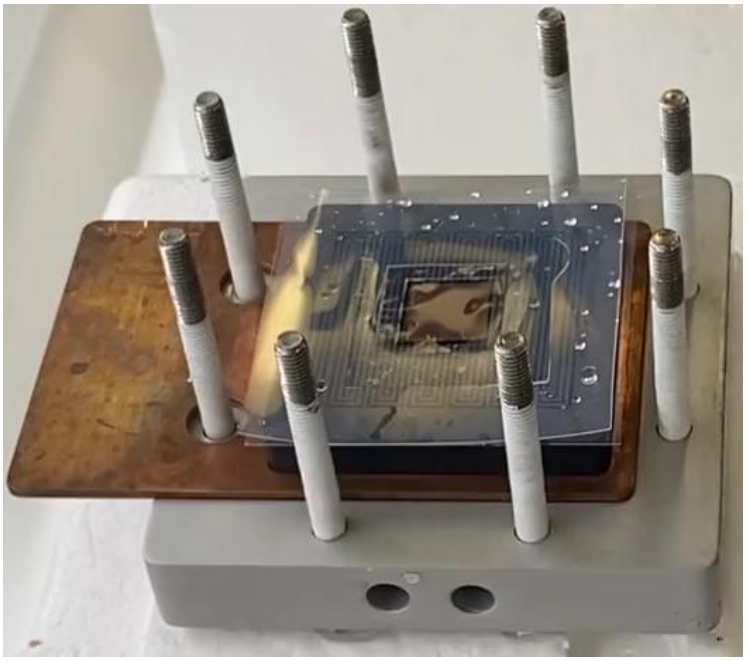

Figure 3.1: *Membrane with gaskets placed on top of the cathode GDE lying on the graphite flowfield during cell assembly.*

3.3 The Basic Setup

A common way of operating an MEA type CO_2E cell is with electrolyte on the anode side and a CO_2 gas stream on the cathode. The cell is then connected to a potentiostat supplying current in either potentiostatic or galvanostatic mode. The work presented in this thesis is all done in galvanostatic mode, for reasons discussed in section 3.5, but otherwise the cell operation is done as described.
A sketch of the simplest setup can be seen in fig. 3.2, and later iterations are based on this. The electrolyte is continuously pumped from a reservoir into the anode inlet and the outlet, containing both the electrolyte as well as O_2 and crossover CO_2, is lead back to the reservoir. If the cell is placed vertically, the inlet is in the bottom of the flowfield and the outlet is at the top to facilitate the removal of gas bubbles. The pump used is a diaphragm pump (KNF NF1.5TTDCB-4). In order to ensure as stable and repeatable pumping speed as possible the pump was made digitally controllable using an Arduino Nano Every as a 5 V Digital Ana-

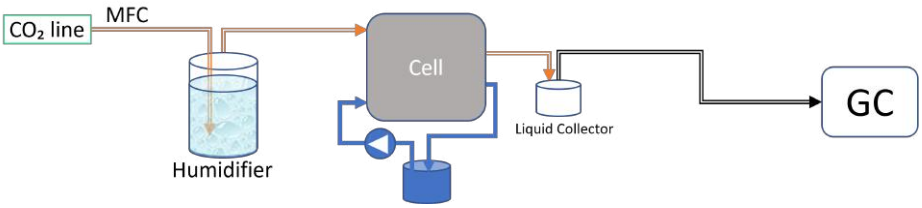

Figure 3.2: *A sketch of the simplest setup. This is the basis for all later iterations.*

logue Converter (DAC). The Arduino was controlled from a Raspberry Pi using an Inter-integrated Circuit (I2C) bus. The pump was operated at $50\,\%$ roughly corresponding to $15\,\mathrm{mL\,min^{-1}}$, except for when using the smaller X-ray cell, where it was operated at $25\,\%$ or approximately $7.5\,\mathrm{mL\,min^{-1}}$.
On the cathode side, the inlet CO_2 flow was regulated using one or more digital thermal Mass Flow Controllers (MFCs), if not specified the flow was $50\,\mathrm{mL\,min^{-1}}$, and the MFCs used was the red-y smart series from vögtlin. As the reaction consumes H_2O it is common to humidify the gas by bobbling it through water, as discussed later, this was done in some of the experiments, but not all. The (humidified) CO_2 is sent to the inlet in the top of the cathode flowfield, so that water droplets and liquid products can escape easier. The cathode outlet gas, containing the reaction products, is let into an air tight $100\,\mathrm{mL}$ glass bottle to prevent liquids from entering the rest of the system. A gas line connected to the top of the bottle is connected to an in-line Gas Chromatograph (GC) for quantification of the reaction products which can then be used to calculate the partial current density and Faradaic Efficiency (FE). While it is possible to collect gas samples and analyse them in a stand alone GC, it is highly beneficial to use an in-line GC, especially if the aim is to investigate and understand phenomena affecting the selectivity on a shorter time scale. When running, the in-line GC takes a small sample (typically 0.25 to $1\,\mu\mathrm{L}$) of the gas stream and analyses it. When the analysis is done a new sample is taken and analysed. Depending on the type and configuration of GC the analysis time can be anything from a few minutes to as much as half an hour. The time resolution of the gas analysis, and thereby the partial current density and FE, therefore depends heavily on the GC configuration, and during this Ph.D. project much work has been put into developing an optimised GC configuration and method

for CO_2E. A detailed description and discussion of the GC configuration and method can be found in appendix A. In order to calculate the partial current density and FE it is necessary to know the outlet flow of the cell, initially this was done using a Volumetric Flow Meter (VFM) (MesaLabs Defender 530+) placed downstream of the GC, but this was changes later on as discussed in section 3.8.
From the concentration of a specific gas (c_x) measured by the GC and the total (mol) flow ($\dot{n}_T$) at the time of the injection, the partial current density (i_x) can be calculated by the time derivative of eq. (1.1):

$$\dot{n}_x = \frac{\dot{Q}_x}{z_x F} \tag{3.1}$$

$$c_x \dot{n}_T = \frac{i_x \cdot A_{cat}}{z_x F} \qquad \Leftrightarrow \qquad i_x = \frac{c_x \dot{n}_T \cdot z_x F}{A_{cat}} \tag{3.2}$$

3.3.1 Ag Tests

Initially a series of experiments were done to get experience with the system and the cell, and to see if everything worked as expected. For several reasons these test were performed using a porous Ag membrane (Sterlitech Inc., purity $99.97\,\%$, pore size of $1.2\,\mu\mathrm{m}$) as cathode catalyst and GDE. First of all, Ag is known to mainly produce CO making it simpler to analyse the outlet gas composition (i.e avoiding problems in the GC analysis of more complex hydrocarbons). Secondly, because the Ag membrane acts as both catalyst and GDE, problems related to catalyst layer thickness, flooding, or the GDE itself, is minimised. Additionally, this catalyst and its performance, was well known to the group. All together, the Ag membrane was suitable as a "reference" or benchmark test of the system.
Figure 3.3 shows the result of one of these experiments performed with a $1\,\mathrm{cm}^2$ electrode and in this case the reinforced Sustainion AEM. Besides showing that it was possible to do CO_2E in the setup, this experiment (together with the others) also provided information on how to improve the setup, as well as what could be interesting to investigate further. fig. 3.3c shows the partial current density of H_2 (red), CO (blue) and the sum of the two (green), as well as the total current density applied (black) vs. time. While it is common to report the FE, as it makes it slightly easier to compare selectivity, the (partial) current density provides more information when investigating stability and dynamic trends. In this experiment the current was stepped up by $50\,\mathrm{mA\,cm^{-2}}$ every hour until

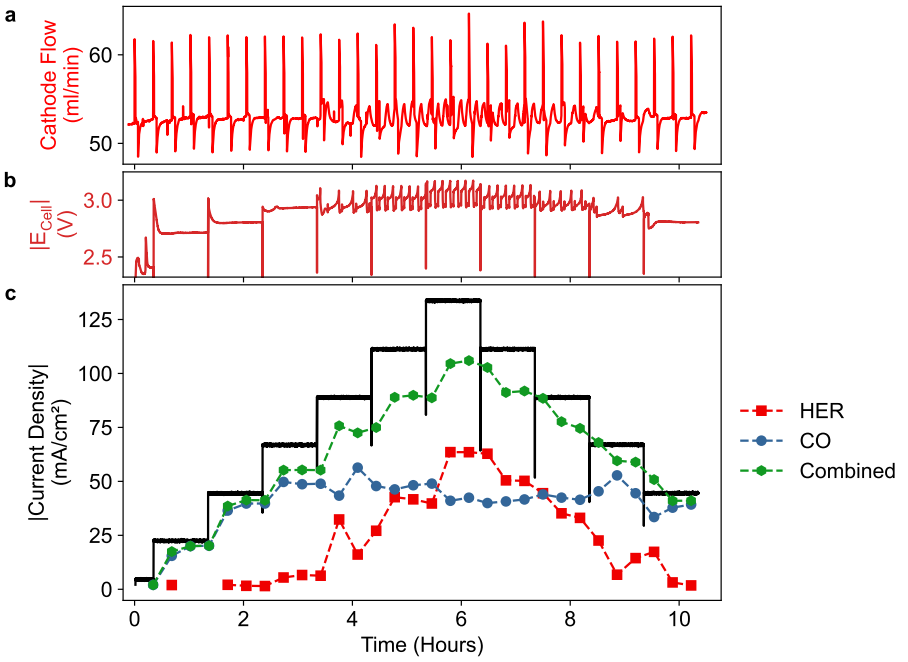

Figure 3.3: *The plot shows the result of an experiment using a* $1\,\mathrm{cm}^2$ *Ag membrane as both GDE and catalyst. In this case the reinforced Sustainion Anion Exchange Membrane (AEM) was used.*

$300\,\mathrm{mA\,cm^{-2}}$ to investigate the performance and selectivity at different currents. It was then stepped down again in the same way, to see if the CO selectivity was regained or if the change was permanent, i.e. caused by some degradation mechanism. This reveals that the partial current density of CO is limited to just above $100\,\mathrm{mA\,cm^{-2}}$. When looking at the outlet flow in fig. 3.3a, it can be seen that the flow is somewhat stable around $53\,\mathrm{mL\,min^{-1}}$, but with a periodically repeating pattern of spikes followed by a small decrease in flow. This happens because the narrow bore of the sampling valves in the GC creates a flow restriction. When the GC takes an injection the flowpath is changed so it only passes the valve once instead of twice. A different, less periodic, kind of oscillation can also be observed at current densities above $200\,\mathrm{mA\,cm^{-2}}$. Interestingly enough, they correlate with both increased H_2 production and oscillations in the cell potential seen in fig. 3.3b. A similar, though slightly slower, phenomena will be discussed in chapter 5, but at this

point there were no clear explanation of the oscillations, except that it was expected to be caused by CO_2 mass transport limitation either due to flooding or diffusion limitations in the Ag membrane. It is expected that the outlet flow will increase when the selectivity shifts towards H_2 since HER does not consume CO_2, but instead produces additional gas. Since $100\,\mathrm{mA}$ corresponds to a H_2 production of approximately $0.75\,\mathrm{mL\,min^{-1}}$, the variations in flow could be explained by an increased H_2 production, but it could also be caused by some unknown change in pressure. The GC data unfortunately does not provide much information, both because the time resolution is too low, but also because there seem to be a significant time delay between the gas production and the GC detection. This is most clearly seen by how the combined gas products in first GC injection after a current step does not match the new current, but rather the previous. This is caused by a too large dead volume between the cell and the GC.
All in all, the initial experiments showed that it would be interesting to extent the setup with a pressure measurement on the inlet as well as adding a more complex gas system giving the possibility of diluting the inlet CO_2 gas stream with various gasses as well as controlling the humidification. The volume between the cell and the GC was also decreased by changing the tube size and removing unnecessary dead volume.

3.4 Various Causes of Low Performance

Some of the first experiments using Cu based GDEs showed very poor performance for various reasons. In general these can be divided into two categories. One is mechanical instability including short circuiting between the anode and the cathode, as well as leakage of gas and/or electrolyte, both out of the cell as well as between the two sides. The second category is when a mechanically stable cell shows low selectivity towards CO_2R, i.e. high FE for H_2.

3.4.1 Mechanical Failure

The explanation for the mechanical issues is a combination of several factors, first of all it take some time to get sufficient experience in how to assemble and mount the cells. This includes both the mechanical process where handling of the membranes, the level of compression, the type and thickness of the gaskets used, plays an important role, but also the time it takes between the cell is assembled and the electrolyte is

supplied, as well as how long it takes before the current is then applied, is important since the membrane dries very quickly, which makes it very fragile. Furthermore, ageing of the membranes as well as large variations in quality of the Sustainion membrane between different batches have been observed to cause both mechanical problems as well as variations in performance.

3.4.2 Metal Contamination

I found that one of the biggest contributors to low CO_2R selectivity was metal contamination from the system. Initially the tubing was connected to the pump using a metal Swagelok connector. Even though it was only a small piece of metal, the electrolyte was continuously cycled thought it and this was enough to cause a contamination. The problem seemed to be worse when using a Cu catalyst, and was seen as a gradual increase in selectivity towards HER. Removing the metal part, seemed to solve the problem as the performance increased, though it did not completely prevent HER. As seen in fig. 3.4, the piece it self was clearly discoloured, but it is unknown if this was related.

Figure 3.4: *Picture of the discoloured Swagelok Part*

The same was observed for the X-ray cell, where the initial design contained metal inlets, as covered in chapter 4. Here it was seen, that a regain of performance was obtained after cleaning the cell in nitric acid, only to be worsened shortly after.
Though I have not made an actual study of this, my impression is, that the Cu catalyst based CO_2E is quite prone to contamination of metals active for HER.

3.5 Controlling Potential or Current & Ref. Electrode Position

The potentiostat configuration can be either a two-electrode setup where the full cell potential is measured (or controlled) or in a three electrode setup where a reference electrode is used to obtain information of the cathode and anode half cell potentials. The potentiostat can, very generalised, be operated in two modes, controlled current or controlled potential. The two modes are known as[33], Chronoamperometry (CA) where a constant potential is supplied and current is measured vs. time. Alternatively, the potentiostat[1], supplies a constant current and measures the potential vs. time, known as Chronopotentiometry (CP). More sophisticated uses of the techniques exists, but will not be covered here. Through my Ph.D., a it has been a reoccurring discussion in our group if we should do constant current or constant potential experiments. From a purely theoretical point of view, the answer is easy, we should use a constant potential. In the real world, where experimental conditions rule, the answer is not so simple.

3.5.1 CA vs. CP

When operation at constant potential, or CA, the potentiostat applies a constant voltage measured between the working electrode and the reference electrode. Since the electrochemical reactions depend on the potential at the surface of the catalyst, controlling this potential is, of course, the most correct way to investigate the influence of potential on reaction rates and selectivity. Further more, it has the benefit, that since the current scales logarithmic to the activation overpotential, a small change in overpotential (or reaction conditions) gives a high change in current. Opposite, if the current is constant, any change in reaction conditions will only cause a small change in the required activation overpotential. This requires that the reference electrode is actually placed near the surface of the catalyst, but the cells available in our lab only allows for the reference electrode to be placed on the anode side, either inserted into the flow channels or in the electrolyte inlet tube (using a tee). The same cannot be done on the cathode side, since it requires an ionic contact which is (obviously) not provided by the gas stream. The measured (or controlled) potential between working electrode and the reference electrode

[1] I guess it would technically be a galvanostat then, but I will keep refereing to it as a potentiostat

is therefore a convolution of the thermodynamic potential, the activation overpotential and the ohmic overpotential caused by resistance in the membrane.
When the current density becomes sufficiently large, the linear nature of the ohmic overpotential causes it to dominate any changes in the total overpotential. An example of this can be seen in fig. 3.5 where the current density is gradually increased to $100\,\mathrm{mA\,cm^{-2}}$ in steps of $10\,\mathrm{mA\,cm^{-2}}$, and later jumped to $200\,\mathrm{mA\,cm^{-2}}$. Initially the potential increases logarithmically (fig. 3.5a), but from around 50 to $100\,\mathrm{mA\,cm^{-2}}$ it begins to increase linearly.

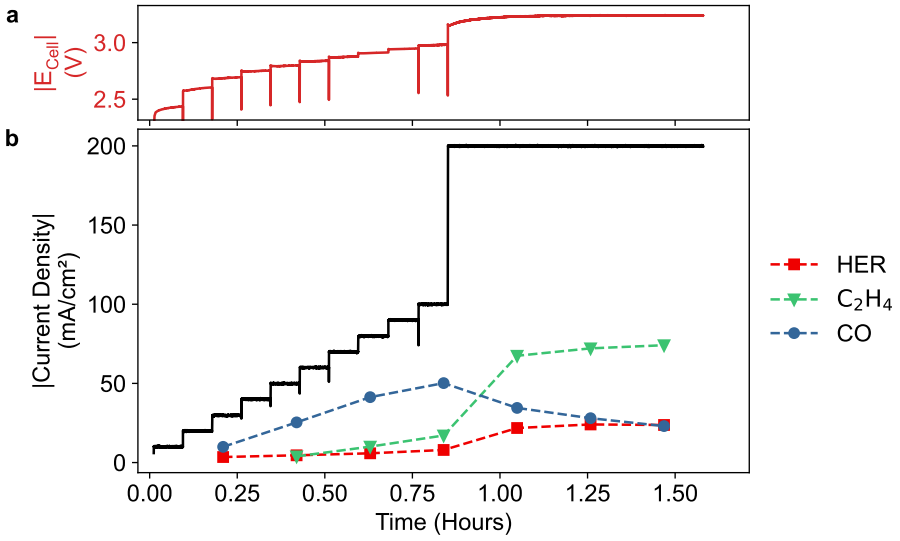

Figure 3.5: *The plot shows the result of an experiment using the normal Cu GDE. The current density (black), plotted in b, was gradually increased to* $100\,\mathrm{mA\,cm^{-2}}$ *in steps of* $10\,\mathrm{mA\,cm^{-2}}$*, and later jumped to* $200\,\mathrm{mA\,cm^{-2}}$*. As seen by the cell potential in a, the potential initially increases logarithmically with current, but transitions to a linear dependency above* $50\,\mathrm{mA\,cm^{-2}}$*.*

Therefore, there is no loss of information obtained by operating at constant current. Actually, it lowers the uncertainty of the FE and partial current density, since there is a volume between the cell and the GC, causing both a delay and some blurring in the gas composition. Variations in the current therefore makes it more cumbersome and imprecise to relate the (average) current to the gas concentrations measured by the GC.

3.5.2 Selectivity Dependence on Current

The experiment shown in fig. 3.5, is also a great example of how the selectivity towards C_2H_4 increases at higher current density. When the current is increased from 100 to $200\,\mathrm{mA\,cm^{-2}}$ the partial current density for C_2H_4 increases significantly, whereas the partial current density for CO decreases. This is expected to occur as the higher current increases the CO coverage on the catalyst and thereby increases the C – C coupling probability.
The sum of all partial current densities does not match the total current density, leading to a total FE significantly less than $100\,\%$. There are two reasons for this. First of all, no liquid analysis has been included here, and other experiments have shown that quite a lot of liquid products are produced. Since it is technically difficult and somewhat cumbersome to get liquid samples through out the experiment, and because my focus has been on C_2H_4, most of my experiments did not include analysis of liquid samples, and have not included data for liquid products in the experiments where it was done.
The second reason for the missing FE is products crossing over to the anode. If a product crosses to the anode side, it is likely to get oxidised. This effectively acts as a "chemical" short-circuit between the two sides. When a (carbon based) product is oxidised, CO_2 is formed instead of O_2, and when looking at the FE for O_2 at the anode side, it generally tends to be around $80\,\%$. The total FE on the anode side should therefore not sum to $100\,\%$, but to the FE for O_2 on the anode side.

3.6 The Gas Supply System

The gas supply system was extended with an additional MFC and a gas manifold, fig. 3.6a, where N_2, Ar, H_2, CO_2, and CO can be directed to MFC - A or MFC - B through an on-off three-way valve (middle position is off). Each incoming gas line is protected by a needle valve and a check valve. The check valve prevents accidental back flow from one gas line to another (e.g. CO_2 into the CO line which has a lower pressure), and the needle valve creates a two step process minimising the risk of opening a wrong gas line. A sixth three-way valve with an HL flow path (middle position connects all three ports) provides the possibility of either connecting a local gas bottle (e.g calibration gas) to line A or B or, when in middle position and the needle valve is closed, connecting line A to line B, so that the same gas (e.g. CO_2) can be supplied to both

MFCs. Downstream of the MFCs three valves makes it possible to either mix the flows into one line, or to send one (or both) flow through a water filled aluminium tank acting as a humidifier. The outlet of the humidifier is then merged with the other gas line before going into the cell. This allows for the possibility of lowering the level of humidification, as dry and humidified gas can now be mixed.
A pressure sensor was mounted on the dry gas line to avoid the high humidity, but the inlet pressure of the cell is still measured independent of the flow path. An illustration of the dual gas line setup can be seen in fig. 3.6b.

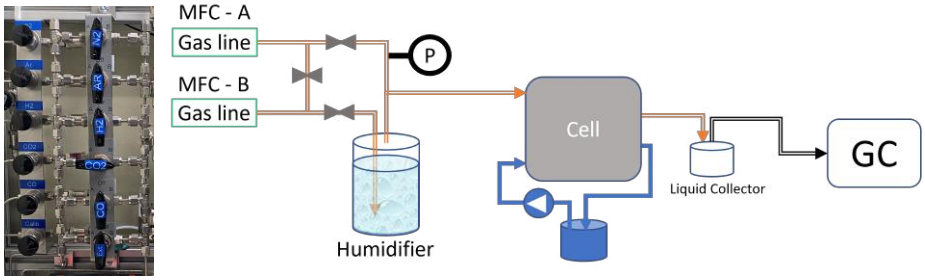

(a) *Manifold* **(b)** *Sketch of setup*

Figure 3.6: *Fig.a shows a picture of the new gas manifold, enabling a selection of various gasses into MFC - A and MFC - B. Fig.b is a sketch of the setup with an extended gas system.*

3.7 Humidification of CO_2

Since H_2O is consumed in the reaction for hydrogenation of CO into hydrocarbons, water must be provided somehow. Either diffusion of electrolyte through the membrane acts as a water source, or the inlet CO_2 can be humidified, by bobbling it through water. At the same time, flooding of the GDE is expected to be a significant cause for loss of selectivity towards CO_2R, indicating that too much water can be supplied. It was therefore interesting to investigate if changing the humidity of the inlet gas would affect the performance.
The possibility to send part of the inlet CO_2 through the humidifier, allowed for a controlled lowering of the humidification. Through out many of the initial experiments, I did use various degrees of humidity,

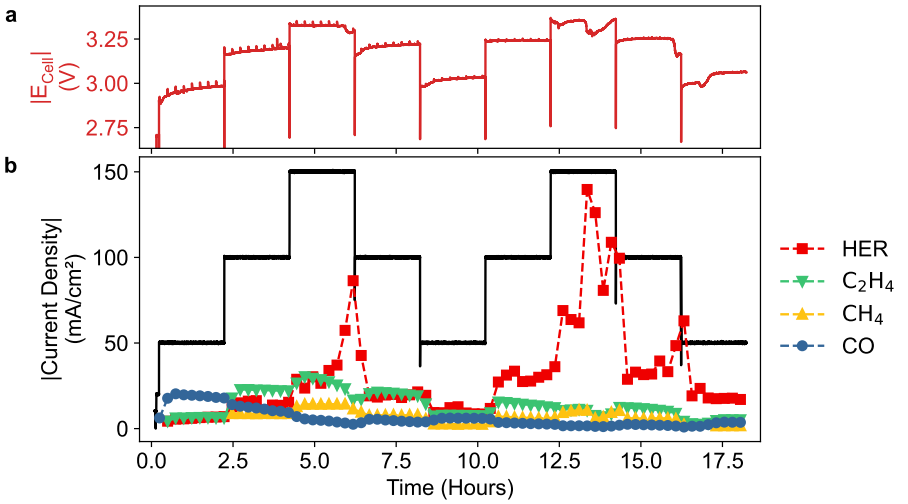

Figure 3.7: *The plot shows an experiment where the humidifier was mounted in the system, but not used. Small spikes were observed in the potential, correlating with the GC injections. They are expected to be caused by the headspace volume of the humidifier.*

but it never seemed to cause any observable change. Maybe, it was because other factors were influencing the reaction more.
This is in accordance with recent findings in literature, showing that at current densities below $400\,\mathrm{mA\,cm^{-2}}$, the main water source is through the membrane[34]. The humidity of the inlet gas can though influence the reaction in other ways. Studying CO_2 to CO electrolysis, Wheeler *et al.*[35] comes to the conclusion that a hydrated feed gas prevents salt precipitation and increases stability. While this might be correct, and though there is a possibility, that humidification might be important at higher currents or elevated temperatures, I did not see any improvement by using a humidified gas stream. Contrary, I observed some influence from the humidifier related to the GC injections.

3.7.1 Pressure Effects from the Humidifier

Figure 3.7 shows one of the experiments where the humidifier was in the system, but not used. In this case the gas was lead around the humidifier, but it is still connected to the inlet, so the head-space in the humidifier acts as a buffer volume on the inlet stream.
In this fairly long experiment, the current was ramped up and down in

order to see if the selectivity towards CO_2RR was regained at lower current density, or if the high HER was a sign of a permanent degradation. Again, it is seen how CO dominates at low current densities, and the partial current density for C_2H_4 increases at higher currents. It can also be seen, that when there is a high selectivity towards HER, the partial current density for CH_4 increases.

When looking close at the potential in fig. 3.7a, a series of small spikes can be observed clearly correlating with when the GC takes an injection. A close up of can be seen in fig. 3.8. As mentioned earlier, the GC creates a significant overpressure, caused by a flow restriction in the sampling valves. When the GC injects, the restrictions is decreased and the flow increases. Without the humidifier, the change in flow into the cell is not significantly affected by this change in pressure, but when inserted the humidifier acts as a buffer volume before the cell, and thereby causing an increase in inlet flow, when the pressure drop across the GC changes. It is unknown why this flow change causes fluctuations in the cell voltage, but I expect that it is either a direct effect of the sudden flow change, or a change in compression of the MEA when the flow, and expectedly the pressure, in the flow channels increase.

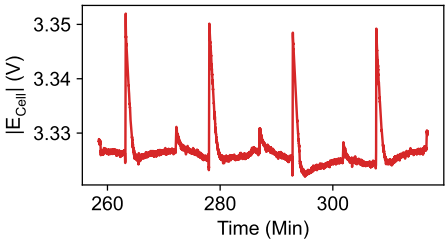

Figure 3.8: *Zoom in on the potential spikes in fig. 3.7a.*

Clearly, the spikes get smaller as the experiments proceeds. Mostly, they seem to diminish when there has been a spike in HER. I would assume that this is because salt precipitations in the flow field (and GDE) changes the flowpath, creating a restriction inside the cell itself. Any change in outlet pressure will therefore not affect the inlet flow nearly as much. Some larger and slower fluctuations is also observed when the H_2 peaks, these will be discussed in chapter 5.

3.8 Measuring the Outlet Flow

The GC measures the concentrations of the different gasses but what we are interested in is the partial current density or FE. The measured concentrations must therefore be converted to a molar flow, and subsequently to partial current. The molar flow is given by the concentration times the outlet flow, but this is not necessarily identical to the inlet flow. Several things things can cause it to deviate. A direct change of the flow can as mentioned earlier have causes such as pressure changes, flow blockage or leakage. A more indirect change can be caused by the electrochemical reactions themselves. There is of course the direct consumption and conversion of CO_2 causing a possible decrease in outlet flow. A high activity of HER will cause an increase in outlet flow given that none of the inlet gas is consumed in this reaction. Furthermore, the reaction between OH^- and CO_2 can create a shuttling of CO_2 from the cathode side to the anode side. As shown in literature, this can can cause a deviation between the outlet and inlet flow, resulting in a significant overestimation of the FE[20,21]. It is therefore important to accurately measure the outlet flow of the cell, at the time of the GC injection.

While the most common way of measuring gas flow is by using a Mass Flow Meter (MFM) based on thermal conductivity, this requires either a well known gas composition or a rigorous back calculation, since the thermal conductivity of different gasses varies significantly. Hydrogen for instance, have a thermal conductivity one order of magnitude higher than CO_2. Varying humidity can also cause the thermal conductivity to deviate from expected, making it a somewhat uncertain method.

What is needed is a volumetric flow measurement, and for short experiments, the simplest way is the low tech soap bobble flow meter and stopwatch, but this is of course not viable when doing experiments over many hours[II]. Digital VFM exists, and we have been testing some in our lab, one was based on a buoyancy principle, where a lever in a water filled reservoir tipped when enough gas had entered, but the precision was not very good. Another was based on the displacement of a small piston, and a pressure measurement. While this one had a fairly good precision, it does not tolerate high humidity, and often the piston got stuck due to the high humidity of the outlet gas. Further more, both

[II]Well, I did have more spare time when the COVID pandemic put an end to social activities, but timing soap bubbles for 10 h was a bit of a streatch.

of them have a somewhat low time resolution, making it problematic to determine the actual flow at the time of the GC injection, given the large variations in flow cased by the GC (as seen in fig. 3.3a). The best solution seem to be an internal flow reference in the GC.

3.8.1 Internal N_2 Flow Reference

What can be described as an internal flow reference can be made by placing a bleed line of e.g. N_2 right before the GC. If the flow of N_2 is known, the total flow into the GC can be determined by the concentration of N_2. For any compound x the GC peak area (α_x) equals the gas concentration (c_x) times a GC calibration constant (k_x) for the given gas:

$$\alpha_x = k_x \cdot c_x \quad \Leftrightarrow \quad k_x = \frac{\alpha_x}{c_x} \quad \Leftrightarrow \quad c_x = \frac{\alpha_x}{k_x} \tag{3.3}$$

While the calibration constant might deviate slightly at very high or low concentrations, it can be regarded as a constant in all practical ranges regarding CO_2E. By using a calibration gas with appropriate concentrations, it is possible to determine the calibration constants for the different gasses of interest. And the concentration of a given gas in an injection can thereby be determined.
The volumetric flow of a gas ($\dot{V}_x$) equals the gas concentration times the total volumetric flow ($\dot{V}_T$):

$$\dot{V}_x = c_x \cdot \dot{V}_T \tag{3.4}$$

It is therefore possible to determine the volumetric flow of a gas from the measured GC peak area, if k_x and $\dot{V}_T$ is known. This is of course also true for N_2, and if the volumetric flow of N_2 is known, it is possible to find the total volumetric flow:

$$\dot{V}_x = \frac{\alpha_x}{k_x} \cdot \dot{V}_T \quad \Rightarrow \quad \dot{V}_{\mathrm{N_2}} = \frac{\alpha_{\mathrm{N_2}}}{k_{\mathrm{N_2}}} \cdot \dot{V}_T \quad \Leftrightarrow \quad \dot{V}_T = \dot{V}_{\mathrm{N_2}} \cdot \frac{k_{\mathrm{N_2}}}{\alpha_{\mathrm{N_2}}} \tag{3.5}$$

thus, it is possible to determine the volumetric flow of a gas, from the GC peak area if the volumetric flow of N_2 is known:

$$\dot{V}_x = \frac{\alpha_x}{k_x} \cdot \dot{V}_{\mathrm{N_2}} \cdot \frac{k_{\mathrm{N_2}}}{\alpha_{\mathrm{N_2}}} \tag{3.6}$$

Assuming that all the measured gasses are somewhat ideal, the volumetric flow of a gas is interchangeable with the molar flow of a gas:

$$\dot{n}_x = \frac{\alpha_x}{k_x} \cdot \dot{n}_{\mathrm{N_2}} \cdot \frac{k_{\mathrm{N_2}}}{\alpha_{\mathrm{N_2}}} \tag{3.7}$$

This method has the benefit that the gas flow is determined at the exact time of the injection, but on the down side, it also does not provide any information about the flow in between the GC injections.

Since the pressure before the GC varies between the injections, it is important to place the N_2 MFC very close to the GC. I have typically used a nitrogen flow of $1\,\mathrm{mL\,min^{-1}}$, and of the volume of the piping between the N_2 MFC and the GC is of a comparable size or larger, it acts as a buffer volume causing variations in the actual N_2 flow merged into the sample gas stream.

3.9 Heating the System

There are various ways to heat an electrolysis cell like this. The simplest way is to heat the cell alone, either by adding a heating element directly to the flowfield, or heat up the electrolyte. While the first option is significantly better than the second, both of the methods suffer from the problem, that heat dissipation and gas supply (especially if humidified) can cause local variations in temperature in the cell. The somewhat more complex, but also superior way, is to place all possible elements inside an oven or a heating box.
As it was desired to be able to perform both CO_2E as well as COE experiments, a certain amount of safety consideration had to be made. It was either an option to build a ventilated chamber for an oven, or place a heating box inside a fumehood. As seen in fig. 3.9, we decided on the last option.

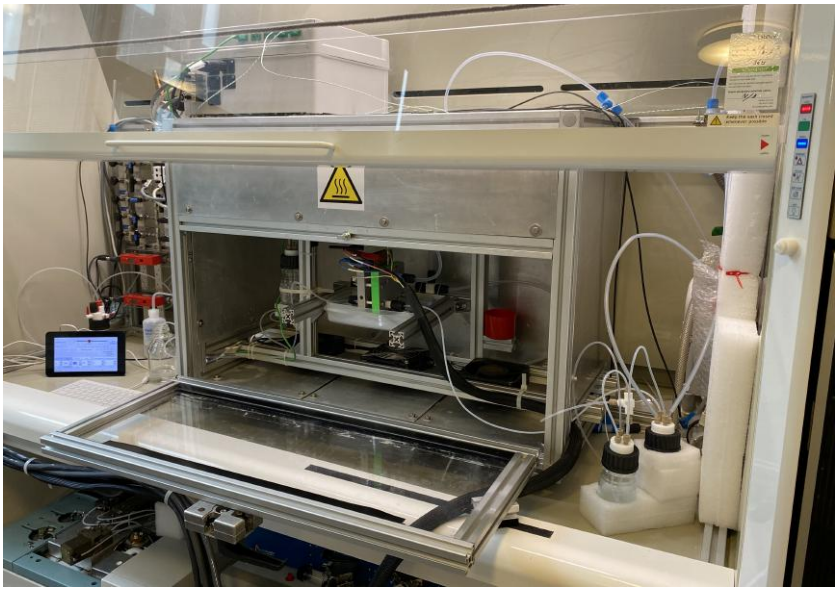

Figure 3.9: *Picture of the heating box in the fumehood. The cell, electrolyte and optionally a humidifier can be placed inside the box, to ensure a uniform heating of all elements.*

The heating box consists of a frame made with Bosch RexRoth profiles. The frame is covered with aluminium plates on the inside and outside, and insulation placed in between. Three 400 W heating pads are attached to the inner bottom plates on the side facing towards the insulation. These plates are insulated from the frame to minimise heat dissipation to the frame. A fan is placed over each of the heated plates to enhance heat distribution. A Raspberry Pi adjusts the heating power by turning the power on and off in a 10 s Pulse Width Modulation (PWM) cycle. The temperature can then be controlled either by setting a constant pulse width or through a Proportional Integral Derivative (PID) control, based on the measured temperature. The temperature is measured in multiple placed, but the control temperature is measured by a thermocouple placed inside the cathode flowfield. When operated at 100 %, the temperature reaches around 90 celsius after 1 to 2 h, at 50 % it reaches around 65 celsius after 30 to 45 min. In all heated experiments the power was turned on in advance, so the temperature was somewhat steady at the start of the experiment.

3.9.1 First Heated Experiment

Figure 3.10 shows an experiment performed at approximately 60 °C. A small amount of CO, and only minor if any signs of C_2H_4 or other CO_2RR products were detected.

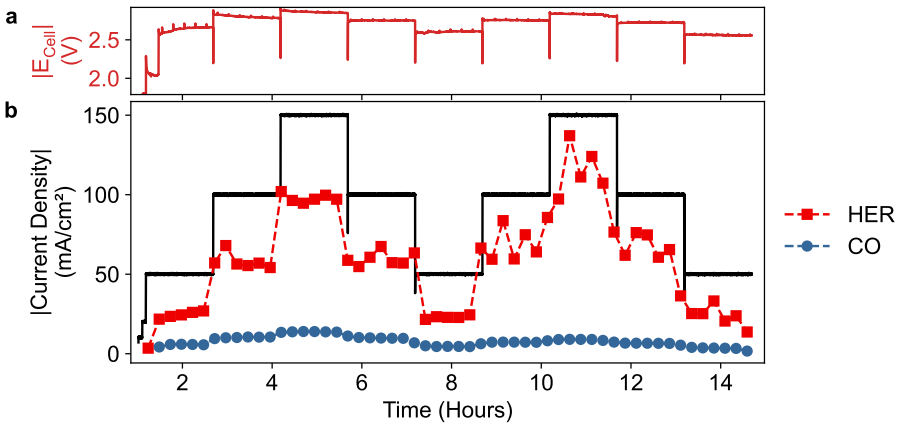

Figure 3.10: *First heated experiment. Performed at 60 °C. Only H_2 and small amounts of CO were detected.*

ardu It was assumed that the lower solubility of CO_2 at the increased temperature, was causing a mass transport limitation of CO_2. Two strategies was attempted to overcome this problem. One was to use an all PTFE filter membrane as GDL, hoping it would minimise flooding. The other was to operate at higher pressure, to counteract the lower solubility at higher temperature.

3.10 PTFE Based GDE

Inspired by the $1\,\mathrm{A\,cm^{-2}}$ paper by García de Arquer *et al.*, I decided to try and use a PTFE based membrane as GDL. In the paper, they use a PTFE substrate with a mean pore size of $450\,\mathrm{nm}$, but the only PTFE filter membranes I had available was with a pore size of $1.5\,\mu\mathrm{m}$ (Merk 58086). None the less, it was worth a try, and Cu was therefore sputtered onto the membrane.
As a start, I needed to see if it performed as good as the normal GDE at room temperature. Since the substrate is non conducting, a direct contact from the flowfiled to the Cu layer was necessary. Initially I attempted to use an Al film placed over the PTFE GDE. The reason for using Al foil, was to minimise the risk of adding any metal that could act as a catalyst. It did work initially, and for a few hours it performed decently, but not as good as the normal GDE. When disassembled, the Al foil was clearly dissolved as seen in fig. 3.11a. As an alternative strategy to create the front contact, I decided to use Cu tape. While this did increase the possibility of creating a larger (geometric) area catalytically active, I tried to overcome this by adding a piece of Kapton tape on top of the Cu tape, as seen in fig. 3.11b. This experiment also performed decently, and for a longer duration, but still not as well as the normal GDEs. I expect that the low performance was caused by the large pore size, and never attempted to use another PTFE substrate. Instead I pursued the strategy of pressurising the setup.

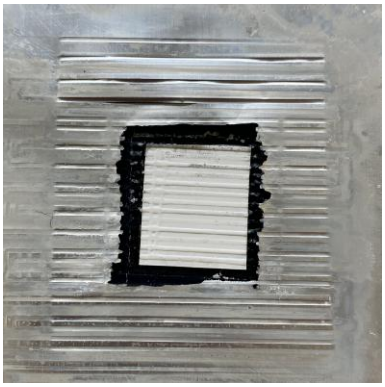

(a) *Al foil dissolved.*

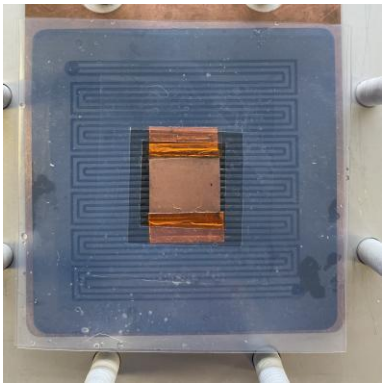

(b) *Cu tape as front contact.*

Figure 3.11: *Attempts of making a front contact to PTFE based GDE. a shows the backside of the PTFE GDE after the experiment, with the rest of the Al foil used for creating the contact. As seen the Al was clearly dissolved. a shows how a front contact was instead made using Cu tape. To restrict the geometric area, the Cu tape was insulated using Kapton tape. While this method worked well, the GDE never performed as hoped.*

3.11 Pressurising the Setup

A set of old analogue back pressure regulators from MKS were installed on the gas outlet lines, after the liquid collector and electrolyte reservoir. The were made digitally controlled in the same way as the pumps.
by using an Arduino Nano Every as a $5\,\mathrm{V}$ DAC. Attempts were made to increase the pressure, but only a small overpressure were obtainable without the membrane breaking. It became clear that since there is no intrinsic flow on the anode side, and the produced flow of O_2 and cross over CO_2 is fairly small, the back pressure regulator did not have enough gas flow to maintain the pressure.
To overcome this, an Ar line bobbling into the electrolyte was added. The higher anode flow also enabled a better GC detection of the anode gas. The full setup can be seen in fig. 3.12.

3.11.1 Heated and Pressurised Experiments

Figure 3.13 shows an experiment performed at$65\,^{\circ}\mathrm{C}$ and $500\,\mathrm{mbar}$ overpressure on both sides. An improvement in especially C_2H_4 FE was ob-

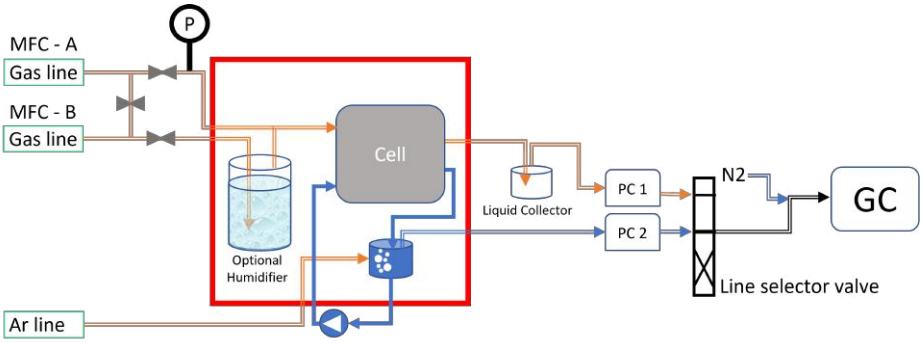

Figure 3.12: *The (almost) final setup, including the heating box (red), an Ar line to the anode, back pressure regulators (first version), and a selector valve as well as an N_2 bleed line going to the GC.*

served, but not very much. Unfortunately, the experiment did stopped after $4.5\,\mathrm{h}$ as the membrane broke. Indicated by the high CO_2 to O_2 ratio measured on the anode, it was clear that gaseous CO_2 was crossing over to the anode side, and that there had been a significant pressure difference between the two sides inside the cell. After multiple attempts, I found that the connection between the tubing and the anode flowfield was leaking at high overpressure. Despite many attempts to fix this, I was clear that a new cell was needed if the pressure should be increased further.

The back pressure regulators were also not performing as hoped. First of all, the placement of the cathode back pressure regulator down stream of the jar used for liquid collecting liquids caused problems. The difference in regulated volume between the two sides was a problem, and since the regulator cannot tolerate liquids, it could not be moved upstream of the liquid collector. The home made digital control, was also not stable enough. Small glitches and noise in communication between the Raspberry Pi and the Arduino, would case one of the pressure regulators to loose pressure from time to time. An other solution for back pressure regulators were therefore needed.

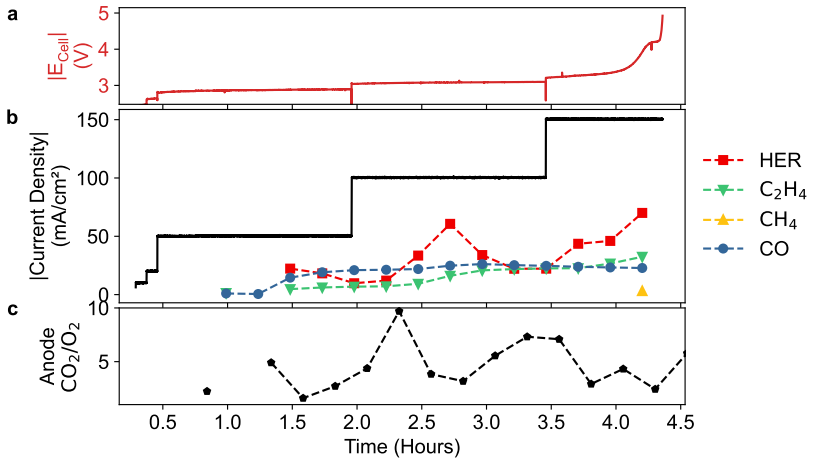

Figure 3.13: *Heated and pressurised experiment performed at* $65\,^{\circ}\mathrm{C}$ *and* $500\,\mathrm{mbar}$ *overpressure on both sides.*

3.12 New Back Pressure Regulators

Later on a new set of dome loaded back pressure regulators from Equilibar (LF Series Precision) was mounted. These back pressure regulators does not measure the pressure directly on the gas stream, but regulates the flow using a diaphragm compressing on a set of orifices. An externally controlled pilot pressure presses the diaphragm down, and opens only if the pressure of the regulated gas stream is higher than the pilot pressure. These all mechanically pressure regulators can therefore be made completely in peak and with a diaphragm of suitable material (in our case the type PGL4.2). They can also regulate on both gas and liquid and it was therefore possible to mount the cathode regulator right after the cell. The pilot pressure was controlled using a dual valve pressure controller model PCS-DRP70. The electronics were exchanged with a more robust system from Widgetlords Electronics (WL-MIO).

The use of the new pressure controllers is presented in chapter 8. This is because the work on heated and pressurised experiments were postponed a for a while, as loosened COVID restrictions allowed us to get a beamtime at the European Synchrotron Radiation Facility (ESRF). The focus was therefore shifted towards operando investigation of the CO_2E.

Chapter 4

Cell Design & Data Analysis for X-ray Operando Experiments

My Contributions

The original cell design was made by the staff at ESRF ID31 and their collaborators. The redesign was done in close collaboration with my colleague Sahil Garg in an iterative process. Most of the drawing and design was done by me, while he focused on performing electrochemical tests.

This page intentionally left blank.

4.1 Chapter Introduction

X-ray analysis of GDE based cells can fundamentally be divided into two groups with respect to the geometry of the experiment. One case is where the electrode is placed perpendicular to the beam, the other is grazing incident geometry where the electrode, or MEA, is placed parallel to the beam. The benefit of placing the cell perpendicular to the beam, is that it provides localised information across the GDE. While interesting studies in literature has used this geometry to investigate bubble formation and electrolyte distribution in a CO_2E flow-cell setup[36], this geometry only provides information of all layers in the cell as an average and is unsuitable for investigating (zero gap) MEA cells with a (full) GDE on both sides. The relative large X-ray pathway through the cell also limits the possibility of obtaining valuable information from the thin catalyst layer. The grazing incident geometry on the other hand, not only allows analysis at different heights of the MEA, but also crystallographic information due to the much larger interaction volume, e.g. with the catalyst layer. The down side is, that the information obtained, to a large extent is an average over the width of the GDE.
The classical MEA cell design is not suitable for X-ray experiments, and it was therefore necessary to design a new cell for these experiments.

4.2 Designing a Cell for X-ray Experiments

The cell was designed with elongated flowfields to allow for the scattered X-rays to exit the cell unhindered. The size was also decreased, mainly to minimise parallax effect (see section 4.2.4). The size should though be comparable to the typical MEA. As a compromise the GDE size is circular with a diameter of $9\,\mathrm{mm}$ and thus and area of $63.6\,\mathrm{mm}^2$. The circular shape was chosen to enhance the capabilities for X-ray Diffraction Computed Tomography (XRD-CT), as this minimises potential reconstruction defects.

Figure 4.1: *Original cell design. The metal inlets in the ends and the electrical connections needed to be redesigned.*

Each flowfield was attached to an endplate connecting to the gas/liquid tubes. The flowfield can be manufactured in a material suitable for the purpose, but in our case the cathode was made of graphite and the anode of Ti. The two flowfields are inserted into a Polyether Ether Ketone (PEEK) casing which does not diffract X-rays in sharp peaks.

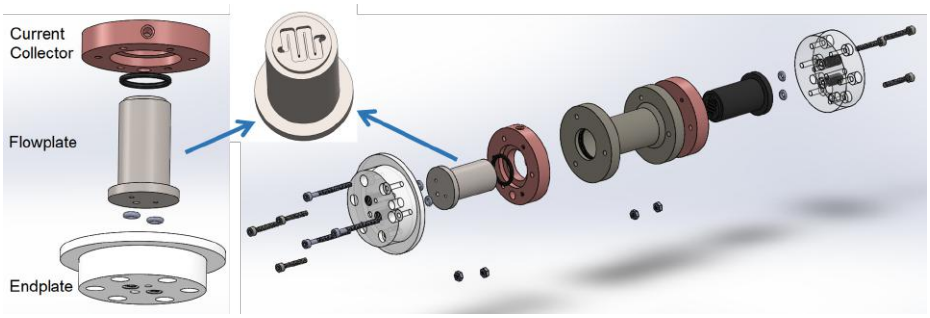

Figure 4.2: *Exploded 3D drawing of the final flowfield (left) and the cell (right). The insert shows the flowplate with a single-channel serpentine flowpath.*

4.2.1 Improvements to Initial Design

The initial design was made by our collaborators at ESRF, but further development was needed as it was unsuited for CO_2E. The main problem was the metal inlet connectors causing contamination (see section 3.4.2), but also problems with leakage and unstable electrical connections to the flowfields had to be solved.

The solution was to redesign the end-parts of the cell, but reuse the flowplates and casing. The fixation ring was exchanged with a Cu version now also acting as a current collector. The metal inlets were exchanged with a small 6-40 thread version of the superflangeless ferules from Idex (M-650 ferrules and M-644-03 nuts) for 1/16" tubing, and the endplates were redesign to match these. To speed up the iterative design and test process, the endplates were manufactured by high precision 3D printing. The 3D print material (VeroClear™RGD810™) is not compatible with KOH, meaning that any contact between the 3D printed material and the electrolyte would inhibit the use of the cell for COE. To solve this, the PTFE tubes were extended all the way into the flowplates where an O-ring ensured a leak-free sealing. To ease the assembly procedure, a $200\,\mu m$ thick gasket was used to stabilise the membrane. An exploded 3D drawing of the final flowfield and cell can be seen in fig. 4.2.

4.2.2 Grazing Incident Geometry

The cell was placed in the high energy ($68\,\mathrm{keV}$) micro sized beam ($5\,\mu\mathrm{m}$ vertical by $20\,\mu\mathrm{m}$ horizontal) at a distance of approximately $70\,\mathrm{cm}$ from the 2D detector (Dectris Pilatus CdTe 2M), as sketched in fig. 4.3. The detector distance was calibrated using a CeO_2 standard mounted on the side of the cell in a position corresponding to the center of the MEA. The cell was mounted in a 6-axis motorised stage, allowing both alignment as well as precise movement in order to probe the different parts of the MEA. Electrical, liquid and gas connections were placed in a way that allowed $360°$ rotation without anything entering the beam path, and thereby making it possible to tomography experiments.

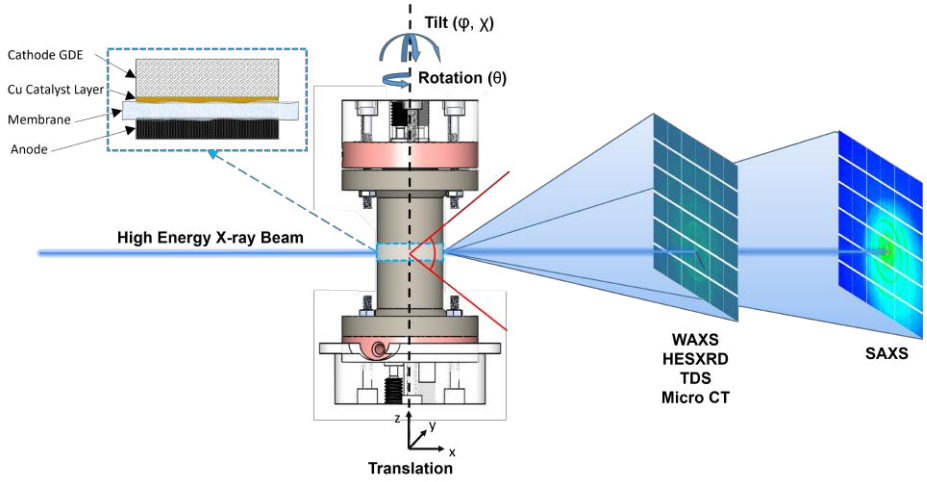

Figure 4.3: *Illustration of the cell placed in the beam path. The left top corner insert in shows the placement and orientation of the MEA. The cell can be positioned in the beam, by translation and tilting, so different parts of the MEA can be investigated. The wide opening of the cell design allows X-rays to exit unhindered as illustrated by the red lines. The circular design is chosen to minimise reconstruction defects in tomography experiments.*

4.2.3 Alignment

It is important that the MEA, and thus the cell, is aligned correctly, so the Cu layer is parallel to the beam. In order to align the cell, we made a set of Region Of Interests (ROIs) integrating parts of the detector signal. The ROIs where covering parts of the Cu and graphite debye rings respectively and thereby allowing us to monitor the Cu and graphite signals directly. Since the intensity of the scattered signal is proportional to the interaction volume between the beam and the material causing the scattering, e.g. graphite, we could use the geometry of the serpentine flow channel and surface of the polished graphite flowfield to align the cell. By performing a horizontal scan across the serpentine flow channel the position of the different lands could be determined, since the signal from the lands would be higher than the signal from the channels. If the cell was slightly rotated the graphite signal of the lands would be triangular rather than showing a square form. In this case the cell was rotated slightly and new scan was performed. This procedure was repeated until the flow channels were parallel to the beam. The cell was then moved to the center bringing one of the lands in the center in focus.

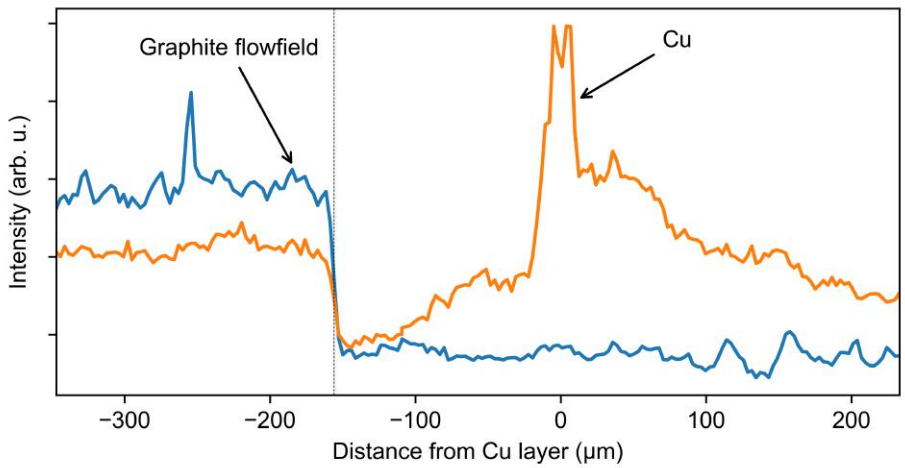

Figure 4.4: *The figure illustrates how the surface of the graphite flowfield was used to align the cell. The more parallel the cell is to the the beam, the steeper will the graphite intensity step at* $-145\,\mu\mathrm{m}$ *(dotted line) be. The orange line shows the intensity of the Cu signal, indicating the position of the catalyst layer.*

A fairly large ($\approx 1\,\mathrm{mm}$) vertical scan was used to find the position corresponding to the surface of the land, which was then brought into focus. A small vertical scan with smaller steps size, i.e. spatial resolution, was used to determine the tilt of the cell. If the surface is in plane with the beam, a steep decrease in the graphite signal should occur as the land is moved out of the beam. A more gradual decrease occurs when the interaction volume between the land and the beam changes with height indicating that cell is tilted. An example can be seen in fig. 4.4, where the blue curve corresponds to the graphite signal. A steep decrease can be seen at the position of the dotted line.
While the slope of the graphite signal to some extent indicates how much the cell is tilted, it does not indicate the direction of the tilt. A series of smaller and smaller tilts to both sides, each followed by a line scan, was therefore used to find the correct tilt angle where the cell is aligned. This iterative procedure took quite some time, especially if the initial position of the cell was very misaligned.
Since the alignment procedure had to be done after the cell assembly, but before the experiment was started, there was a risk of the membrane getting dry which can influence the performance. Increased experience in placing the cell did shorten the alignment time, but it was clear that this could be improved by changing the cell design slightly. The stage, in which the cell is mounted, is a cylinder with three screws used to fasten the cell. And after the first beamtime, I modified the design of the endplate by adding a collar and increasing the diameter of the anode endplate, so that it would fit perfectly in the top of the cylinder.

4.2.4 Peak Split from Parallax Effect

Since the diameter of the cell is not negligible compared to the distance to the detector, some degree of parallax effects was observed. This is best seen when the beam enters the surface of the flowfield in a channel. Here a set of split peaks from the graphite flowfield can be observed (most noticeable around $5.1\,\text{Å}^{-1}$). The split peaks are placed symmetrically around the expected peak position, and it is actually not a split, but rather a set of peak shifts.

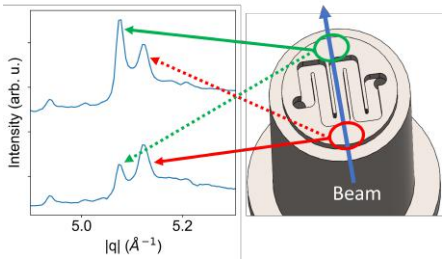

Figure 4.5: *Example of a peak split caused by the parallax effect.*

Because the two ends are distanced differently from the detector, the graphite peak is shifted slightly towards lower q for the end close to the detector and towards higher q for the end further from the detector, thus causing the observed split. An illustration can be seen in fig. 4.5. If the cell is just slightly tilted, the two peaks can be seen to increase differently in intensity as the flowfield is moved into the beam. This happens because one end enters the beam before the other.

Other elements in the cell and MEA, e.g. the Cu layer, will show similar effect, but if the scattering element is continuously distributed along the beam path, it will cause a peak broadening rather than a shift. In other words, since the magnitude of the peak shift depends on the distance from the center, a continuous film will cause a continuum of peak shifts, effectively seen as a broadening. The parallax effect is also one of the things causing a limitation on the cell size. A much wider cell would cause significant peak broadening, and thereby limit the resolution of the measured reciprocal space. Even in this moderately sized cell, this is a limitation that should be taken into account, especially if the cell is used for XRD-CT or if more complex analysis and refinements are made.

The parallax effect is not purely a bad thing. Some information can be obtained from the peak shifts and broadening, as it contains information about the relative position of the scattering event. However, one should be careful, since multiple things can cause similar peak shifts and broadening.

4.3 Analysing Large Operando WAXS Datasets

During the operando experiments, the cell was moved vertically in small steps and a WAXS pattern was recorded at each step. The cell was then moved back and the process was repeated. This allowed a repetitively probing of different heights in the GDE. Each vertical scan consisted of 50 steps, and thus patterns, and was repeated approximately every $1.65\,\mathrm{min}$. A $150\,\mathrm{min}$ experiment would therefore give somewhere in the order of 4500 patterns. With this amount of data, it is near impossible to inspect every pattern, at least while keeping an overview. While it is somewhat straight forward to get a computer algorithm to manipulate and plot such amount of data, such bulk processing bares risk of of either missing important changes or in worst case make inaccurate conclusions. To overcome this problem, I developed a python script with an interactive plot that makes it easy to inspect every pattern as well as analyse and visualise the dataset. The script was named Python For X-ray Operando Analysis (pyXop), and will be referred to as such.

Before analysing the data with pyXop, the raw 2D detector data was integrated to 1D patterns using the pyFAI software[37]. For the data obtained at the first beamtime a sigma clip algorithm was used to smooth the data, to removing random spikes from the gasket material. For the second beamtime the data was not smoothed.

The 1D patterns and metadata containing position and time for each pattern was loaded into pyXop, and the interactive plot was generated. An example of the interactive plot can be seen in fig. 4.6. The cell potential is plotted at the top (fig. 4.6a), but is only included for reference. The main parts are the contour plot in the middle (fig. 4.6b) and the pattern plot in the bottom (fig. 4.6c). The contour plot has (arbitrary) height on they y-axis and time on the x-axis. The intensity is obtained by integrating every pattern in a selected q-range. In this case a q-range around the main Cu peak has been selected, and the contour plot therefore shows the Cu content at different heights (of the MEA) vs. time. The q-range can be selected by a (left) click and drag on the pattern plot below, indicated by the two red lines. When a new range is selected, the contour plot is updated. When the mouse is moved around on the contour plot, the pattern plot is continuously updated showing the pattern corresponding to the given height and time of the mouse location. In the example shown the mouse is located in the Cu layer, and as seen in the pattern, all

expected Cu peaks are present. Reference patterns downloaded e.g. from ICSD can be imported and overlaid as a guide. The different imported reference patterns can be toggled on an off in the side panel.

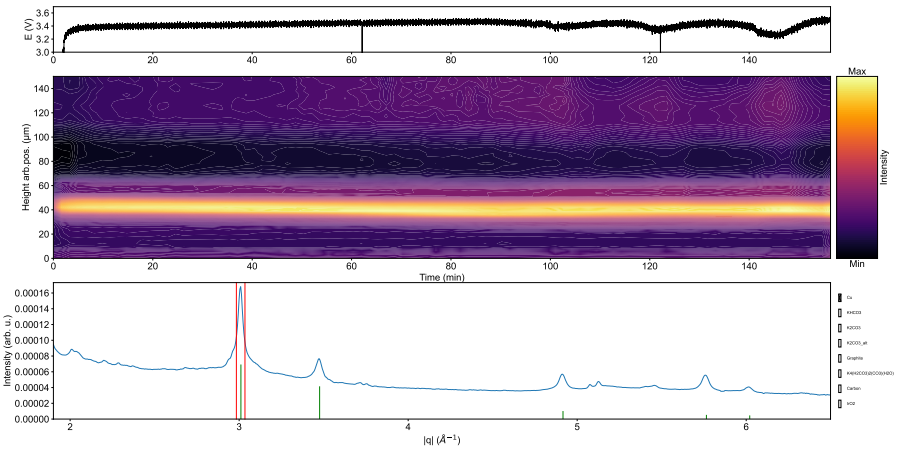

Figure 4.6: *Screen print of the interactive pyXop plot. The cell potential is plotted at the top (a). The main parts are the contour plot in the middle (b) and the pattern plot in the bottom (c). The contour plot shows the integration of each pattern in the range of the area selected on the pattern. The pattern plot is updated when the mouse is hovered over the contour plot, and shows the 1 D pattern corresponding to the mouse position.*

4.3.1 Detecting Water with WAXS

As anything else, water scatters X-rays, but given the lack of crystallinity, the scattering does not give sharp Bragg peaks (or Debye rings), but a set of very broad and overlapping peaks, resulting in a broad background in the q-range around 2 to 5 Å^{-1}, peaking around 2 Å^{-1}[38,39].
Therefore, an increase in water content can be detected as an increasing in the background signal. All though the water content is not easily quantifiable, the background must be proportional to the water content as it seems unlikely that any other component of the cell should give such an increase in background.

One possibility would be to subtract the first scan from the rest, and integrate the full spectrum in an attempt of visualising changes in back-

ground. While this approach is applicable when no crystalline phases are evolving, it can not be used in this case where salt is expected to be precipitating (and dissolving). Instead, part of the background is integrated in a q-range where there are no Bragg peaks, making it possible to qualitatively visualise electrolyte content, or at least changes hereof, in the different layers of the GDE as the time evolves.

4.3.1.1 Separating Salt & Electrolyte Content

A similar problem occurs when determining salt precipitations. This is done by integrating around a peak from the given salt, but as the background also changes, this leads to a combination of (crystalline) salt and electrolyte content. To solve this, a functionality for subtracting an integrated part of the pattern was implemented. In this way, it is possible to integrate a Bragg peak from the salt, while subtracting the contribution from the background, i.e. electrolyte, and thereby visualise the two independently.

Chapter 5

First Synchrotron Beamtime

My Contributions

The experiments were planned and performed in collaboration with my colleagues Sahil Garg, Carlos Giron and the team from ESRF ID31, Jakub Drnec and Marta Mirolo and their exchange student Roosa Ilvonen from Aalto University, Finland. I was leading most of the operando X-ray data analysis, and developed the proposed mechanism in collaboration with Sahil Garg and my supervisors.

This page intentionally left blank.

5.1 Chapter Introduction

We had an aim of understanding what goes on inside the GDE when it was running, both regarding the electrolyte content in the GDE, but also to see, if any degradation or changes in the catalyst layer itself was observable. We therefore moved the setup and GC to ESRF ID31. The experiments are all performed with dry CO_2.

5.2 In Situ Study of Cu_2O Reduction

In two of the operando experiments the beam was focused on the Cu layer before the current was applied. While keeping the position, a series of fast WAXS measurements were performed with approximately 3 scans pr. second. After a minute or so, the potentiostat was started and the current was stepped up every 10 s at 10, 25, 50, 100, 150 and 200 $\mathrm{mA\ cm^{-2}}$. This allowed us to follow the phase changed due to the initial reduction of Cu_2O to Cu caused by the applied cathodic potential.

The as sputtered GDE contains only Cu, but over time surface oxidation creates a mixture of both Cu and Cu_2O. Based on the slightly dark, but still Cu-ish colour of the GDE when it was used, it was expected that the main phase would still be Cu. This was confirmed by the diffraction pattern of the pristine catalyst layer, which did show a mixture of both Cu_2O and Cu, and a rough estimation of the intensity of the two phases indicates that the main phase is Cu, but with a significant Cu_2O content.

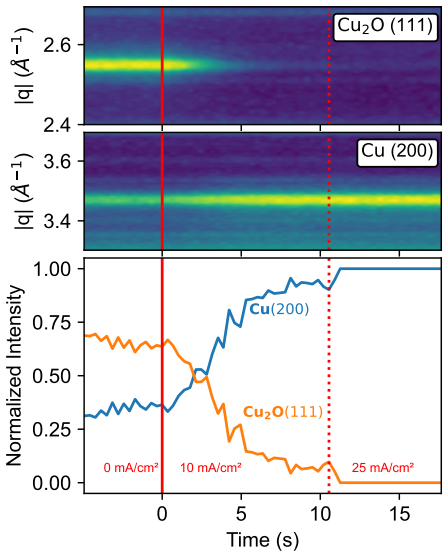

Figure 5.1: *Plot of the initial Cu_2O reduction to Cu.*

Figure 5.1 shows the two main peaks of Cu_2O (fig. 5.1a) and Cu (fig. 5.1b) and their normalised in-

tensity (fig. 5.1c) vs. time. The vertical red lines shows the time where a current was applied and further stepped to $10\,\mathrm{mA\,cm^{-2}}$. Already within these $10\,\mathrm{s}$, the Cu_2O is fully reduced to Cu, as seen by the disappearance of the Cu_2O peak and a similar increase of the Cu peak. No sign of a Cu_2O phase was observed later on. The same trend was observed in the other experiment, but here an even faster transition was observed. In all experiments we saw a complete transition within the first one or two scans, and in no cases did we see any significant signs of lattice stretching or a highly defect lattice. This indicates that the Cu lattice is completely free of oxygen. WAXS is though mainly probing the bulk of the crustal structure, and others has used more surface sensitive techniques and computational methods, finding signs of subsurface oxygen and an amorphous oxygen rich surface layer[40,41]. These methods are though only quasi-insitu, and given the very fast reduction and that no later change in the catalyst structure was observed in our experiments, we do not see any evidence that loss of subsurface oxygen should cause a performance degradation in MEA based CO_2E. It also seems unlikely that subsurface oxygen should be enhancing let alone necessary for the CO_2R process. A clear conclusion can though not be made, as undetectable changes on the catalyst surface might occur.

5.3 Operando WAXS Experiments

A series of operando experiments with $0.1\,\mathrm{M}$ $KHCO_3$ electrolyte were performed at current densities from 100 to $250\,\mathrm{mA\,cm^{-2}}$, the X-ray data was then analysed using the pyXop script (see section 4.3).

In all experiments an increasing electrolyte content in the cathode GDE could be observed, but at varying degree and location in the GDE. In most of the experiments oscillations in the electrolyte content was also observed, and seemed to correlate with a decrease in potential.

An example from an experiment performed at $200\,\mathrm{mA\,cm^{-2}}$ can be seen in fig. 5.2. The cell potential slowly increases until approximately $90\,\mathrm{min}$ where it start to decrease slightly and then oscillates up and down in $20\,\mathrm{min}$ intervals as seen in fig. 5.2a. A similar trend can be seen for the electrolyte content in fig. 5.2b. Within the first 10 to $20\,\mathrm{min}$, all parts of the GDE start to get wetted as electrolyte penetrates further towards the cathode flowfield (towards the top of the plot). Hereafter, the electrolyte content increases mainly in the outer layers of the GDE from around 50 to

100 µm, until around 100 min where it suddenly decreases slightly after the potential reaches its first local minimum. It then increases slightly and seems to peak every time the cell potential reaches a minimum.

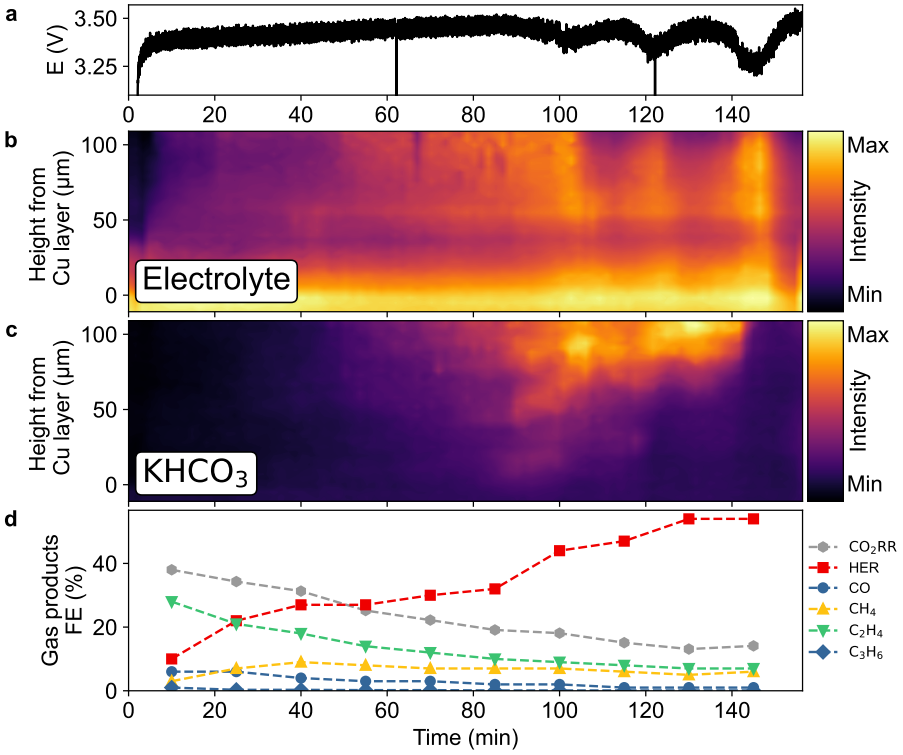

Figure 5.2: *Experiment performed at* 200 $\mathrm{mA\,cm^{-2}}$. *The contour plot in b is the integration of* 2.450 *to* 2.460 $\mathrm{Å^{-1}}$ *indicating the electrolyte content. The contour plot in c shows* $KHCO_3$ *integrated from* 2.190 *to* 2.200 $\mathrm{Å^{-1}}$ *and subtracted the background integrated from* 2.450 *to* 2.460 $\mathrm{Å^{-1}}$.

When looking at the FE of gas products in fig. 5.2d, it can be seen how the CO_2RR products slowly decreases while HER takes over. Though the low time resolution of the GC makes it a quite unclear, the rate at which the FE for H_2 increases seem to be somewhat correlated to the oscillations in potential and electrolyte content.

The increase in H_2 FE is expected to be caused by salt precipitations in the GDE blocking CO_2 accessibility to the catalyst layer. As seen in

fig. 5.2c, accumulations of crystalline $KHCO_3$ starts to form slowly after $60\,\mathrm{min}$ and are placed mainly in the outer layers of the GDE. Although it is not a very clear trend in this experiment, the salt precipitation seem to peak when the electrolyte content is low, especially seen around $130\,\mathrm{min}$. Another example can be seen in fig. 5.3 where the current density was $150\,\mathrm{mA\,cm^{-2}}$.

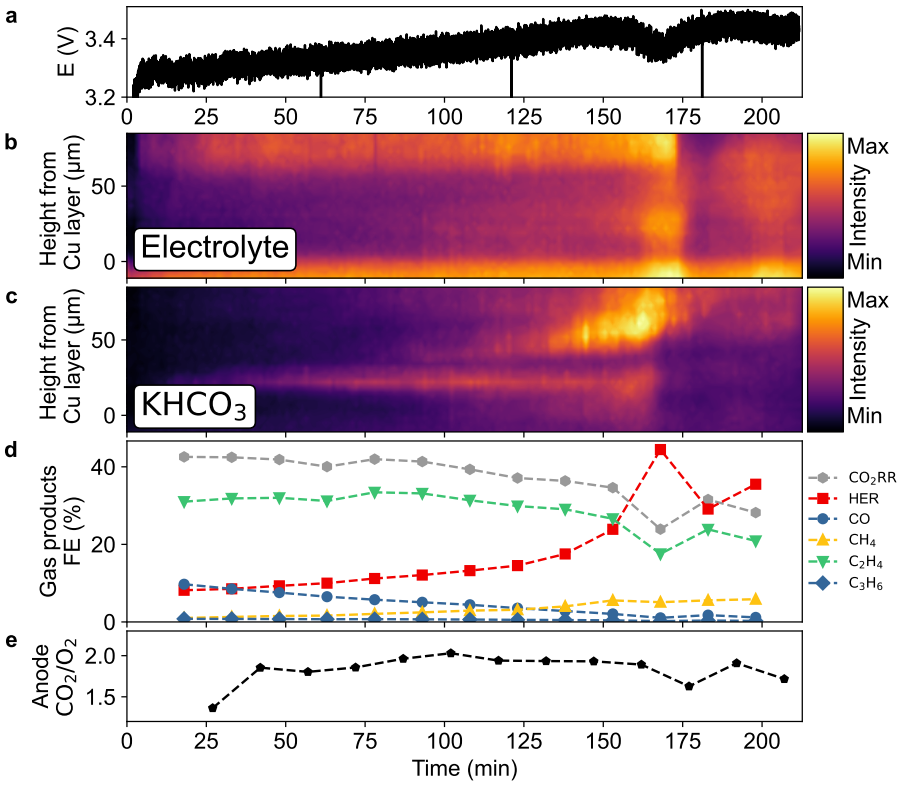

Figure 5.3: *Experiment performed at* $150\,\mathrm{mA\,cm^{-2}}$. *The contour plot in b is the integration of* 2.450 *to* $2.460\ \mathrm{Å}^{-1}$ *indicating the electrolyte content. The contour plot in c shows* $KHCO_3$ *integrated from* 2.193 *to* $2.217\ \mathrm{Å}^{-1}$ *and subtracted the background integrated from* 2.150 *to* $2.171\ \mathrm{Å}^{-1}$.

Again, a gradual increase of electrolyte can be seen in the GDE, mainly in the part more than $50\,\mu\mathrm{m}$ away from the Cu layer. A similar increase can be observed in the potential and in the H_2 FE. Around $125\,\mathrm{min}$ $KHCO_3$

precipitates starts to increase and along with the H_2 FE. At 155 to $165\,\mathrm{min}$ the signal from $KHCO_3$ peaks and the potential starts to decrease. This is quickly followed by a temporary increase in electrolyte content and a return of the cell potential. At the same time, a significant spike occurs in the H_2 FE while the C_2H_4 production decreases similarly. When looking at the CO_2 to O_2 ratio on the anode outlet, a temporary decrease can be seen slightly after the H_2 peak, indicating that the ion transport across the membrane has shifted towards OH^- instead of carbonates. This is a clear sign that CO_2 is mass transport limited at the catalyst interface since the reaction between OH^- and CO_2 is purely chemical. In all datasets any change in CO_2 to O_2 is slightly delayed, this is most noticeable in the beginning of an experiment. The delay is expected to be caused by the significantly higher solubility of CO_2 compared to O_2, and since the anode outlet gas is mixed with the electrolyte, this causes both a delay as well as a blurring of the outlet composition.

When lowering the current density to $100\,\mathrm{mA\,cm^{-2}}$, the picture became even more clear. As seen in fig. 5.4, formations of salt precipitates are followed by a flooding event dissolving the salt. These event are then followed by a fast decrease in electrolyte content, allowing new formations of precipitates. At every occurrence, the cell potential starts to decrease approximately when the salt formations peak and starts to rise again when the salt is dissolved around halfway in the flooding event. While visualisations like this can be deceiving, the formation and dissolving of crystalline $KHCO_3$ as well as background fluctuations, i.e. electrolyte flooding, were confirmed by inspecting the individual patterns using the pyXop script.

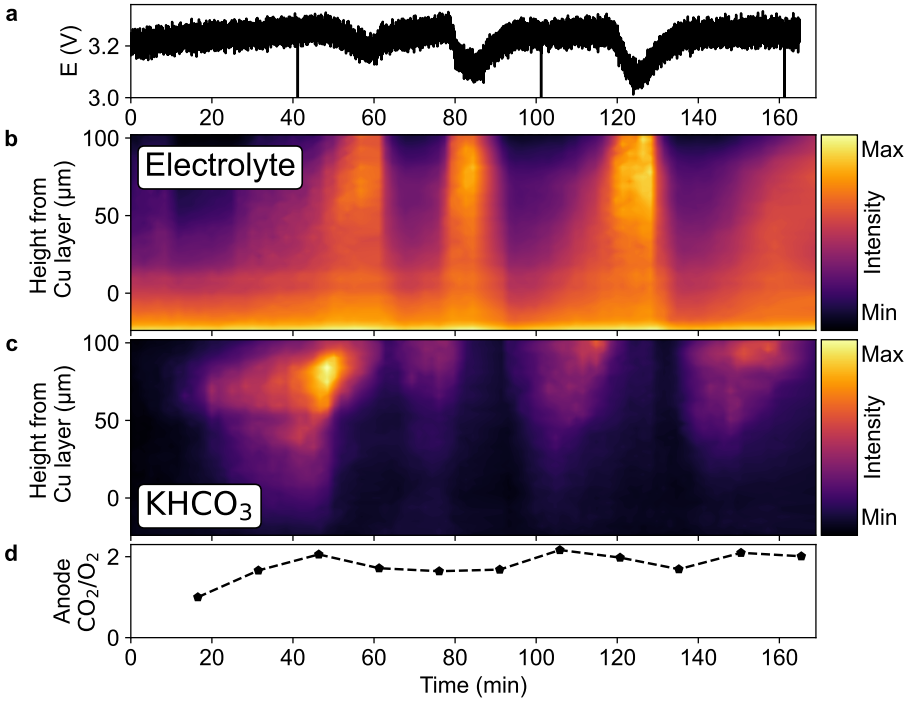

Figure 5.4: *Experiment performed at* $100\,\mathrm{mA\,cm^{-2}}$. *The contour plot in b is the integration of* 2.450 *to* $2.460\,\mathrm{Å}^{-1}$ *indicating the electrolyte content. The contour plot in c shows* $KHCO_3$ *integrated from* 2.190 *to* $2.200\,\mathrm{Å}^{-1}$ *and subtracted the background integrated from* 2.450 *to* $2.460\,\mathrm{Å}^{-1}$.

Unfortunately, due to an error, there is no GC data from the cathode side in this experiment, but data from the anode side was obtained. When taking the before mentioned delay into account, the CO_2 to O_2 ratio in fig. 5.4d, seem to decrease when salt formations are detected.

Based on this experiment, as well as the other, we can explain this cyclic behaviour by combining WAXS, potentiostat, and GC data, from both cathode and anode. An illustration of the cyclic mechanism can be seen in fig. 5.5, and is explained in the following.

5.3.1 Mechanism of Cyclic Behaviour

Precipitation of $KHCO_3$ in the GDE causes a blockage of the pores, which limits the CO_2 acceptability at the catalyst surface. This limits CO_2RR and causes an increase in HER given the galvanostatic operation. The lack of CO_2 also prevents the formation of carbonate ions, and consequently the ion transport in the membrane shifts to OH^-. Since the membrane conductivity for OH^- is higher than for carbonates, a possible explanation for the decreases in cell voltage could be the lower resistance. An other possibility is, that the CO coverage on the catalyst is reduced due to the lack of CO_2. Since *CO lowers the activity for HER[42], the lower coverage causes a decrease in the catalytic overpotential for HER, which is observed as a lower cell potential. It is very likely, that the observed oscillations in cell voltage are caused by a combination of changes in both membrane resistance and catalytic overpotential. The experiments were conducted using a reference electrode, but since it is placed on the anode side, it is not possible to de-convolute contributions from membrane resistance and (cathode) catalytic overpotential. In both cases, the main cause is a lack of CO_2.

At the same time, a flooding of the GDE occurs only to be succeeded by a decrease in electrolyte content. The cause of this flooding, and subsequent drying, is not fully understood, but one of two possible mechanisms, or a combination, could be the explanation. One possibility is, that the water flux from the anode to the cathode increases when the ion transport in membrane changes to OH^-. The total water flux across the membrane depends on both diffusion from the anode to the cathode, electro-osmotic drag caused by hydrated ions crossing, as well as hydraulic permeation[43]. All of these parameters can be affected by the change of ion, both because a membrane in OH^- form is more hydrated[44] and because the hydration, and therefore electro-osmotic drag, depends on the ion[43]. An other possibility is, that the formation of salt crystal drags water from the cathode side of the hydrated membrane towards the dry CO_2 gas stream where it is evaporated easier. This could cause a decease in the water content close to the membrane, and then either an increase in water diffusion or lead to a deficiency explaining the following drop in water content.

If the shift towards OH^- was the sole explanation for the increased water flux, it could be expected that COE would be completely impossible, but this is not the case (see section 6.4). On the other hand, in all experiments an increased intensity in the background, i.e. electrolyte, can be observed near the membrane when the flooding occurs, indicating that the water flux is increased, excluding that the water drag from salt is the only reason.

Independent of the underlying mechanism, the flooding dissolves the precipitates and thereby removes the blockage. The regained CO_2 accessibility entails an increase in CO_2RR and restores the formation of carbonate ions. This is followed by a decrease in water flux to the cathode, causing the GDE to dry. $KHCO_3$ can now again (re-)precipitate and the cycle starts over.

Figure 5.5: *Illustration of the suggested mechanism causing the oscillations.*

In most of the experiments, the salt precipitation and electrolyte content seemed to be located more than $50\,\mu m$ into the GDE. It is expected that this is a consequence of the structure of the GDL. The GDL consists of a macro-porous layer in the back and a micro-porous layer facing towards the Cu layer, and it is expected that the micro-porous layer is more hydrophobic.

The manufacturer does not provide information about the thickness of the layers, and it is not known how well defined the layers are.
In none of the experiments did we observe any sign of a K_2CO_3 phase.

5.4 Chapter Conclusion

From the in situ study performed in the beginning of two of the experiments, it was clear that at least the main part of any surface Cu_2O was reduced very fast (less than a minute), and no later signs of any oxide phase were observed. Since amorphous phases cannot be detected using WAXS, the presence of any thin surface oxide or subsurface oxygen cannot be out-ruled, but I would find it unlikely given the very reducing conditions.

The operando experiments clearly shows a gradually increasing electrolyte content in the GDE, but also significant fluctuations. The fluctuations were correlating with a change in both potential and selectivity, all following salt precipitations. And it is proposed that the fluctuations are initiated by salt blocking the GDE, and thereby preventing CO_2 from accessing the catalyst layer.

Chapter 6

Second Synchrotron Beamtime

My Contributions

The planning and execution of these experiments were done together with my colleagues Sahil Garg and Qiucheng Xu, as well as the ESRF ID31 staff Marta Mirolo and Jakub Drnec.
However, the data analysis, plotting, interpretation and discussion as it is presented here was done by me alone.

6.1 Chapter Introduction

After our finding at the first beamtime, it was obvious that a series of follow up experiments would be interesting. Being able to detect the salt precipitations in the GDE, we wanted to investigate how a change in cation would affect the precipitation. Since the salt precipitation occurs as a consequence of the reaction between CO_2 and OH^-, we also wanted to investigate COE where no salt formation is expected to occur. Particularly, it was our aim to see if we could identify what mechanism then caused the degradation in this case, and if it as expected was caused by GDE flooding.
The experimental method and data analysis were identical to the first beamtime, but with larger scans covering more of the GDE as well as part of the anode side. Besides this, a new GC gave us an improved time resolution on the gas analysis data.

6.2 Variation in Cations

As mentioned in section 1.1.1.3, it is established in literature, that the presence of cations at the cathode catalyst surface enhances CO_2R, and that this enhancement depends on the cation size. It is therefore expected, that using electrolyte based on smaller cations such as Li and Na will result in a lower selectivity for CO_2RR. In the context of investigating salt precipitations, it is though interesting to test these electrolytes, since there is a significant difference in solubility of the various carbonate salts. The solubility of the relevant cat-/anion combinations in water can be seen in table 6.1. The combination with lowest solubility for each cations is marked in red, except for Cs, where the data is for $15\,^{\circ}\mathrm{C}$ and thus not completely representative.

Cation	**Solubility** ($\mathrm{mol\,L^{-1}}$)		
	OH^-	$HCO_3{}^-$	$CO_3{}^{2-}$
Li^+	5.34	N.A.	0.18
Na^+	25	1.23	2.90
K^+	21.57	3.62	8.03
Cs^+	26.35 (30 °C)	10.78 (15 °C)	8.01 (15 °C)

Table 6.1: *Table of the solubility of relevant cation and anion combinations[43]. The lowest solubility for each cat ion is marked in red, except for Cs, where the data is for* $15\,^{\circ}\mathrm{C}$ *and thus not completely representative.*

Looking at the solubility of $KHCO_3$ compared to K_2CO_3, provides an explanation for why only crystallites of $KHCO_3$ were observed. The much lower solubility causes the potassium to precipitate in the bicarbonate form, before the concentration reaches the solubility level for K_2CO_3. Although this also depends on the CO_2 availability and pH.

If the proposed mechanism presented in chapter 5 is correct, significant variations in salt precipitation would be expected when changing the electrolyte, given the difference in solubility between the cations. A series of experiments using Li, Na and Cs bicarbonate as electrolyte was therefore performed. In all cases the electrolyte concentration was $0.1\,\mathrm{mol\,dm^{-3}}$, and the current density was $200\,\mathrm{mA\,cm^{-2}}$.

6.2.1 $LiHCO_3$

As seen in fig. 6.1c, Li_2CO_3 starts to precipitate almost immediately, and on the interface between the membrane and GDE, right on top of the Cu layer. As the experiment proceeds, the thickness of the Li_2CO_3 layer grows, but does not penetrate further into the GDE. As expected, the main product is H_2, with almost no CO_2RR gas products. The first GC injection should expectedly have contained no H_2, as it is taken right before the start of the experiment. Prior to the actual experiment, a short pre-test was performed to ensure that the cell assembly was good, and that it was neither shorted or showed too high a potential. The pretest is done by stepping up the current quickly, and typically takes about 1 to $2\,\mathrm{min}$. Therefore, a small amount of reaction products can be detected prior to the start of the actual experiment. Normally, the products from the pretest is irrelevant and close to undetectable. In this case though, it actually provides a bit of information, since the ratio between H_2 and CO_2RR products seem to be significantly higher. This indicates, that it is possible to do some amount of CO_2R with Li-based electrolyte. It could indicate, that the high H_2 FE, might not only be a consequence of the lower field enhancement from Li-ions, but also caused by a rapid and intense blocking of CO_2. This is further supported when looking at the CO_2 to O_2 ratio in the anode outlet. As seen in fig. 6.1e, there is almost no CO_2 crossing the membrane (notice the scaled y-axis). Furthermore, the ratio is declining as the Li_2CO_3 layer grows, confirming the hypothesis that salt blockage causes a lack of CO_2 at the catalyst interface. It appears the salt layer penetrates into the membrane. This could be because the salt formations create a mechanical force pushing on the membrane. Alternatively, it is because the cell is slightly tilted, causing the layer to appear thicker than it actually is. Most likely it is a combination, since the Cu layer also seem to be somewhat wider than expected, confirming that the cell was slightly misaligned. Inspections of peaks shifts confirms this (see section 4.2.4).

Unlike all other experiments, there is no signs of electrolyte penetrating into the GDE, as seen in fig. 6.1b. It is unknown if this is because the dense salt layer prevents it, or whether it is perhaps due to a lower osmotic drag caused by the lack of salt precipitation further away from the membrane.

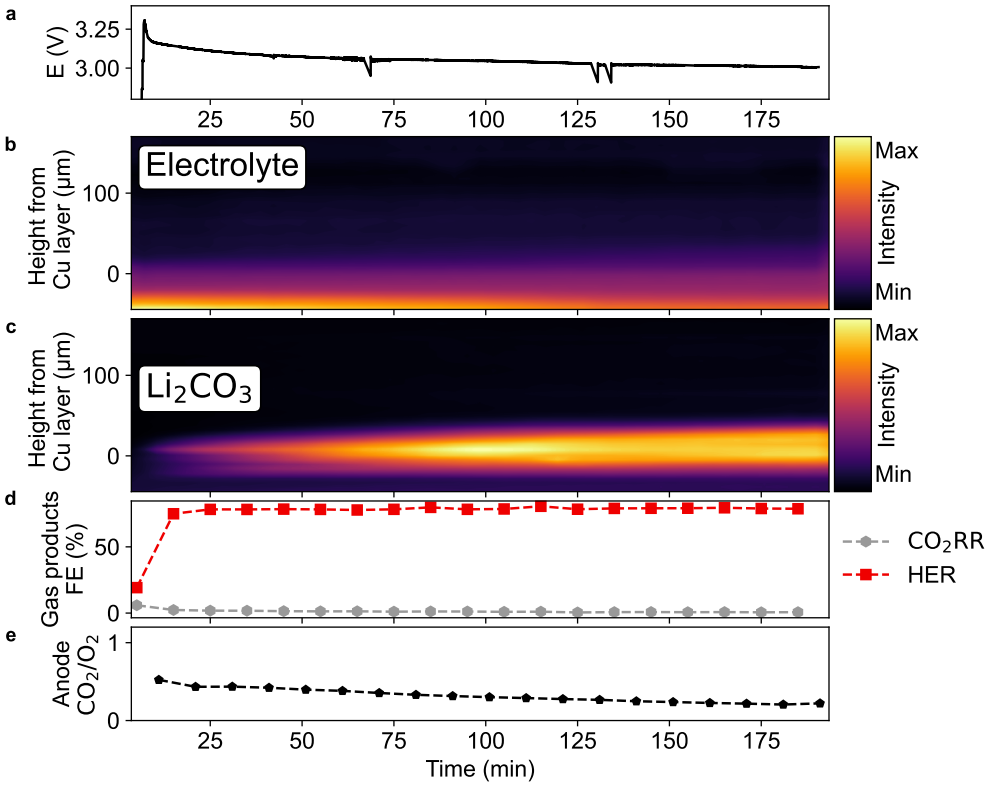

Figure 6.1: *Experiment with* $0.1\,\text{M}$ *$LiHCO_3$ electrolyte, performed at* $200\,\text{mA}\,\text{cm}^{-2}$. *The contour plot in b is the integration of* 2.439 *to* $2.464\,\text{Å}^{-1}$ *indicating the electrolyte content. The contour plot in c shows Li_2CO_3 integrated from* 2.209 *to* $2.238\,\text{Å}^{-1}$ *and subtracted the background integrated from* 2.439 *to* $2.464\,\text{Å}^{-1}$.

6.2.2 $NaHCO_3$

The experiment with $NaHCO_3$ electrolyte shows a combination of the trends observed for $LiHCO_3$ and $KHCO_3$. Relatively early, a layer of $NaHCO_3$ is formed close to the membrane, as seen in fig. 6.2c. Like in the $KHCO_3$ experiments, the electrolyte content, shown in fig. 6.2b, is slowly increasing until it suddenly penetrates deep into the GDE. Once again, an oscillating pattern can be observed, in both potential, GC data and in electrolyte/salt content.
After each flooding event, the salt precipitations move further into the GDE, as seen before. In this case, clear signs of the carbonate salt (Na_2CO_3), can be found somewhat mixed with the bicarbonate, but with increasing intensity further away from the membrane, as seen in fig. 6.2d. As one could expect, mixed phases were also observed, mainly where the two primary forms overlap.

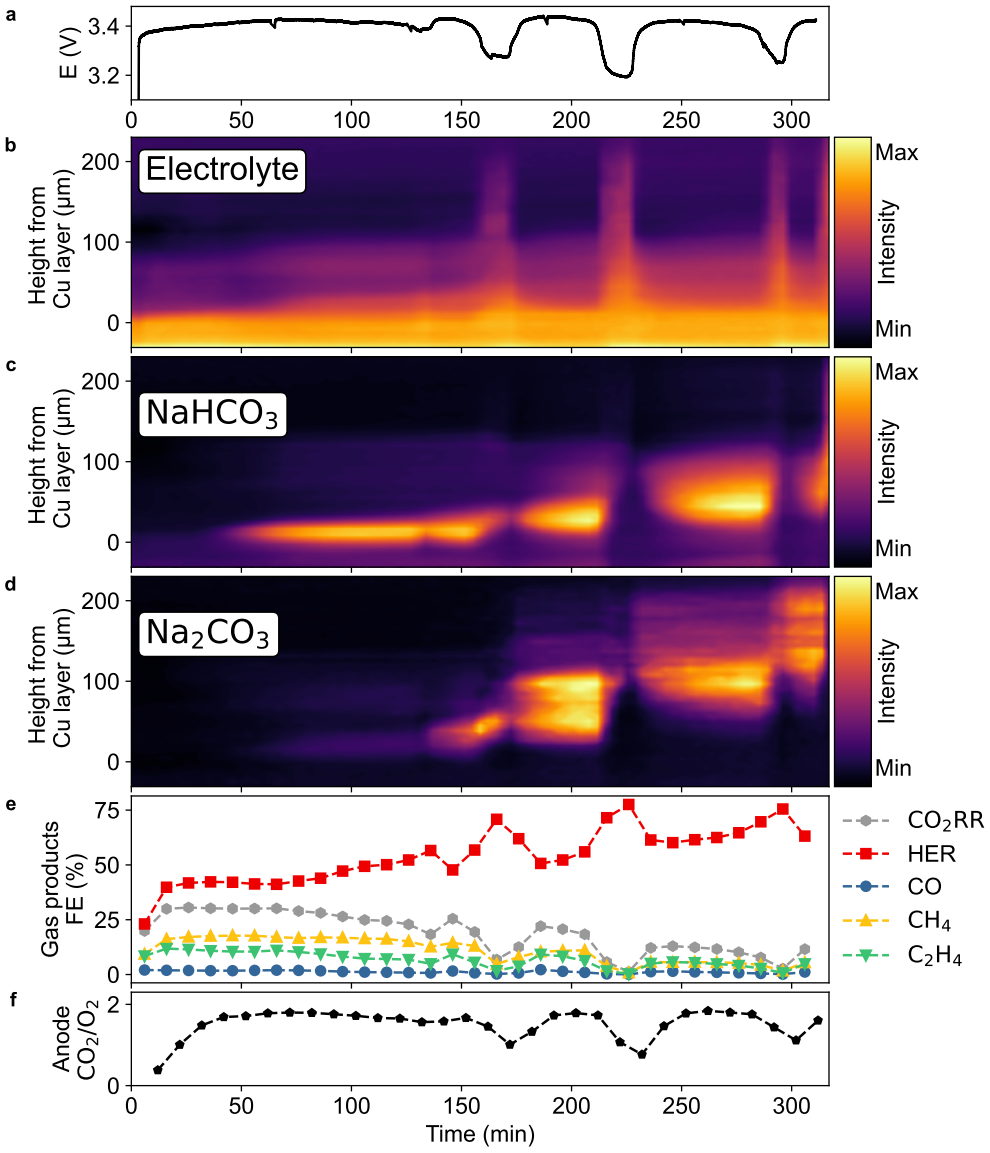

Figure 6.2: *Experiment with* $0.1\,\text{M}$ *$NaHCO_3$ electrolyte, performed at* $200\,\text{mA}\,\text{cm}^{-2}$. *The contour plot in b is the integration of* 2.668 *to* $2.684\,\text{Å}^{-1}$ *indicating the electrolyte content. The contour plot in c shows $NaHCO_3$ integrated from* 2.825 *to* $2.849\,\text{Å}^{-1}$ *and subtracted the background integrated from* 2.668 *to* $2.684\,\text{Å}^{-1}$. *The contour plot in d shows Na_2CO_3 integrated from* 2.783 *to* $2.801\,\text{Å}^{-1}$ *and subtracted the background integrated from* 2.668 *to* $2.684\,\text{Å}^{-1}$.

6.2.3 $CsHCO_3$

Using $CsHCO_3$ as electrolyte resulted in a significantly increased stability, and only very small signs of crystalline salt formations were found in the GDE. A direct investigation of the raw data (i.e. non-smoothed), using the pyXop script, reveals that small crystallites form and disappear very quickly, from around halfway in and through out the experiment. Persisting salt precipitations are though only seen in minor amounts as shown in fig. 6.3c. Though it can look like a fairly high intensity in the plot, it is somewhat deceiving since it is on a relative scale. The actual intensity of the crystallites are quite small, which is also indicated by the high background intensity in the plot.
The same goes for the plotted electrolyte content in fig. 6.3b. The constant darker area in the top corresponds to where the flowfield begins (the GDE is bulging quite a bit into the channels). The lower intensity is expected to be caused by an added attenuation of the scattered X-rays, as they go through the end of the graphite flowfield. Normally, this attenuation is insignificant, but given the low intensity of the background, it becomes quite visible.
Some changes in electrolyte content can nevertheless be observed. Initially, it seems to increase as expected, but it appears like the electrolyte content slowly decreases. It is unknown if this is due to an actual decrease in electrolyte content, or if it is some sort of measuring artefact. One possibility is, that an increased Cs^+ content in the GDE slowly attenuates the scattered signal. Unfortunately, this can not be detected by WAXS.

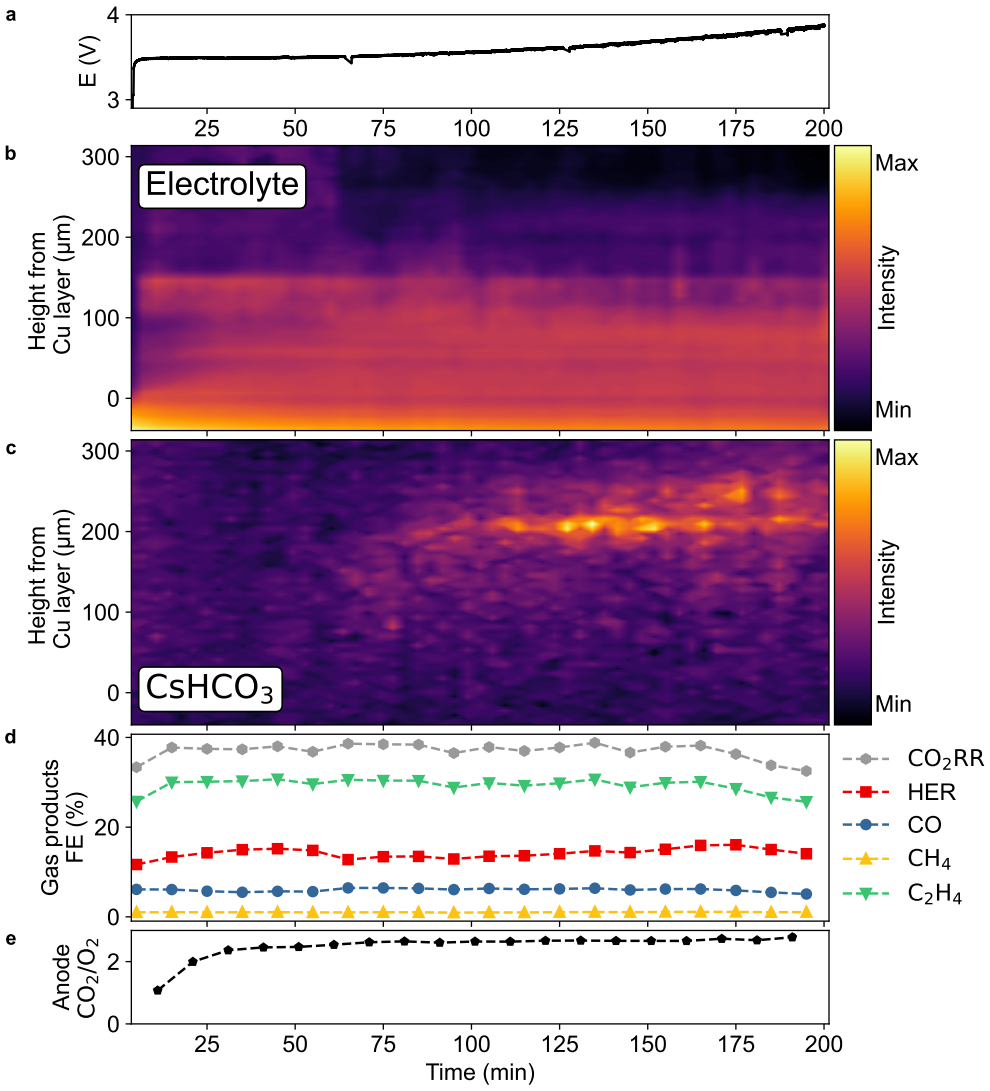

Figure 6.3: *Experiment with* $0.1\,\text{M}$ *$CsHCO_3$ electrolyte, performed at* $200\,\text{mA}\,\text{cm}^{-2}$. *The contour plot in b is the integration of* 2.085 *to* $2.095\,\text{Å}^{-1}$ *indicating the electrolyte content. The contour plot in c shows $CsHCO_3$ integrated from* 2.075 *to* $2.085\,\text{Å}^{-1}$ *and subtracted the background integrated from* 2.085 *to* $2.095\,\text{Å}^{-1}$.

6.3 Double Membrane Experiments

We also performed an experiment at $200\,\mathrm{mA\,cm^{-2}}$ with $KHCO_3$ as electrolyte, but with two membranes to mimic a membrane of double thickness. In this case, the result resembled the Li and Na experiments, with salt precipitations appearing close to the membrane at an early stage, as seen in fig. 6.4c. Two mechanisms are expected to be causing this difference. One possibility is, that the water flux to the cathode is decreased. This could cause a higher concentration of the electrolyte in the GDE, and thereby an earlier precipitation. The other possibility is, that the flux of cations to the cathode is higher, leading to a higher concentration. The total flux of cations through the membrane must be (at least in a simple approximation) equal to the flux of K^+ migrating across the membrane due to electro-osmotic drag induced by the electric field, minus the flux of K^+ diffusing back to the anode due to a concentration difference. Now, the thicker membrane is not expected to cause a significant change in the electric field inside the membrane, leaving the flux of migrating ions somewhat unchanged. The (back) diffusion on the other hand, is expected to be significantly affected by the increased distance. The (steady state) cation concentration on the cathode side is therefore expected to increase. Since water is dragged across the membrane by ions, a change in cation flux might also affect the total water flux, making the two mechanisms somewhat convoluted.

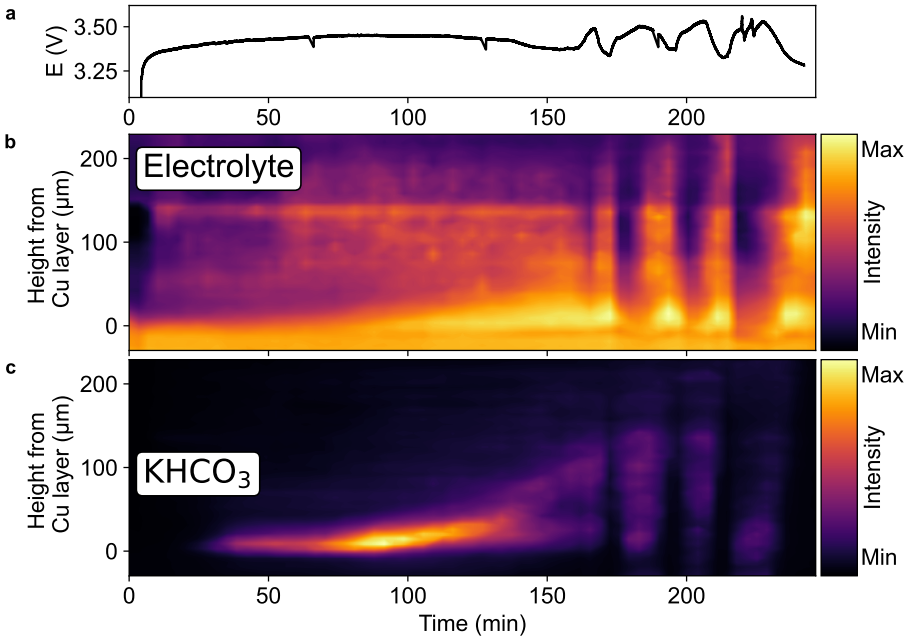

Figure 6.4: *Experiment with* $0.1\,\text{M}$ *$KHCO_3$ electrolyte and double membrane, performed at* $200\,\text{mA}\,\text{cm}^{-2}$*. The contour plot in b is the integration of* 2.450 *to* $2.460\,\text{Å}^{-1}$ *indicating the electrolyte content. The contour plot in c shows $KHCO_3$ integrated from* 2.193 *to* $2.217\,\text{Å}^{-1}$ *and subtracted the background integrated from* 2.150 *to* $2.171\,\text{Å}^{-1}$*.*

6.4 COE Experiments

A series of COE experiments was performed to ensure the observed oscillations actually are caused by salt precipitations. At the same time, we were interested in observing how a potential flooding of the GDE would look like, and if it was possible to minimise this in any way.
All the COE experiments shown here were performed at $200\,\mathrm{mA\,cm^{-2}}$ using $0.1\,\mathrm{mol\,dm^{-3}}$ CsOH as electrolyte. For safety reasons the gas flow was lowered to $15\,\mathrm{mL\,min^{-1}}$ instead of $30\,\mathrm{mL\,min^{-1}}$[I].
As predicted, no oscillations were observed in any of the COE experiments, and in none of them have I been able to find any signs of crystalline salt precipitation. When looking at the electrolyte content in fig. 6.5b, here plotted from 10 to $250\,\mu\mathrm{m}$ above the Cu layer, it shows a gradual penetration into the GDE during the first $50\,\mathrm{min}$. Hereafter, the distribution of electrolyte stays fairly constant, with a small increase in intensity. This is somewhat different than the trend for CO_2E electrolysis, where large fluctuations in both intensity and distribution of the electrolyte was observed. It therefore supports the hypothesis, that salt precipitation and changes in anion transport affects the water flux, causing variations in GDE electrolyte content.

[I]Well, I do not really think it would have been unsafe to use $30\,\mathrm{mL\,min^{-1}}$, but we were unsure if the safety inspectors at the synchrotron would agree.

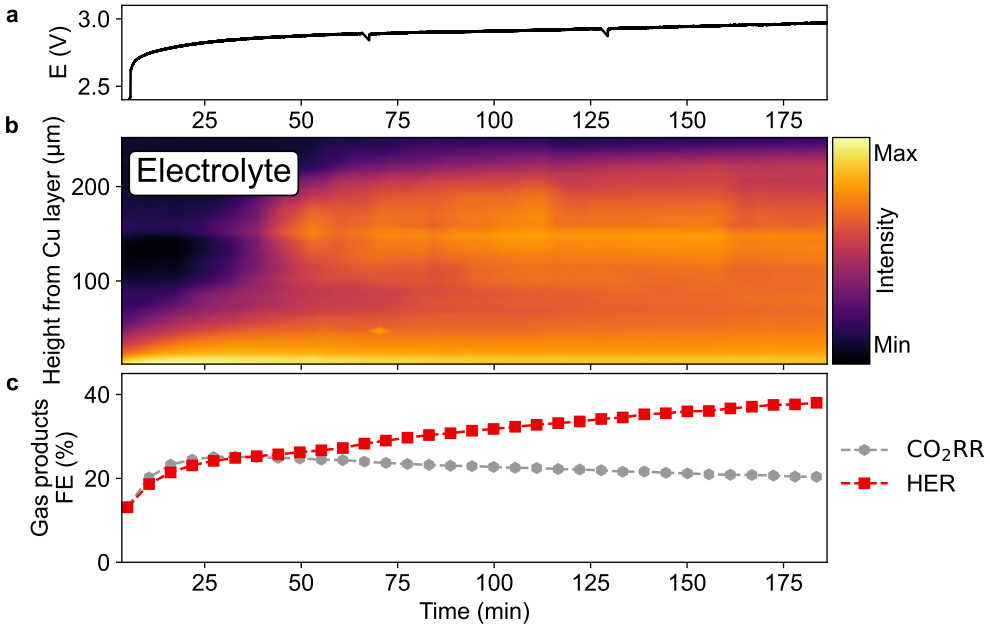

Figure 6.5: *COE experiment with* $0.1\,\text{M}$ *CsOH electrolyte, performed at* $200\,\text{mA}\,\text{cm}^{-2}$*. The contour plot in b is the integration of* 2.470 *to* $2.500\,\text{Å}^{-1}$ *indicating the electrolyte content.*

6.4.1 Double Membrane COE

We performed a similar experiment, but with two membranes. As seen by the FE for CO Reduction Reaction (CORR) gas products in fig. 6.6c, the general performance increased slightly, and the stability given by the increase in HER improved significantly. When comparing the GDE electrolyte content, plotted in fig. 6.6b, the distribution and increase looks quite similar to what was seen for the single membrane experiment (fig. 6.5b). Unfortunately, I have not (yet) found a way to quantify the electrolyte content[II], and it is therefore not possible to directly compare the intensity of the plots between experiments, though they both show the integration in the range 2.470 to $2.500\,\text{Å}^{-1}$. It is therefore not possible to determine if one of the experiments are more or less flooded than the other. Based on the similarities in both penetration rate and distribution, it does however seem unlikely that there should be a large difference in electrolyte content. Likewise, it is not possible to determine, if the overall electrolyte content is higher than in the CO_2E experiments.

[II]And yes, I have considered normalising to the Cu signal, or the intensity of the graphite flowfield, but it is unfortunately not that straight forward.

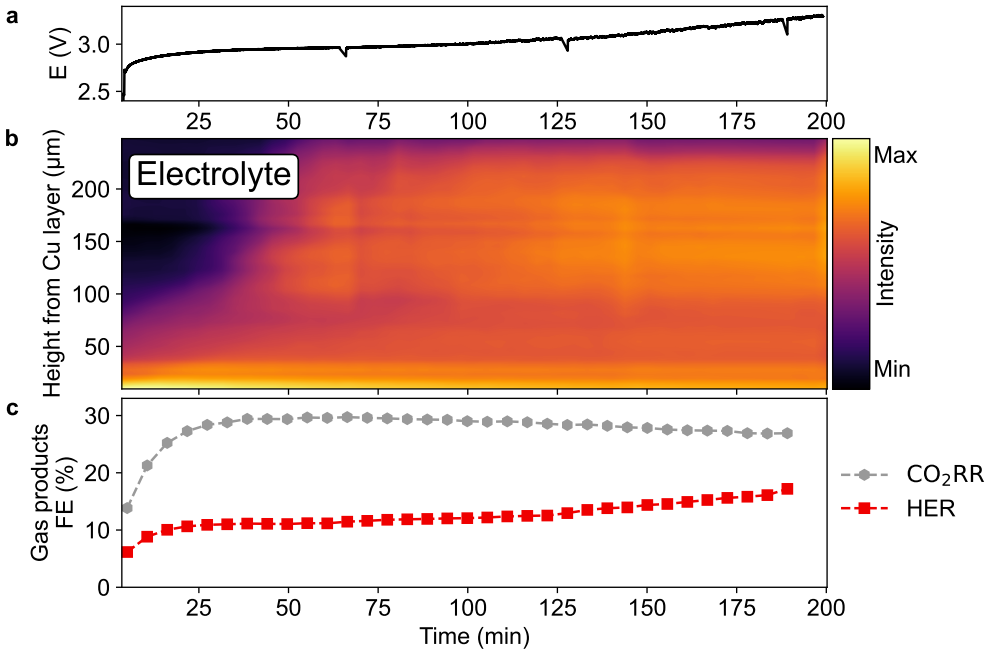

Figure 6.6: *COE experiment with* $0.1\,\text{M}$ *CsOH electrolyte and double membrane, performed at* $200\,\text{mA}\,\text{cm}^{-2}$*. The contour plot in b is the integration of* 2.470 *to* $2.500\,\text{Å}^{-1}$ *indicating the electrolyte content.*

6.4.2 Higher PTFE Containing GDE

Since it was expected that flooding was the main cause behind the increasing HER, we performed a set of similar experiments using a GDE with a higher PTFE content. The normal GDE was based on the Sigracet 39BB GDL with $5\,\%$ PTFE, whereas the GDEs used here was based on Sigracet 39 DC containing $20\,\%$ PTFE.

With respect to selectivity, both experiments performed slightly better than the low PTFE single membrane experiment, and comparable to the high PTFE double membrane. When comparing the stability, the two single membrane experiments showed a similar increase in HER, as seen in fig. 6.7c (vs. fig. 6.5c). Like before, the stability increased when using two membranes, and the experiment with a high PTFE containing GDE performed even better, with almost no increase in HER, as seen in fig. 6.8c (vs. fig. 6.6c). Regarding electrolyte content and distribution, the trend in both experiments is almost the same as previously described, but there seem to be an increase in intensity just below $150\,\mu\mathrm{m}$ above the Cu layer, as seen in figs. 6.7b and 6.8b. Interestingly, this is right below where the flowfield starts (but before any graphite peaks can be observed). It is unknown if the effect is caused by an increased compression or strain of the GDE, or it is an inherent property in the GDL. Again, it should be mentioned that the GDE bulges into the flowfield channel, explaining why the exist a significant overlap between the GDE and the graphite flowfield. The colour scale in the plot can though be somewhat deceiving, and the variation in background is actually fairly small, and not as dramatic as it might appear.

It is clear that the degradation mechanism in COE is different than the one in CO_2E, and since the increased membrane thickness improves the stability, the degradation seems to be related to "something" crossing the membrane. It could be a difference in water flux to the cathode. As discussed earlier, cation back diffusion is expected to be lower with two membranes, and this might affect the water flux. It is also possible, though not expected, that the thicker membrane it self, changes the water flux. The higher PTFE containing GDEs seemed to perform slightly better, and though the high PTFE content should increase the hydrophobicity, it seems like it also shifts the electrolyte content to a position further away from the membrane. If this is the case, and the electrolyte content is lower close to the membrane, this would probably cause a decease of electrolyte concentration at the membrane interface,

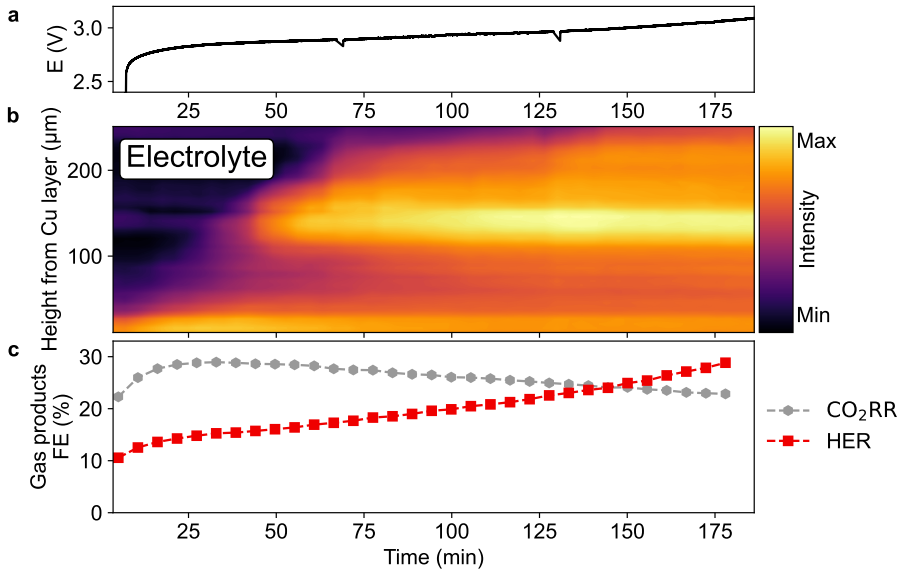

Figure 6.7: *COE experiment using the higher PTFE containing GDE and with* $0.1\,\text{M}$ *CsOH electrolyte, performed at* $200\,\text{mA}\,\text{cm}^{-2}$*. The contour plot in b is the integration of* 2.470 *to* $2.500\,\text{Å}^{-1}$ *indicating the electrolyte content.*

since more cations diffuse further out. This would further decrease the back diffusion of cations, explaining the slightly increased stability.

Another possibility is, that the degradation is caused by contaminant diffusing through the membrane, e.g. Ir dissolved at the anode. When examining the CO_2E experiments, no sign of Ir, or oxides hereof, were seen at the cathode, but in the case of COE, the significantly more alkaline anolyte could cause the $IrO_2$to dissolve and diffuse to the cathode[45–47]. A closer investigating of the X-ray pattern does show sign of what could be Ir crystals (it is assumed that it reduces at the cathode) at the cathode close to the Cu layer. A significant contributor to the degradation in COE might therefore be Ir contamination, and the thicker membrane lowers this cross over.

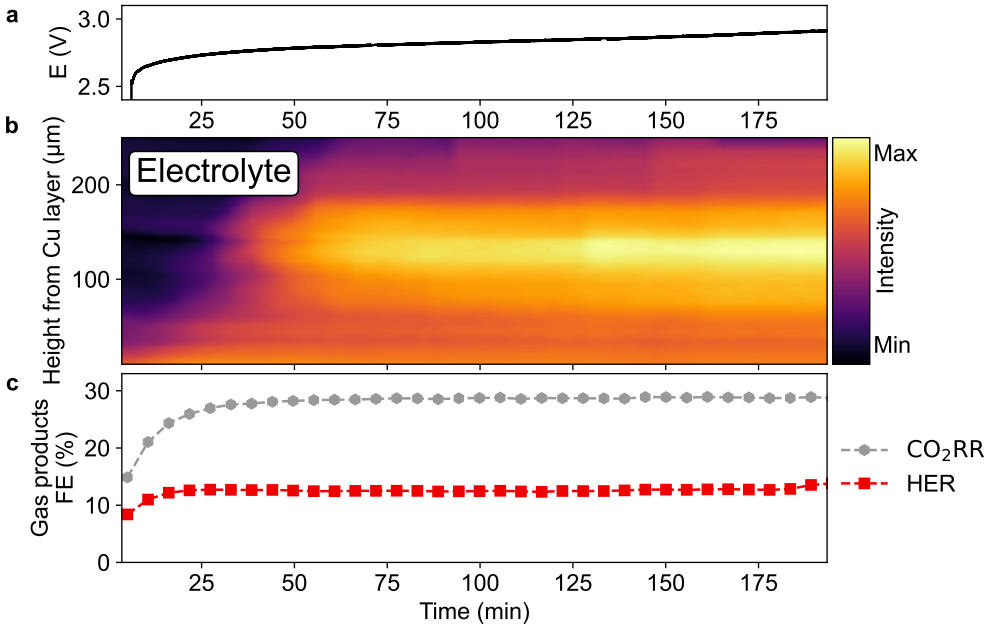

Figure 6.8: *COE experiment using the higher PTFE containing GDE and with* $0.1\,\text{M}$ *CsOH electrolyte as well as a double membrane, performed at* $200\,\text{mA}\,\text{cm}^{-2}$*. The contour plot in b is the integration of* 2.470 *to* $2.500\,\text{Å}^{-1}$ *indicating the electrolyte content.*

6.5 Stability of Cu Layer

Given the expected dissolving of IrO, it is interesting to ask if the Cu layer is also affected. From fig. 6.9b, showing the Cu content in the single membrane high PTFE COE experiment, it could look like some of Cu layer has diffused around, but that is most likely not the case. Using the interactive plot in pyXop, a closer investigation of the patterns shows a small shift of the Cu peak position between the different layers. This shift is expected to be a consequence of the parallax effect described in section 4.2.4. The magnitude of the shift indicates that the additional Cu layer is positioned at the outer edge of the cell. I therefore expect, that even though it looks like Cu is diffusing around, it is in fact very stable. Most likely the observed is an artefact cause by either a slight misalignment of the cell, or because the surface of the GDE, and thus the Cu layer, is bulging down into the flow channel, except for in the ends

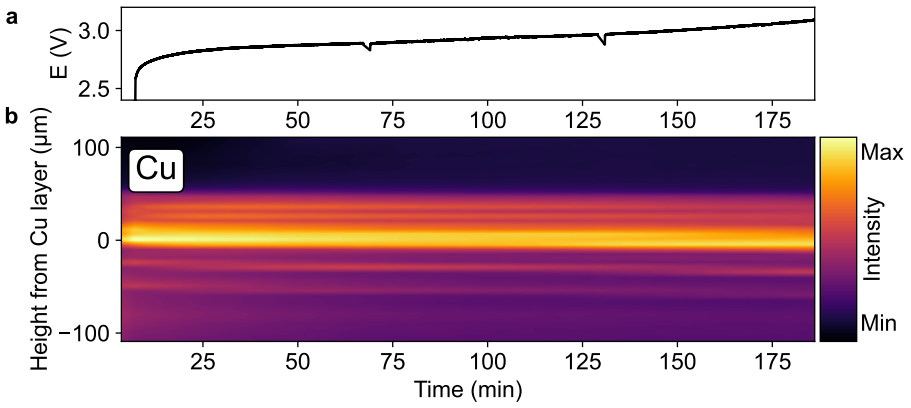

Figure 6.9: *The same COE experiment as in fig. 6.7 using the higher PTFE containing GDE and with* $0.1\,\text{M}$ *CsOH electrolyte, performed at* $200\,\text{mA}\,\text{cm}^{-2}$*. The contour plot in b shows the Cu signal integrated from* 2.982 *to* $3.022\,\text{Å}^{-1}$ *and subtracted the background integrated from* 2.937 *to* $2.951\,\text{Å}^{-1}$*.*

where the channel ends. It would also be strange, that any displacement of Cu occurs already before the experiment is initiated, and that it does not move further around during the experiment.

6.6 Chapter Conclusion

It was observed that variations in cations affected the precipitation, depending on their respective solubility, as expected. An increased membrane thickness accelerates the precipitation of $KHCO_3$, presumably due to a lower back diffusion of cations.

A series of COE experiments showed no signs of oscillations or salt precipitation, as predicted. Here an increased membrane thickness improved the stability, most likely due to a decreased Ir contamination from the anode.

This page intentionally left blank.

Chapter 7

Cation Movement in the GDE

This page intentionally left blank.

7.1 Chapter Introduction

After the first beamtime, where it was observed that salt precipitations seemed to move further towards the flowfield during the flooding events, I got curious about the mechanism causing this.
It seemed clear that the experiments with PTFE containing carbon based GDEs seemed to be less durable, and had more salt precipitate in the flowfield, than both the Ag-membranes GDEs and those reports in literature succeeding in using all PTFE based GDEs. There are of course many differences between the tree types of GDEs, but one main difference is the large difference in conductivity. This lead me to the hypothesis, that maybe an internal electric field in the GDE was driving the cations towards the flowfield.

Any charged particle, such as an ion, will experience a force when placed in an electric field. If the particle is mobile, this force will quickly accelerate it resulting in a constant drift velocity (v_d):

$$v_d = \mu E \tag{7.1}$$

where E is the magnitude of electric field in $\mathrm{V\,m^{-1}}$ and μ is the ion mobility for the specific ion under the given conditions, and is measured in $\mathrm{m^2\,V^{-1}\,s^{-1}}$. This mechanism is what drags the cations across the membrane from the anode to the cathode in the first place, but if the GDE is flooded, making the ions mobile, they would experience a similar force in the presence of an electric field.

The electrical conductance of the Ag-membrane GDEs is assumed to be almost perfect, where as the PTFE GDEs is perfectly insulating, and therefore requires a direct electrical contact to the Cu layer. The carbon based GDEs is somewhere in between, having a "non perfect" conductance. Yet they are still so conductive that the electrical contact between the flowfield and the Cu layer goues through the GDE. An ohmic loss in the GDE would cause a (small) electric field between the Cu layer and the flowfield, explaining the observed drag of the ions.

7.2 Internal E-field in the GDE

The first step was to get a rough idea about the magnitude of electric field and the drift velocity of cations in the GDE. While the manufacturer provides the sheet resistance of the GDE, i.e. the resistance along the plane of the GDE, what is relevant here is the resistance perpendicular to the GDE, i.e. from the front to the back.

It is, of course, fairly easy to measure the resistance through the raw GDE, but since it is highly compressed in the cell, this might affect the resistance. In order to measure the resistance of the compressed GDE, a piece of Cu tape was mounted on each side of a GDL of same size ($2.89\,\mathrm{cm}^2$) and type as the ones normally used, but without a Cu catalyst layer. The two pieces of tape were insulated from each other by a gasket identical to the ones normally used. A picture of the GDE taped to the gasket can be seen in fig. 7.1a. The GDE was then placed on top of an anode GDE and the normal (anode) gasket. No membrane was used, but it was expected that the two gaskets would be sufficient to ensure a compression resembling normal operation.

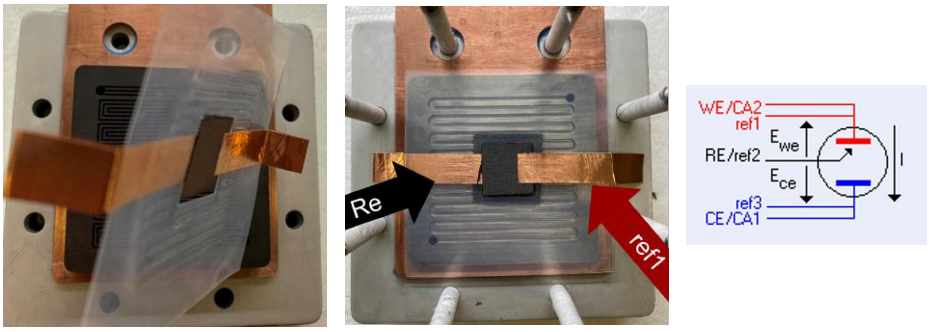

(a) *Placement of Cu tape* **(b)** *Potentiostat connections.* **(c)** *Potentiostat configuration.*

Figure 7.1: *Assembly used to measure the resistance in the GDL. a shows the placement of the Cu tape on each side of the GDL. b indicates the location of potentiostat connections. c is a screen shot of the potentiostat configuration.*

A 5-wire potentiostat was used as a current source and as high precision voltmeter, taking advantage of the 5-wire configuration (fig. 7.1c), where the voltage measurement can be separated from the wires supplying the current. The current carrying working electrode (WE) and counter electrode (CE) was connected to the cell current collectors as normal, and the reference electrode (RE) was attached to the Cu tape facing the anode. The WE reference electrode (ref1) was attached directly to the Cu tape facing the cathode flowfield, to ensure that the potential measured was only caused by the resistance in the GDE, and not including any potential contact issues between the GDE and the flowfield/current collector.
The cell was assembled using a torque of $3\,\mathrm{N\,m}$ and a current was passed in steps at 50, 100, 200 up to $500\,\mathrm{mA\,cm^{-2}}$. As expected, the response was linear and a voltage drop of $\approx 15\,\mathrm{mV}$ was measured at $200\,\mathrm{mA\,cm^{-2}}$. The cell was then tightened further using $6\,\mathrm{N\,m}$ and the test was repeated, but showed no change. The cell was disassembled, and the thickness of the GDL was measured to be $260\,\mu\mathrm{m}$. Thus, the magnitude of electric field is approximately:

$$E = \frac{15\,\mathrm{mV}}{260\,\mu\mathrm{m}} \approx 58\,\mathrm{V\,m^{-1}} \tag{7.2}$$

The ion mobility for K^+ at infinite dilution in H_2O at $25\,^\circ\mathrm{C}$ is around $7 \times 10^{-8}\,\mathrm{m^2\,V^{-1}\,s^{-1}}$[148], giving a magnitude of drift velocity of:

$$v_d = 7 \times 10^{-8}\,\mathrm{m^2\,V^{-1}\,s^{-1}} \cdot 58\,\mathrm{V\,m^{-1}} \approx 4\,\mu\mathrm{m\,s^{-1}} \tag{7.3}$$

The conditions inside the GDE is far from ultra dilute, and the ion pathway is no near straight, but this gives a rough idea of the drift velocity, if it had been in unhindered dilute conditions. Since this indicates that the internal field could cause a drag towards the flowfield, it seemed worth investigating further.

7.3 Cu Felt as GDE

The first approach was to mimic the Ag-membrane GDE and use a full Cu based GDE. I was not able to find a Cu version of the Ag-membrane, or something similar. Instead our collaborators at IRD supplied me with a Cu felt worth testing. The expectations were though fairly low, as the pore size between the woven copper wires seemed to be quite large and the total thickness was around $1\,\mathrm{mm}$.

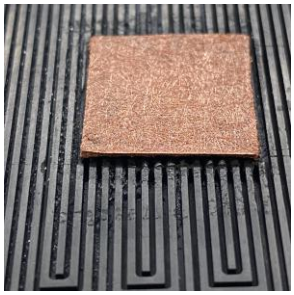

(a) *Right after disassembly.*

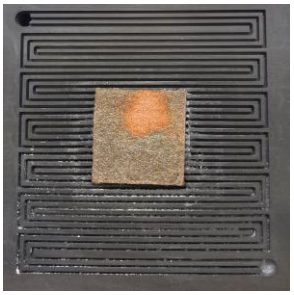

(b) *After drying in air.*

(c) *The blocked outlet.*

Figure 7.2: *Pictures after the Cu felt experiment. a is taken right after the cell was disassembled. Pictures in b and c were taken about an hour later, when the salt was dry. The amount of salt and the oxidation of the Cu indicates that the cathode had been significantly flooded with electrolyte.*

The cell was assembled as normal, except that a thicker rubber gasket was used on the cathode side, since the normal gaskets were to thin. The experiment was run at $200\,\mathrm{mA\,cm^{-2}}$, and kept running for $16\,\mathrm{h}$ until it failed due to a blockage of the flowfield, seen by a large increase in inlet pressure. Until the breakdown, the cell potential was quite stable, but mainly H_2 was produced, and only minor amounts of CO and less C_2H_4 was detected. After the experiment, the flowfield was completely full of salt to a degree I had not seen before.

The high HER selectivity was expected to be caused by an increased flooding, due to the large pore size and low hydrophobicity. An alternative explanation could though be, that the CO_2 diffusion pathway was too long given the large thickness. An attempt of cutting the felt in half was therefore made, but this showed no improvement in selectivity, and only seemed to make the flooding worse.
As the purity of the Cu felt was unknown, but expected to be relatively low, contaminations could also be the explanation for the high HER selectivity. Two attempts of cleaning the Cu felt in nitric acid was therefore done. One for $30\,\mathrm{min}$ and one where it was left over night. In both cases, the C_2H_4 selectivity increased slightly, but not above $12\,\%$.

7.4 Short-circuiting the GDL

Inspired by the method used for the PTFE GDEs, I decided to try and short circuit the GDL by making a direct contact to the Cu layer, hoping that it would prevent, or minimise, salt precipitation. At least, I hoped in this way it would be possible to alter the direction of the electric field and thereby drag the salt precipitations towards the Cu tape.
A slightly longer GDE was taped to the flowfield with Cu tape, as seen in fig. 7.3a. The gasket on top ensured that the Cu tape was not in contact with the membrane, and the active area corresponded to the normal $2.89\,\mathrm{cm}^2$.

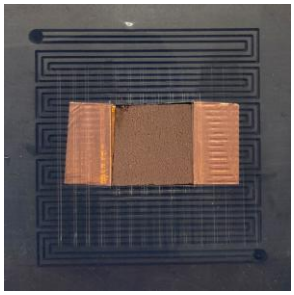

(a) *Cathode GDE with Cu tape.*

(b) *Salt in the flowfield.*

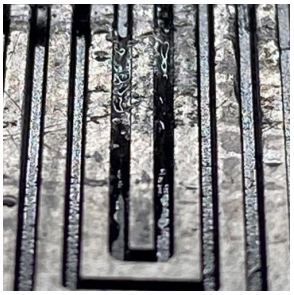

(c) *Close up of salt in the flowfield.*

Figure 7.3: *Pictures before (a) and after (b and c) the experiment using Cu tapeto short circuit the GDL. Clear signs of salt precipitation seen at the placement of the Cu tape.*

An experiment was performed at $200\,\mathrm{mA\,cm}^{-2}$ for around $16.5\,\mathrm{h}$. Unfortunately it stopped in the middle of the night due to a potential overload, and was therefore not disassembled before several hours later. When disassembled, large amounts of salt precipitations were found in the flowfield, where they were almost blocking the flow channels (fig. 7.3c). As seen in fig. 7.3b, the precipitations were concentrated at the positions where the taped had been. This gave hope to the hypothesis, since the side contact would create an electric field going from the middle of the GDE to the Cu tape, and therefore create a drag of ions towards the sides.

An alternative explanation could be, that the Cu tape it self had somehow affected the precipitation. A control experiment was therefore performed following the same procedure, but using Kapton tape instead. Unfortu-

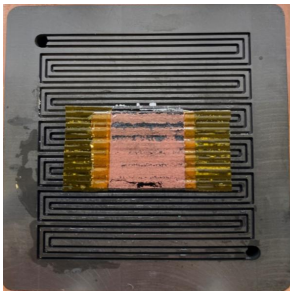

(a) *Cathode GDE after the experiment.*

(b) *Salt precipitated above the GDE.*

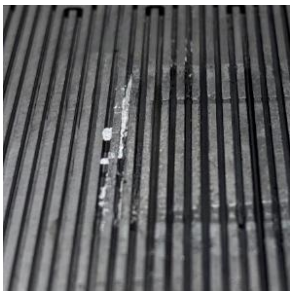

(c) *Closeup of the salt.*

Figure 7.4: *Reference test using Kapton tape on the font of the GDE. Salt were seen above the GDE.*

nately, this experiment stopped already after $1.3\,\mathrm{h}$, but some salt were present in the flowfield. As seen in figs. 7.4a and 7.4b, the salt were placed right above the GDE, and not where the tape had been. When disassembling an MEA, it sometimes happens that part of Cu sticks to the membrane. Though it is not certain, it could be expected that a higher compression makes this more likely, and since part of the Cu is missing where the salt is, it could indicate that this part of the GDE had been more compressed. This could lead to a better contact, and explain why the salt precipitated here, but it could also be a coincidence. An other possibility is, that the edge of the GDE had bulged down into the flowfield channel, creating an effect similar to the attached Cu tape in the previous experiment.

To exclude a possible interference of the flow channels, two experiments were performed with the GDE turned $45°$. In one of the experiments, Cu tape was attached on both sides of the GDE, whereas in the other Cu tape was used on one side, and Kapton tape on the other. This half front contact should, maybe, induce a driving force towards one side, as indicated by the red arrow in fig. 7.5a. Both experiments were again performed at $200\,\mathrm{mA\,cm^{-2}}$ and both ran for $12.5\,\mathrm{h}$ and was disassembled right after. In both cases the flowfield was full of salt, but there were no correlation between the location and where the tape had been. Pictures taken a few hours later when the salt was dry can be seen in fig. 7.5b for the half front contact experiment and in fig. 7.5c for the dual front contact experiment.

(a) *Diagonal GDE placement.*

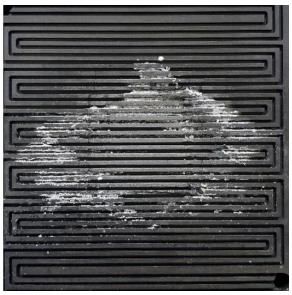

(b) *Half front contact.*

(c) *Dual front contact.*

Figure 7.5: *Pictures of the experiments performed with a diagonally placed GDE. a shows the placement of the GDE. The red arrow indicates the hypothesised cation driving force in the half contact experiment. The white paper indicates the normal GDE size. b and c are pictures of the dry salt precipitations in the cathode flowfield. b is from the experiment using both Cu tape and Kapton tape, while c is from the experiment with Cu tape on both sides.*

Interestingly enough, as seen in fig. 7.6, the cell potential in both experiments were almost identical, including a very similar oscillating behaviour. As expected, the oscillations were also seen in the product distributions. In both experiments the selectivity was fairly good and quite similar, with a FE for C_2H_4 starting just below $40\,\%$ and gradually declining throughout the experiment. The CO FE on the other hand were quite low.

It would be understandable if one wanted to reject the hypothesis based on these experiments, but there is one thing that has not been taken into account so far. Even though the Cu tape creates a direct contact to the Cu layer, there is still contact through the GDL. And given the small thickness and high porosity of the Cu layer, as well as the orders of magnitude longer distance across the GDE compared to its thickness, a substantial part of the current might still pass directly through the GDL. So before the hypothesis is completely rejected, it seemed relevant to try and insulate the back of the GDE from the flowfield.

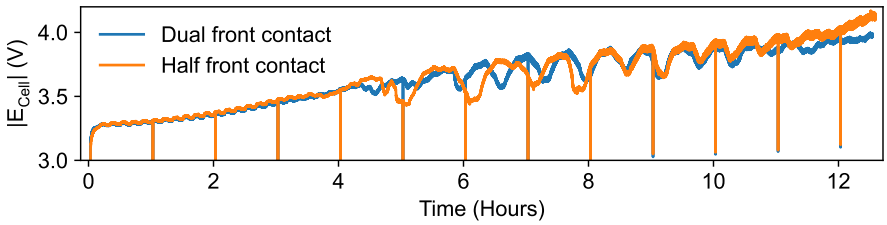

Figure 7.6: *Cell potential of the two diagonal experiments.*

7.5 All Metal Cell Test

The simplest way to insulate the GDE from the flowfield, without altering the gas diffusion pathway, seem to be to coat or lacquer the flowfield (or relevant part of it) with an insulating layer, e.g. nail polish. As I was afraid this would be difficult to remove from the graphite flowfield afterwards, I needed to use a cell with an all metal flowfield instead.

Before attempting to lacquer the flowfield, a baseline experiment was needed as reference for how much salt would precipitate in the flowfield. A normal experiment was performed, without any tape or manipulation of the flowfield, but with a slightly smaller electrode ($1.5\,\mathrm{cm} \times 1.5\,\mathrm{cm}$) due to the smaller flowfield. This experiment stopped after $4\,\mathrm{h}$, because of a potential overload. The exact cause is unknown, but the reason is probably that the cell was turned $90°$, so that the serpentine flow channels were vertical and not horizontal.

As seen in fig. 7.7a, a small amount of salt were found in the flow channels and on the back side of the GDE. Another attempt was made, but here the membrane broke and the electrolyte was pumped through the cathode flowfield, washing away any salt. Beside the membrane puncture, the anode was clearly dissolved. This have been observed many times, but seemed to be worse than normal.

One more attempt was made, but with a larger electrolyte volume ($500\,\mathrm{mL}$). In this case, the electrolyte was sucked through the anode flowfield instead of pumped in, so the GC would not be flooded in case of a membrane failure. Once again the anode dissolve, but significantly less. In this case, the membrane seemed intact, but no salt precipitation were to see in the flowfield.

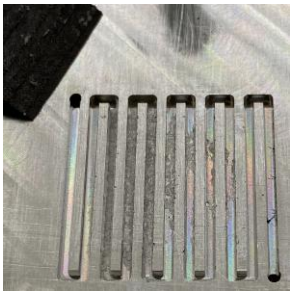

(a) *Salt in the flowfield after short experiment.*

(b) *GDE & salt after a long experiment.*

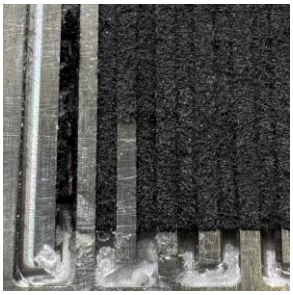

(c) *Close up of salt from long experiment.*

Figure 7.7: *Pictures after the experiments using the all metal cell. The black cloth seen in c is part of the cathode GDE stuck to the flowfield.*

In a more successful experiment, using the normal electrolyte volume ($\approx 60\,\mathrm{mL}$) and pumping direction, large amounts of salt were found in the flowfield, as seen in fig. 7.7b. Again the GDE seemed to have been under significantly higher compression, and when attempting to remove the cathode GDE, the back layer were stuck to the flowfield. The GDE also seemed to have bulged down into the channels, and because the flowfield was too small to do a test with the GDE rotated $45°$ (the anode is slightly larger, occupying most of the serpentine), combined with the problems I had faced using this cell, I decided that this cell was not suitable for the test.

7.6 Chapter Discussion & Conclusion

While waiting for the new cell, I started to doubt my hypothesis, for the following reasons. Some amount of salt precipitation were also seen in the Ag experiments, although significantly less. In the Cu-felt experiments large amount of salt were seen. I did not observe any salt precipitation in the large electrolyte volume experiment. There was no significant change when trying to short-circuit the GDL with Cu tape. At the same time reports in literature recommends the use of a humidified gas stream[35], as a possible way to avoid salt precipitations. The drag of salt into the flowfield seemed more likely to be caused by efflorescence. I expected that the differences in salt precipitation that there might be

between the different types of GDE were probably caused by differences in porosity.

Unfortunately, the delivery of the new cell took longer than hoped. When it finally arrived, I prioritised other experiments, and never performed the test with the insulated flowfield. When revising the data and pictures again, I do though regret that I did not perform the experiments with an insulated flowfield. Because even though I still feel quite certain that efflorescence is a major driving force, I am not convinced that the electric field internally in the GDE is not contributing to the drag of salt precipitation, and thereby possibly to the degradation.

Given how similar the two experiments with a diagonal GDE were, though one had half the front contact of the other, I am convinced that the main current must have passed through the GDE. In the experiments with the Cu felt, a major lack of hydrophobicity was clearly the cause of electrolyte flooding the flowfield. And in the experiment using a large electrolyte volume, I am not sure if the reversed pumping direction did not influence the result.

The result of these experiments is non-conclusive. My hypothesis that an internal E-field in the GDE causes a drag of cations towards the flowfield was not confirmed, but neither rejected.

Chapter 8

New Cell & Final Experiments

This page intentionally left blank.

8.1 Chapter Introduction

In the last part of my Ph.D. I had gained enough knowledge to realise that it would be beneficial with a new cell to investigate many of the questions I had. First of all, I wanted a cell that could be pressurised to several bars. Secondly, I was dreaming of being able to mount more than one reference electrode and in different positions, both on the anode and the cathode side. And it should preferably be completely out of Ti.

8.2 Cell Design

From the pressure test in chapter 3 it was clear that I needed a new cell of a fundamentally different design, to avoid the internal leaking between the inlets and the flowfield. Inspired by some of our other cells, I designed it as an all metal cell where pressure tight fittings could be mounted directly into the flowfield plates. The cell was manufactured in Ti (Grade 2), and holes were made for $2\,\mathrm{mm}$ banana plugs, as well as long holes going to the middle of the flowfields for temperature probes.

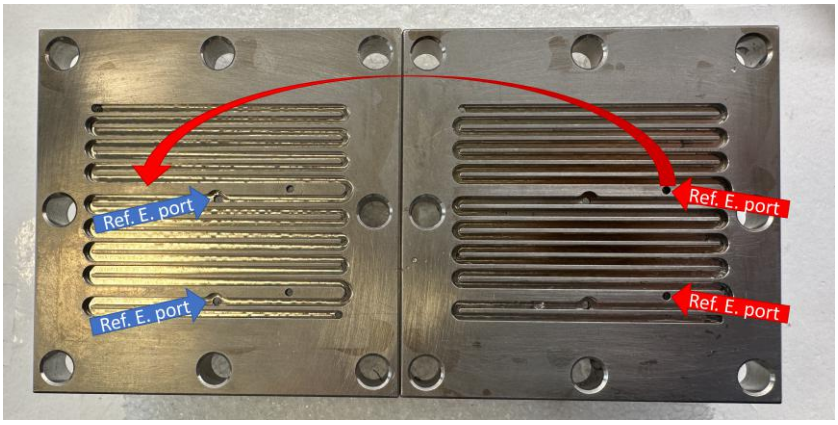

Figure 8.1: *A picture of the two flowfiled next to each other. They are made identical, but the extra reference electrode positions are intended to be used for anode (blue) or cathode (red). The red arrow indicated how the reference electrode meats the land when assembled.*

As I also wished to be able to have one or more reference electrodes in different places, each side was designed with four ports for reference electrodes. Two positioned in the channels for use on the anode side, and two positioned on the land so they could touch the membrane. The ports on the flow channel lands were positioned off center, and the lands were made slightly wider. To avoid puncturing the membrane, the cell is assembled so the reference electrode touching the membrane will face the opposite land, ensuring a good support for the membrane, as indicated by the long red arrow on fig. 8.1.

8.2.1 Pressure Testing the Cell

The first step was to pressure test the cell just using a gasket with no cut-out for the electrodes. Unfortunately, the cell was leaking quite significantly, especially through the middle holes for the bolts. Two causes were identified, and if I should redesign the cell, I would make a few changes to overcome this.

The problems were identified using a pressure measurement film (Fujifilm Prescale). The result from one of the test can be seen in fig. 8.2a. This first problem is, that the flowchannels are too close to the holes for the bolts.

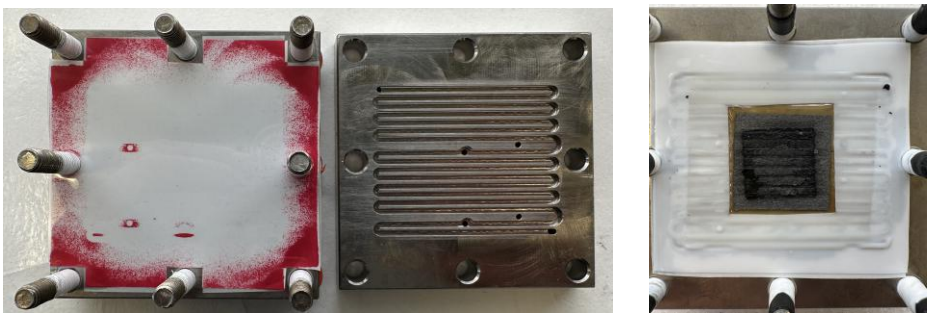

(a) *Test with pressure measurement film.* **(b)** *Decreased gasket size.*

Figure 8.2: *Pictures from the pressure test. a shows the result using a pressure measurement film, and it is clearly seen how the compression was higher at the edges. b shows how using smaller gaskets solved the problem. The picture is taken after one of the tests.*

Though I eventually did manage to solve this, there should have been more space in between. Secondly, the main compression is at the edge where the bolts are. If there had been a small indent along the outer edge of the plates, approximately where the red markings can be seen, the compression would be moved inside of the bolts. All of this was made worse by a slightly uneven surface.

The issues were solved by polishing the cell, and decreasing the area of the gaskets, so the compression became less on the edges, as seen in fig. 8.2b. The gaskets were also exchanged with a slightly thicker ($254\,\mu m$) PTFE version.

The cell was now ready for electrochemical testing, at high pressure and with two reference electrodes. An annotated picture of the cell mounted with all connections can be seen in fig. 8.3. The red arrows shows the components on the cathode side, and the blue the anode side.

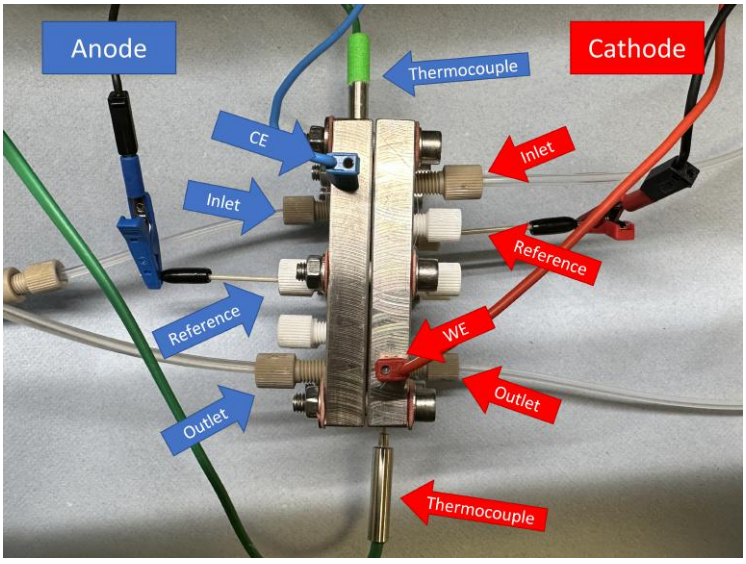

Figure 8.3: *The assembled cell with all connections. Blue indicates an anode connection, red a cathode.*

8.3 Experiments With two Reference Electrodes at High Pressure

A series of experiments were performed at $5\,\mathrm{bar}$ and with a reference electrode on both the anode and cathode side. In order to use two reference electrodes, two potentiostat channels needed to be used. One of the reference electrodes were connected to the potentiostat channel supplying the current as normal. The other channel was connected with the WE and CE wires floating, while the WE and CE reference wires (ref1 & ref3) were connected to the main channel. The second reference electrode was connected to the reference (ref2) of the slave channel.
At first I tried using the normal Sustainion membrane, but it kept braking at high pressure, I therefore changed to the more durable MPIP membrane made by our collaborators at University of Surrey. Experiments by my colleagues have though shown, that the two membranes perform somewhat identical at normal conditions.At higher temperatures, my colleague Carlos did though find, that the selectivity towards HER was significantly lower when using the MPIP membrane compared to the Sustainion.

8.3.1 $65\,^{\circ}\mathrm{C}$ $5\,\mathrm{bar}$

The first experiment were initiated at $60\,^{\circ}\mathrm{C}$, but the temperature increased slightly to $67\,^{\circ}\mathrm{C}$ throughout the experiment, due to an error in the PID controller script. The average temperature was around $65\,^{\circ}\mathrm{C}$.

At first the current was set to $200\,\mathrm{mA\,cm^{-2}}$, but as seen in fig. 8.4c almost no C_2H_4 was produced. At the same time, the potential was relatively low, expectedly due to the lower resistance in the membrane at higher temperature. I therefore increased the current to $300\,\mathrm{mA\,cm^{-2}}$ in an attempt of reaching a similar cell potential. While this increased the FE for C_2H_4 significantly (to around $10\,\%$), the main product was still CO ($53\,\%$).

After around $8.5\,\mathrm{h}$, the cell potential started increasing rapidly, but until then only small amounts of H_2 was detected with a partial current density around $15\,\mathrm{mA\,cm^{-2}}$. Unfortunately, the higher humidity of the outlet gas caused the Flame Ionisation Detector (FID) in the GC to go out from time to time. Therefore, some of the GC data points are missing.
The plots in figs. 8.4a and 8.4b contains both the full cell potential as measured by the two channels, as well as the potential measured against

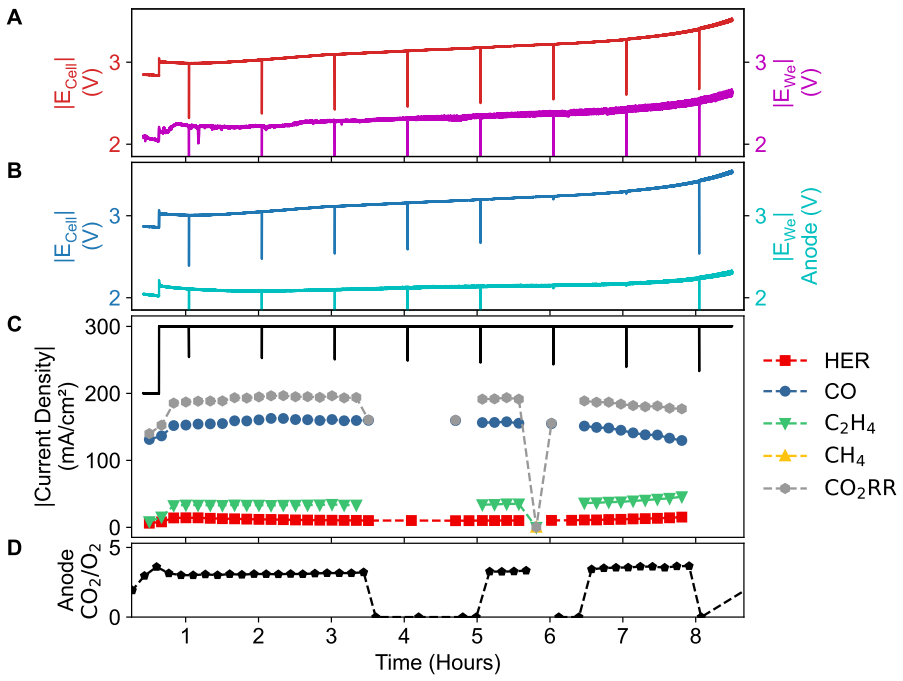

Figure 8.4: *Experiment performed at* 65 °C *and* 5 bar.

each of the reference electrodes. This shows that it is possible to use two reference electrodes at the same time, but they were not calibrated against each other, and it is not established if the placement of the cathode reference on the membrane is representative of the actual cathode potential. Further analysis has therefore not been done.

8.3.2 50 °C 5 bar

Another experiment was performed at 50 °C and 5 bar, this time the cell potential started around 3 V at 200 mA cm^{-2}, and the current was therefore not increased. Again, the H_2 production starts lower than what is normally observed, and the selectivity is highest towards CO. The FE for C_2H_4 is around 20 % and thus slightly higher than in the previous experiment. Towards the end, HER increases while CO decreases correspondingly, but C_2H_4 seems fairly stable. Again, no liquid products has been analysed, and the remaining current is expected to go to the production of these.
As seen in fig. 5.4a the reference potential was quite noisy in the beginning. This occurs as I was fiddling around with the cell trying to tighten it a bit more, since the outlet flow on the anode side was lower than expected. Therefore, the heating box was also opened and the temperature went down, and I assume that the dip in CO current is an effect of this. I later found, that the leak on the anode side was not from the cell itself, but a leak from the cap on the electrolyte reservoir.

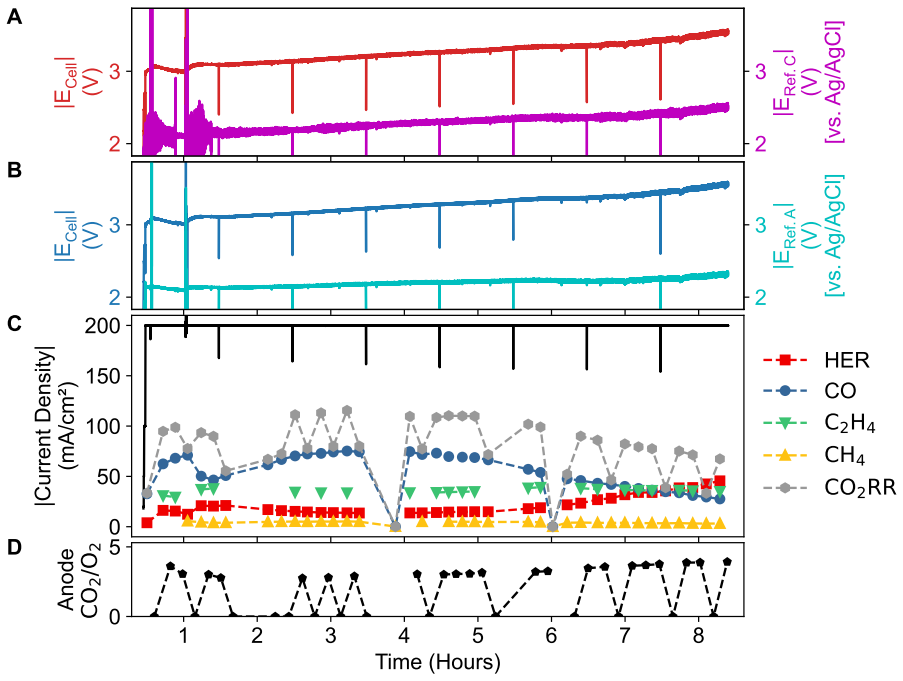

Figure 8.5: *Experiment performed at* 50 °C *and* 5 bar.

8.3.3 Unheated 5 bar

As a reference, I performed an unheated experiment at 5 bar. The experiment ran significantly shorter, as the cathode flow path got blocked causing the inlet pressure to increase to 6 bar (supply pressure) after 4.5 h. The pressure difference caused the membrane to brake.
Unfortunately, the problems with the GC had become worse (even though the humidity was now normal). There is therefore no data for C_2H_4 at the beginning, but the first data points show an increase in partial current compared to the previous experiments. At the same time, the CO current is significantly decreased. The HER also seem to be quite low. I suspect this is due to an error in the GC integration (the same error does not occur for the other compounds[I]), but I cannot exclude it is an actual effect of the high pressure, causing a significant increase in e.g. formate production.

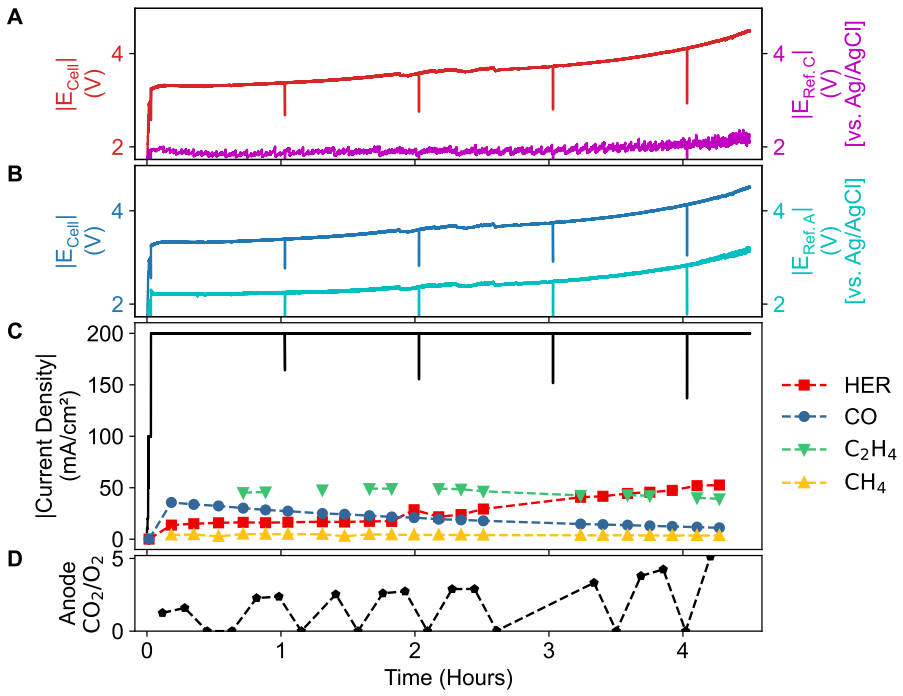

Figure 8.6: *Experiment performed at* 5 bar*, but unheated.*

[I]The error occurs, as the response for H_2 is so large that the TCD signal starts oscillating. The integration algorithm therefore only integrates parts of the H_2 peak.

8.4 Chapter Discussion & Conclusion

In chapter 3, the heated experiments showed an increased selectivity towards HER, and of the CO_2RR (gas) products only CO was seen. While a small overpressure of $500\,\mathrm{mbar}$ helped some, the experiment was only performed at relatively low current density, and the partial current density of CO and C_2H_4 did not seem to increase a lot when the current was raped up to $150\,\mathrm{mA\,cm^{-2}}$. Since these experiments were some of the earlier ones, and the membrane is different, I am not sure how comparable they are to the pressurised experiments presented here. It does though seem like the higher pressure causes a decrease in HER, although it could also be an effect of the membrane (or, less likely, the cell).
When increasing the overpressure to $5\,\mathrm{bar}$, the selectivity towards C_2H_4 does not increase as hoped, not even at room temperature. And when thinking further about it, it might not be so strange. Even though the CO_2 pressure is increased, the partial pressure of CO at the catalyst surface might not be. Actually the opposite would be expected, since the CO is produced at the surface, and if there is no change in FE it would be at the same rate. The lower HER would of course change this, but at the same time, when the temperature is increased, the diffusion of CO is expected to increase, leading to a possible explanation for why the CO production goes up at higher temperature.
An increased diffusion of CO near the surface would lead to a lower surface coverage, as it is easier transported away. Therefore, the production of CO increases, while the C−C coupling, and thus the selectivity for C_2H_4, decreases at higher temperature, and an increased pressure does not affect this. So even if the accessibility of CO_2 is increased at higher pressures, and HER is decreased as a consequence, the higher temperature would cause a shift towards CO production.

No salt, nor oscillations, were observed in the heated experiments. While more experiments are needed to make a definite conclusion, I expect this can be explained by two factors. First of all, the solubility of $KHCO_3$ increases with temperature, explaining the lack of precipitation. Secondly, the (back) diffusion of cations is expected to increase with temperature, thereby lowering the steady state concentration at the cathode-membrane interface.

Chapter 9

The Anode

This page intentionally left blank.

9.1 Chapter Introduction

The main focus of my work has been on the cathode. However, considering the title of the thesis, I think a brief comment on my observations, as well as a general consideration, regarding the anode is in order.

9.2 Standard Anode not Viable for Industrial Use

In all of the work presented, the anode has been a carbon based GDE with an Ir based catalyst. While this works for research purposes, it is not viable for a large scale industrial use. First of all, the worlds annual production of Ir is very low, and will most likely be insufficient for a wide industrial use[49]. Secondly, the use of a carbon based substrate is not ideal on the anode, since it is easily oxidised.

9.2.1 Dissolving of the Anode

In may of the experiments, it was seen that the anode rapidly degraded and dissolved when the cell potential became too high ($\approx 5\,\mathrm{V}$). This caused a discolouring of the otherwise water clear electrolyte. As seen in fig. 9.1a, in the worst cases it turned completely black, and parts of the carbon paper could be seen in the electrolyte. When disassembling the cell, the anode was in these cases clearly dissolving. Figure 9.1b is an example of a slightly dissolved anode, in some cases the outer edge and the center were not even connected any more.
The problem was seen independent of the cell used, but might have been worsened by a high compression. The problem did though seem to vary throughout my Ph.d., and I expect that differences in various batches of the commercial anode is the explanation. In the beginning, the anode could be reused between experiments (though I never did), but later this was completely impossible, even if the cell assembly procedure and all other components were the same. At one point, our collaborator at IRD attempted to make an anode similar to the Dioxide Materials, but this was even less stable.
In one experiment, I tried to use a larger electrolyte volume, and though it did last longer, a degradation of the anode was still seen. In this case, I compared the pH of the used electrolyte to the fresh, as I suspected that a pH change might have been the cause of degradation. As seen in fig. 9.1c, there was no significant change. It is unclear to me why the larger electrolyte volume performed better.

(a) *Electrolyte.*

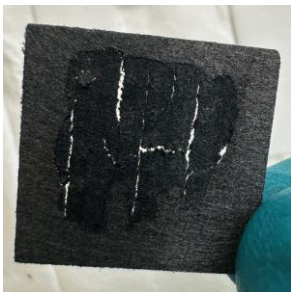

(b) *Slightly dissolved anode.*

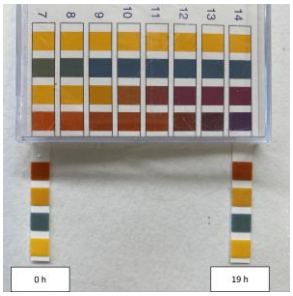

(c) *pH test of large electrolyte.*

Figure 9.1: *a is an example of a discoloured electrolyte when the anode was heavily dissolved. b is an example of a slightly dissolved anode. c shows the result of a simple pH paper test before and after an experiment with* $500\,\mathrm{mL}$ *electrolyte.*

9.3 Requirements for an Industrial Anode

For future industrial use it is necessary to find catalyst materials that are both sufficiently abundant, which Ir is not, and is stable under the given conditions. An anode catalyst suitable for CO_2E might therefore not be ideal for COE. Since contamination seem to be an issue, the catalyst material should preferably also not be highly active for HER, or at least sufficiently stable. The use of carbon based substrates should also be avoided.

Chapter 10

Final Conclusion & Outlook

There is no doubt that the main finding of my Ph.d. project is how salt precipitations in the GDE causes an oscillating behaviour in CO_2E.
A mechanism was proposed, that salt precipitations block CO_2 from getting to the catalyst layer and membrane. The lack of CO_2 causes both an increase in HER, but also a shift in anion transport through the membrane (from carbonates to OH^-). The changed ion transport decreases the potential loss in the membrane, and thereby a lower cell potential. An increase in GDE electrolyte content could be seen, following the blockage and increase in HER. While the cause of the increased electrolyte content remains unclear, it dissolves the salt blockage and causes an oscillating behaviour.

At the second beamtime, experiments with different cations confirmed the expected mechanism proposed from the first beamtime. An increase in salt precipitation was seen for salts of lower solubility as well the expected trend in HER and CO_2 cross over.
An experiment using a thicker membrane showed a worsening of the precipitation for $KHCO_3$ expected to be caused by a decrease in cation back diffusion.

A series of COE were also performed using CsOH, and as expected no salt precipitations or oscillations were observed. Using a GDE with a higher PTFE content increased the performance slightly, but the most significant enhancement of stability was seen with an increased membrane thickness. As this is opposite to what was observed for CO_2E, this suggests that the degradation mechanisms for COE is different than for CO_2E.

For COE it seems likely that Ir contamination is the main cause of degradation, whereas flooding seems to be less of a challenge. Given the significantly lower solubility of CO vs. CO_2 this does not correspond with the expectation that flooding of GDE should be the main cause for degradation in CO_2E. There is the possibility that the water flux towards the cathode is lower for CO_2E, perhaps due to the OH^- transport in the membrane, as opposite to carbonates. The observed fluctuations when doing CO_2E with $NaHCO_3$ and $KHCO_3$ however indicated the opposite, that a OH^- transport increased the water flux towards the cathode. An alternative explanation is, that the use of Cs-based electrolyte causes a lower water flux to the cathode.

In the heated experiments, neither oscillations nor salt in the flowfield were observed. It is unknown if this is due to the different membrane, the increased solubility of $KHCO_3$ or an increased back diffusion of cations at higher temperatures.
Based on all of these findings, it seems clear to me, that understanding and tailoring transport mechanisms in the membrane is essential to obtain a stable CO_2E operation. Thus, transport and diffusion of water, anion as well as cation in the membrane are obvious areas for further research.
One possibility would be to use X-ray fluorescence to monitor cation movement in the membrane as well as the GDE. This could be done in combination with WAXS experiments similar to the presented, but would likely require the use of Cs, as K might not emit X-rays with sufficiently high energy to escape the cell.

The heated experiments also seemed to show an increased selectivity towards CO. Though more experiments are needed to draw a conclusion, a possible explanation is, that an increased diffusion of CO causes a lower coverage, and therefore a lower C−C coupling. Investigating COE at elevated temperatures and increased pressure could provide further insight to this.

References

1. Moss, A. B. *et al. Versatile high energy X-ray transparent electrolysis cell for operando measurements* Oct. 2022.
2. Moss, A. B. *et al. In Operando investigations of oscillatory water and carbonate effects in MEA-based CO2 electrolysis devices* Oct. 2022.
3. International Energy Agency. *The future of petrochemicals* tech. rep. (Oct. 2018), 152.
4. Ellen MacArthur Foundation. *The New Plastics Economy: Rethinking the Future of Plastics & Catalysing Action* tech. rep. January (2017), 68.
5. Hori, Y., Kamide, N. & Suzuki, S. Energy storage by electrolytic reduction of carbon dioxide. jpn. *Journal of the Faculty of Engineering, Chiba University* **32,** 37–40 (1981).
6. Hori, Y. & Suzuki, S. CATHODIC REDUCTION OF CARBON DIOXIDE FOR ENERGY STORAGE*). *Journal of the Research Institute for Catalysis Hokkaido University* **30,** 81–88 (1982).
7. Hori, Y., Kikuchi, K. & Suzuki, S. PRODUCTION OF CO AND CH 4 IN ELECTROCHEMICAL REDUCTION OF CO 2 AT METAL ELECTRODES IN AQUEOUS HYDROGENCARBONATE SOLUTION. *Chemistry Letters* **14,** 1695–1698 (Nov. 1985).
8. Hori, Y., Kikuchi, K., Murata, A. & Suzuki, S. PRODUCTION OF METHANE AND ETHYLENE IN ELECTROCHEMICAL REDUCTION OF CARBON DIOXIDE AT COPPER ELECTRODE IN AQUEOUS HYDROGENCARBONATE SOLUTION. *Chemistry Letters* **15,** 897–898 (June 1986).
9. Pei, Y., Zhong, H. & Jin, F. A brief review of electrocatalytic reduction of CO 2 —Materials, reaction conditions, and devices. *Energy Science & Engineering* **9,** 1012–1032 (July 2021).

10. Hori, Y., Murata, A., Takahashi, R. & Suzuki, S. Enhanced formation of ethylene and alcohols at ambient temperature and pressure in electrochemical reduction of carbon dioxide at a copper electrode. *Journal of the Chemical Society, Chemical Communications,* 17–19 (1988).

11. Nitopi, S. *et al.* Progress and Perspectives of Electrochemical CO 2 Reduction on Copper in Aqueous Electrolyte. *Chemical Reviews* **119,** 7610–7672 (June 2019).

12. Hori, Y. in *Modern Aspects of Electrochemistry* 89–189 (Springer New York, New York, NY, Mar. 2008).

13. Liu, X. *et al.* Understanding trends in electrochemical carbon dioxide reduction rates. *Nature Communications* **8,** 15438 (Aug. 2017).

14. Hori, Y., Murata, A. & Takahashi, R. Formation of hydrocarbons in the electrochemical reduction of carbon dioxide at a copper electrode in aqueous solution. *Journal of the Chemical Society, Faraday Transactions 1: Physical Chemistry in Condensed Phases* **85,** 2309 (1989).

15. Hori, Y., Takahashi, R., Yoshinami, Y. & Murata, A. Electrochemical Reduction of CO at a Copper Electrode. *The Journal of Physical Chemistry B* **101,** 7075–7081 (Sept. 1997).

16. Deng, W., Zhang, P., Seger, B. & Gong, J. Unraveling the rate-limiting step of two-electron transfer electrochemical reduction of carbon dioxide. *Nature Communications* **13,** 803 (Feb. 2022).

17. Monteiro, M. C. O. *et al.* Probing the local activity of CO 2 reduction on gold gas diffusion electrodes: effect of the catalyst loading and CO 2 pressure. *Chemical Science* (2021).

18. Resasco, J. *et al.* Promoter Effects of Alkali Metal Cations on the Electrochemical Reduction of Carbon Dioxide. *Journal of the American Chemical Society* **139,** 11277–11287 (Aug. 2017).

19. García de Arquer, F. P. *et al.* CO 2 electrolysis to multicarbon products at activities greater than 1 A cm -2. *Science* **367,** 661–666 (Feb. 2020).

20. Larrazábal, G. O. *et al.* Analysis of Mass Flows and Membrane Crossover in CO 2 Reduction at High Current Densities in an MEA-Type Electrolyzer. *ACS Applied Materials & Interfaces* **11,** 41281–41288 (Nov. 2019).

21. Ma, M. *et al.* Insights into the carbon balance for CO 2 electroreduction on Cu using gas diffusion electrode reactor designs. *Energy & Environmental Science* **13,** 977–985 (2020).

22. Reyes, A. *et al.* Managing Hydration at the Cathode Enables Efficient CO 2 Electrolysis at Commercially Relevant Current Densities. *ACS Energy Letters* **5,** 1612–1618 (May 2020).

23. Yang, K., Kas, R., Smith, W. A. & Burdyny, T. Role of the Carbon-Based Gas Diffusion Layer on Flooding in a Gas Diffusion Electrode Cell for Electrochemical CO 2 Reduction. *ACS Energy Letters* **6,** 33–40 (Jan. 2021).

24. Wu, Y. *et al.* Effects of microporous layer on electrolyte flooding in gas diffusion electrodes and selectivity of CO2 electrolysis to CO. *Journal of Power Sources* **522,** 230998 (Feb. 2022).

25. Rossi, K. & Buonsanti, R. Shaping Copper Nanocatalysts to Steer Selectivity in the Electrochemical CO2 Reduction Reaction. *Accounts of Chemical Research* **55,** 629–637 (Mar. 2022).

26. Jin, M. *et al.* Shape-controlled synthesis of copper nanocrystals in an aqueous solution with glucose as a reducing agent and hexadecylamine as a capping agent. *Angewandte Chemie - International Edition* **50,** 10560–10564 (Nov. 2011).

27. Long, R., Zhou, S., Wiley, B. J. & Xiong, Y. *Oxidative etching for controlled synthesis of metal nanocrystals: Atomic addition and subtraction* June 2014.

28. Lyu, Z., Shang, Y. & Xia, Y. Shape-Controlled Synthesis of Copper Nanocrystals for Plasmonic, Biomedical, and Electrocatalytic Applications. *Accounts of Materials Research* (Sept. 2022).

29. Fichthorn, K. A. & Chen, Z. Surface science of shape-selective metal nanocrystal synthesis from first-principles: Growth of Cu nanowires and nanocubes. *Journal of Vacuum Science & Technology A* **38,** 023210 (Mar. 2020).

30. Grosse, P. *et al.* Dynamic Changes in the Structure, Chemical State and Catalytic Selectivity of Cu Nanocubes during CO 2 Electroreduction: Size and Support Effects. *Angewandte Chemie International Edition* **57,** 6192–6197 (May 2018).

31. Popović, S. *et al.* Stability and Degradation Mechanisms of Copper-Based Catalysts for Electrochemical CO 2 Reduction. *Angewandte Chemie International Edition* **59,** 14736–14746 (Aug. 2020).

32. Kuang, S. *et al.* Stable Surface-Anchored Cu Nanocubes for CO2 Electroreduction to Ethylene. *ACS Applied Nano Materials* **3,** 8328–8334 (2020).

33. Napporn, T. W. *et al.* in *Fuel Cells and Hydrogen* 175–214 (Elsevier, Jan. 2018).

34. Choi, W. *et al.* Origin of Hydrogen Incorporated into Ethylene during Electrochemical CO 2 Reduction in Membrane Electrode Assembly. *ACS Energy Letters* **7,** 939–945 (Mar. 2022).

35. Wheeler, D. G. *et al.* Quantification of water transport in a CO2 electrolyzer. *Energy and Environmental Science* **13,** 5126–5134 (2020).

36. Hoffmann, H. *et al.* Development of a Modular Operando Cell for X-ray Imaging of Strongly Absorbing Silver-Based Gas Diffusion Electrodes. *Journal of The Electrochemical Society* **169,** 044508 (Apr. 2022).

37. Kieffer, J., Valls, V., Blanc, N. & Hennig, C. New tools for calibrating diffraction setups. *Journal of Synchrotron Radiation* **27,** 558–566 (Mar. 2020).

38. Skinner, L. B. *et al.* Benchmark oxygen-oxygen pair-distribution function of ambient water from x-ray diffraction measurements with a wide Q -range. *The Journal of Chemical Physics* **138,** 074506 (Feb. 2013).

39. Amann-Winkel, K. *et al.* X-ray and Neutron Scattering of Water. *Chemical Reviews* **116,** 7570–7589 (July 2016).

40. Cavalca, F. *et al.* Nature and distribution of stable subsurface oxygen in copper electrodes during electrochemical CO2 reduction. *Journal of Physical Chemistry C* **121,** 25003–25009 (2017).

41. Liu, C. *et al.* Stability and effects of subsurface oxygen in oxide-derived Cu catalyst for CO2 reduction. *Journal of Physical Chemistry C* **121,** 25010–25017 (Nov. 2017).

42. Cave, E. R. *et al.* Trends in the Catalytic Activity of Hydrogen Evolution during CO2 Electroreduction on Transition Metals. *ACS Catalysis* **8,** 3035–3040 (Apr. 2018).

43. Garg, S., Giron Rodriguez, C. A., Rufford, T. E., Varcoe, J. R. & Seger, B. How membrane characteristics influence the performance of CO 2 and CO electrolysis. *Energy & Environmental Science* **15,** 4440–4469 (2022).

44. Luo, X., Rojas-Carbonell, S., Yan, Y. & Kusoglu, A. Structure-transport relationships of poly(aryl piperidinium) anion-exchange membranes: Eeffect of anions and hydration. *Journal of Membrane Science* **598,** 117680 (Mar. 2020).

45. Cherevko, S. *et al.* Oxygen and hydrogen evolution reactions on Ru, RuO2, Ir, and IrO2 thin film electrodes in acidic and alkaline electrolytes: A comparative study on activity and stability. *Catalysis Today* **262,** 170–180 (Mar. 2016).

46. Flores, R. A. *et al.* Active Learning Accelerated Discovery of Stable Iridium Oxide Polymorphs for the Oxygen Evolution Reaction. *Chemistry of Materials* **32,** 5854–5863 (July 2020).

47. Wang, Z., Guo, X., Montoya, J. & Nørskov, J. K. Predicting aqueous stability of solid with computed Pourbaix diagram using SCAN functional. *npj Computational Materials* **6,** 160 (Dec. 2020).

48. Koneshan, S., Rasaiah, J. C., Lynden-Bell, R. M. & Lee, S. H. Solvent structure, dynamics, and ion mobility in aqueous solutions at 25 °C. *Journal of Physical Chemistry B* **102,** 4193–4204 (May 1998).

49. Vesborg, P. C. K. & Jaramillo, T. F. Addressing the terawatt challenge: scalability in the supply of chemical elements for renewable energy. *RSC Advances* **2,** 7933 (2012).

Acronyms

AEM	Anion Exchange Membrane.	32, 33
CA	Chronoamperometry.	36
CO_2E	CO_2 Electrolysis.	I, 2, 8, 10, 25, 26, 29, 30, 32, 35, 43, 45, 50, 53, 55, 66, 86, 88, 90, 91, 120–122, 137
CO_2R	CO_2 Reduction.	3, 5–8, 34, 35, 39, 66, 77, 78
CO_2RR	CO_2 Reduction Reaction.	3, 5–8, 25, 41, 46, 67, 72, 73, 77, 78, 116

COE	CO Electrolysis.	10, 45, 55, 73, 76, 86, 87, 89–93, 120–122
CORR	CO Reduction Reaction.	88
CP	Chronopotentiometry.	36
DAC	Digital Analogue Converter.	30, 48
DFT	Density Functional Theory.	7, 14
FE	Faradaic Efficiency.	31, 32, 34, 37, 38, 42, 48, 67–69, 78, 88, 103, 112, 114, 116
FID	Flame Ionisation Detector.	112
GC	Gas Chromatograph.	31–34, 37, 40–44, 48, 49, 65, 67, 71, 76, 78, 80, 104, 112, 115, 133, 137–140

GDE	Gas Diffusion Electrode.	I, 8–10, 25, 29, 30, 32–34, 37, 39, 41, 47, 48, 53, 54, 60, 65–68, 72–74, 76, 78, 80, 82, 84, 86, 88, 90–93, 97–99, 101–106, 119, 121, 122
GDL	Gas Diffusion Layer.	8, 25, 29, 47, 74, 90, 98, 99, 101, 103, 105
HDA	$CH_3(CH_2)_{15}NH_2$.	13, 14, 17, 22, 25
HER	Hydrogen Evolution Reaction.	5–7, 34, 35, 41, 42, 67, 72, 88, 90, 100, 112, 114–116, 120, 121

HR-TEM	High Resolution Transmission Electron Microscopy.	14
I2C	Inter-integrated Circuit.	31
ICP-MS	Inductively Coupled Plasma Mass Spectrometry.	13
MEA	Membrane Electrode Assembly.	8, 9, 25, 30, 41, 53, 54, 56, 57, 59, 60, 66, 102
MFC	Mass Flow Controller.	31, 38, 39, 44
MFM	Mass Flow Meter.	42
NC	Nano Cubes.	10, 13–17, 20, 22, 24–26
NP	Nano Particles.	I, 13, 14, 16, 25
PEEK	Polyether Ether Ketone.	54
PFA	Perfluoroalkoxy Alkane.	18, 29
PID	Proportional Integral Derivative.	46, 112
PTFE	Polytetrafluoroethylene.	29, 47, 48, 55, 90–93, 97, 101, 111, 121
PWM	Pulse Width Modulation.	46
ROI	Region Of Interest.	57

SEM	Scanning Electron Microscopy.	13, 16, 20–22, 25
VFM	Volumetric Flow Meter.	32, 42
WAXS	Wide Angle X-ray Scattering.	I, 60, 65, 66, 71, 74, 82, 122
XRD	X-ray Diffraction.	13, 14
XRD-CT	X-ray Diffraction Computed Tomography.	54, 59
fcc	Face-centered Cubic.	13
pyXop	Python For X-ray Operando Analysis.	60, 61, 66, 70, 82, 92

Symbols

Q	Charge passed.	3
z	Number of Electrons.	3, 4
E°_{Cell}	Thermodynamic Cell Potential.	4
i_0	Exchange current density.	4
η_{Act}	Activation overpotential.	4, 5, 36, 37
i	Current density.	4
A	Tafel slope.	4
η_{Ω}	ohmic overpotential.	5, 37
c_x	gas concentration.	32, 43
$\dot{n}_T$	total molar flow.	32
i_x	partial current density.	32
$\dot{n}_x$	molar flow of a gas.	32, 43
Q_x	charge gone into product x.	32
z_x	number of electrons for a given compound.	32
A_{cat}	cathode area (geometric).	32
η	Overpotential.	36
E°	Thermodynamic Potential.	37
η_{Total}	Total overpotential, the sum of all overpotential in the cell..	37
α_x	GC peak area.	43
k_x	GC calibration constant.	43
$\dot{V}_x$	volumetric flow of a gas.	43
$\dot{V}_T$	total volumetric flow.	43
$\dot{V}_{\mathrm{N_2}}$	volumetric flow of N_2.	43
$\alpha_{\mathrm{N_2}}$	area of N_2 GC peak.	43

$k_{\mathrm{N_2}}$	GC calibration constant for N_2.	43
$\dot{n}_{\mathrm{N_2}}$	molar flow of N_2.	43
q	length of scattering vector, $\frac{4\pi}{\lambda}\sin(\theta)$.	59–62
v_d	Drift velocity magnitude.	97, 99
μ	Ion mobility ($\mathrm{m^2\,V^{-1}\,s^{-1}}$).	97, 99
E	Electric field magnitude.	97–99
$\vec{\boldsymbol{E}}$	Electric field.	101

Constants

F Faraday constant (approximately $9.6485 \times 10^4\,\mathrm{C\,mol^{-1}}$)
Defined as $F \equiv e \cdot N_A = 9.6485 \times 10^4\,\mathrm{C\,mol^{-1}}$. 3, 4, 32

e elementary charge
Defined as $1.602\,176\,634 \times 10^{-19}\,\mathrm{C}$. 3, 135

N_A Avogadro constant
Defined as $6.022\,140\,76 \times 10^{23}\,\mathrm{mol^{-1}}$. 3, 135

This page intentionally left blank.

Appendix A

Design of Gas Chromatograph for CO_2E

A.1 GC Configuration

There are many ways to design and configure a GC. The way presented here is what I have been using, and what I find best suited for analysing CO_2E products. In the first two years I used an Agilent 6890A GC, and later a new Agilent 8890, but they were configured identically.
The configuration including columns, carrier gas etc. was slightly updated along the way, but the fundamental principle remained the same. What is presented here is the final configuration.

A GC fundamentally works by injecting a small sample into a molecular sieve or a column containing a stationary phase. The sample is carried through the column by a carrier gas. Various compounds interact differently with the stationary phase in the column, causing a retention in the movement of the compound. For both the molecular sieve and the columns, the retention time for all products depends on the temperature, the carrier gas flow and pressure, and the type of carrier gas. When the retained compounds leave the column they are separated in time and enters a detector used to quantify each compound. The detector signal is recorded as a function of run time (after the injection) and as each compound has been separated in the column a series of peaks corresponding to each compound can be analysed. The peaks are then integrated and the area of a peak is proportional to the concentration of the respective compound in the sample.

The GC used here is equipped with two detectors, a flame ionisation detector (FID) and a thermal conductivity detector (TCD). The two detectors operate individually and each has its own injection valve, sample loop, columns etc. The only thing they share is the oven. They can therefore be regarded as two separate channels in the GC. Figure A.1 shows a sketch of the layout, and the blue line indicate the parts associated with each detector (marked in blue). The following sections describe each detector and the connected components.

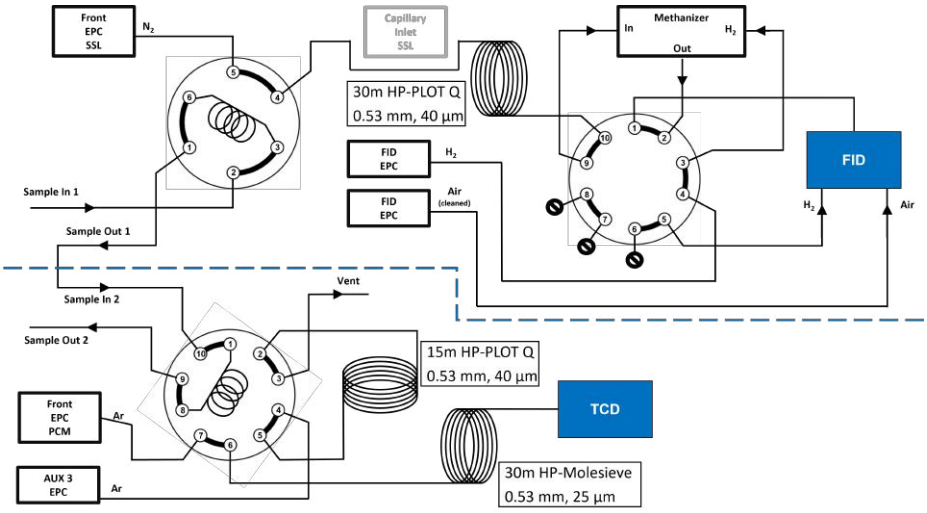

Figure A.1: *GC schematics.*

A.2 In-line Operation & Injection

When the GC is used in in-line operation, the reaction gasstream is passed through two $0.25\,\mathrm{mL}$ sample-loops, one for each channel. When the GC injects, the injection valve in each channel is turned and the column carrier gas moves the gas sample in the sample-loop into the column.

A.3 Flame Ionisation Detector

The flame ionisation detector works by burning and ionizing hydrocarbons in a hydrogen flame. The current of ions is then recorded. Since it

is only possible to detect compounds that can be combusted, permanent gasses such as O_2, N_2 and Ar cannot be detected. H_2 can also not be detected, since this is used as a fuel for the flame.
CO and CO_2 is also not directly detectable, but can be converted into methane right before the detector (and after the column) using a methanizer.

A.3.1 Column

The column used for the FID channel is a $30\,\mathrm{m}$ long HP-Plot Q capillary column with a diameter of $0.53\,\mathrm{mm}$ and a film thickness of $40\,\mu\mathrm{m}$ (the stationary phase). It does not retain permanent gasses, but separates CO, CH_4, CO_2, C_2H_4, C_2H_6, C_3H_8 and C_3H_6 in that order. A good separation of CO and CH_4 requires a temperature below $65\,^\circ\mathrm{C}$, but at this temperature the retention time of the C_3 products becomes extremely long. Therefore, the oven temperature is ramped to high temperatures after CO has passed the column.
The normal Agilent GC is equipped with a Split/Splitless inlet (SSL), but it is not used when the GC is operating in-line with the gas stream. I found, that when the gas sample is led through the SSL inlet, it causes a broadening of all peaks. This is especially a problem for the separation of CO and CH_4, as they will then overlap. I therefore recommend that the SSL inlet is (physically) bypassed if not in use.
Originally I used Ar as a carrier gas, but a better separation, and therefore faster analysis time, was obtained using N_2 instead.

A.3.2 Methanizer

The methanizer is a Ni catalyst, heated to around $375\,^\circ\mathrm{C}$, and converts CO and CO_2 into methane in a reaction with H_2. When the methanizer is used the H_2 fuel for the FID is led into the methanizer, thus providing the H_2 necessary for the reaction. The typical sample size is less than $1\,\mathrm{mL}$, and as the normal fuel supply is around 30 to $50\,\mathrm{mL\,min^{-1}}$, this H_2 supply is more than sufficient.

Since the Ni catalyst in the methanizer gets poisoned by some compounds, e.g. C_2H_4, a repeatable and stable conversion is best obtained by bypassing the methanizer before these products enter. The GC is therefore equipped with a bypass valve, leading the column flow around the methanizer and the H_2 directly to the FID.

When the valve is switched, the temporary loss of fuel supply, and a pressure transient, most often causes the flame to go out. The GC detects this by it self, and will attempt to re-ignite the flame 3 times[1]. This takes some time, and the separation between CH_4 and C_2H_4 must therefore be sufficient for the FID to reignite.

A.4 Thermal Conductivity Detector

The thermal conductivity detector measures the thermal conductivity of the column flow and compares this to a reference flow in using a wheatstone bridge. When only carrier gas and no sample compounds is in the column flow, the signal will be constant, and if the reference flow and column flow are identical (in flow and gas) the signal will be zero. When a (separated) compound is in the flow, the column gas will have a changed thermal conductivity, and the magnitude will depend on the concentration and thermal conductivity of the sample compound. Since the TCD is primarily used for the detection of H_2, Ar has been selected as carrier gas, due to the very large difference in thermal conductivity.

A.4.1 Columns

Since the HP-plot Q column cannot separate permanent gasses, a $30\,\mathrm{m}$ HP-Molesieve with $0.53\,\mathrm{mm}$ diameter and a film thickness of $25\,\mu\mathrm{m}$ is used instead. The Molesieve gets blocked by water, CO_2 and larger molecules, so these have to be filtered away. This is done by pre-separating the gasses using a $15\,\mathrm{m}$ long HP-Plot Q capillary column similar to the one used for the FID, but shorter. When injecting, the column and the Molesieve is placed after each other, but separated by the (10 port) injection valve, when permanent gasses (and CO and CH_4) have passed into the Molesieve, but before CO leaves the HP-Plot column, the valve is turned, and the flow direction in the column is changed. This causes a back-flush of the remaining gasses. The permanent gasses are then separated in the Molesieve.

[1] And irritatingly enough, not more than that. I assume it is for safety reasons, since a constant flow of un burned H_2 would otherwise be running.

A.5 Timing and Carrier Gas Flow

Since all columns share the same oven, it is a bit of a puzzle to get all timings right, while still keeping the overall analysis time down. The pre-separation in the TCD channel must be sufficient to avoid water and CO_2 from entering the Molesieve, and the time between CH_4 and C_2H_4 in the FID channel must be sufficient for the FID to re-ignite. At the same time, the temperature must be ramed up quickly to get C_3 compounds through. The temperature should also not be too high, as this will cause a long cooling time.
This is made worse when a dual injection from both cathode and anode side is used. By ramping the flows, one can get a bit more control of the two channels independent on the common temperature, but short analysis time is often associated with a more fragile operation, where e.g. increased humidity can cause problems.

This page intentionally left blank.

Appendix B

Appended Papers

B.1 Versatile high energy X-ray transparent electrolysis cell for operando measurements

Versatile high energy X-ray transparent electrolysis cell for *operando* measurements

Asger B. Moss[a], Joel Hätinen[b, c], Peter Kúš[d], Sahil Garg[a], Marta Mirolo[b], Ib Chorkendorff[a], Brian Seger[a], Jakub Drnec[b, *]

[a]*Surface Physics and Catalysis (SurfCat) Section, Department of Physics, Technical University of Denmark, 2800 Kgs. Lyngby, Denmark*

[b]*Experimental Division, European Synchrotron Radiation Facility, Grenoble, France*

[c]*Helsinki Institute of Physics, P.O. Box 64, FI-00014 University of Helsinki, Finland*

[d]*Department of Surface and Plasma Science, Faculty of Mathematics and Physics, Charles University, V Holešovičkách 2, 180 00 Prague 8, Czech Republic*

**Corresponding author: Jakub Drnec, Email: drnec@esrf.fr*

Abstract

Herein we present a design for a versatile electrochemical cell for High Energy X-ray operando studies of Membrane Electrode Assembly (MEA) based electrochemical systems. The cell flowplate materials can be interchanged according to the needs of experiments, allowing studies of different chemistries and reactions. The design also allows for coupling the X-ray elastic scattering techniques with computed tomography reconstruction, opening the possibility of 3D mapping of chemical and structural properties in operating devices. The cell has originally been designed and tested for CO_2 electrolysis performance studies using Wide Angle X-ray Scattering (WAXS) technique.

1. Introduction

In the quest for a fossil fuel-free world, electrification has become a cornerstone in the strategy, and electrolysis appears to be a promising route for energy storage and renewable feedstock of chemicals[1]. So far, most research has been in the field of water electrolysis[2], but lately, the electrolysis of more complex reactions, such as CO_2 reduction reaction (CO_2RR[1,3]), has gained interest. In both water electrolysis and especially in CO_2 (and CO) electrolysis (CO_2E) one of the most promising cell designs is the zero-gap membrane electrode assembly (MEA) due to a low operating potential and simple configuration[4–6]. From a research perspective, the MEA does come with challenges. MEAs are inherently difficult to study *in situ* and operando conditions, and even *post mortem* analysis is relatively difficult as the assembly often suffers from mechanical instability when disassembled. With X-rays it is possible to investigate the MEA (during electrolysis operation) in grazing incidence geometry where the beam is parallel to the catalyst surface, but this requires a micro-sized beam at high energy and flux. With the development of 4th Generation synchrotrons, such as the European Synchrotron Radiation Facility Extremely Brilliant Source (ESRF-EBS), it is possible to obtain a beam suitable for such grazing incidence operando measurements. Grazing incidence measurements not only give a much larger interaction volume compared to the situation where the beam is perpendicular to the catalyst layer, but they also provide the possibility to investigate different MEA depths, i.e. anode and cathode GDEs, membrane, thin catalyst layer, etc. by moving the cell in the beam through a scanning method as illustrated in Figure *1*. However, the typical MEA cell cannot be used for X-ray operando experiments in this geometry, as this sets certain requirements regarding the cell shape and materials. Even though there exists many cells for X-ray experiments[7], most of them are not suitable for investigating MEAs for water splitting and CO_2 reduction experiments. Typically they are either significantly smaller than the typical cell, very challenging to assemble, or designed for use with the beam perpendicular to the GDE[8]. Therefore, this work aimed at designing a cell that

is both easy to work with, suitable for multiple applications and that can be used for a large variety of X-ray techniques, including Wide/Small Angle X-ray Scattering (W/SAXS), diffraction and absorption tomography, X-ray dark-field microscopy and possibly even coherent scattering experiments using high energy X-ray probe. While the cell can be used in many applications, in the following we will focus on the performance towards CO_2E to discuss the cell capabilities.

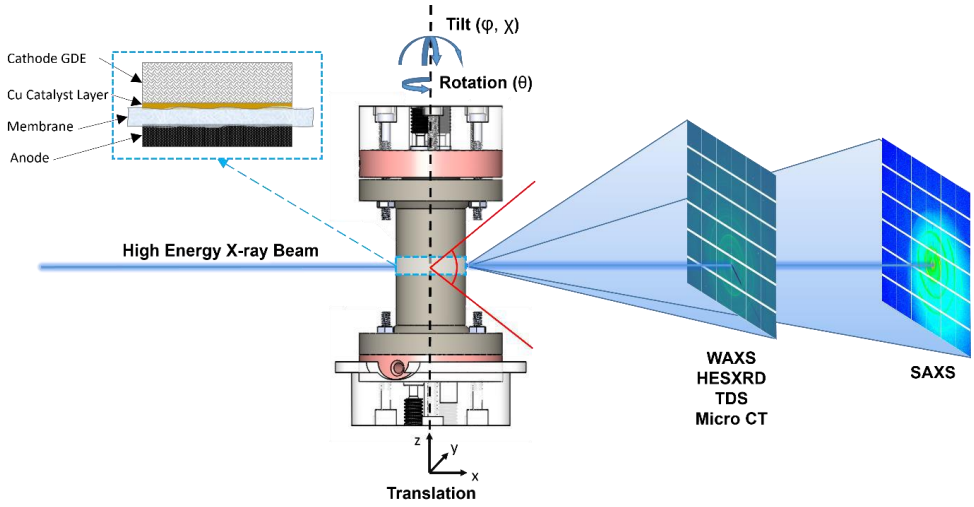

Figure 1. Illustration of the cell in the beam path. The magnification in the top left corner shows the placement and orientation of the Membrane Electrode Assembly (MEA). The cell can be moved in the beam (through translation and tilting) allowing for the different parts of the MEA to be investigated. The cell design allows X-rays scattered in wide angles (up to 30°) to exit unhindered as illustrated by the red lines. The circular design and the possibility to rotate it freely also enables the cell to be used for absorption and scattering tomography experiments.

2. Result and Discussion

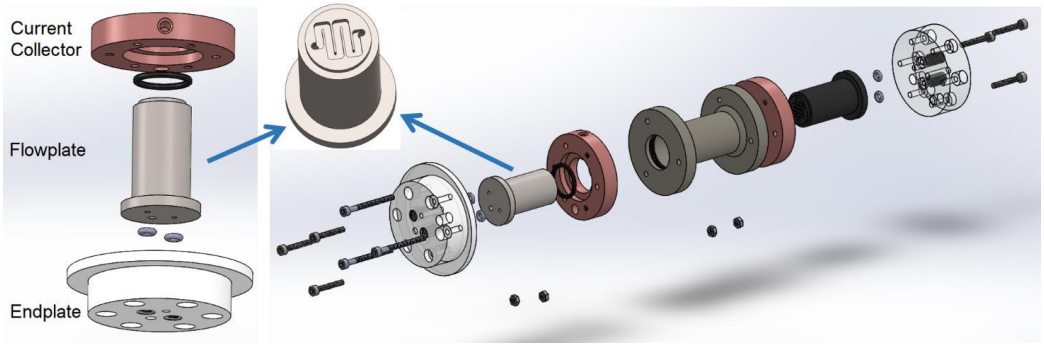

Figure 2. Left: Exploded view of the anode flowfield. Right: Exploded view of the whole cell. The insert shows the flowplate with the single-channel serpentine.

2.1. Cell design

The cell consists of three main parts; an anode flowfield, a cathode flowfield, and a polyether-ether ketone (PEEK) casing in which the two flowfields are inserted from each end (Figure *2*). Each flowfield consists of a 3D printed endplate in which the gas/liquid tubes are connected, a flowplate[†] of suitable material, e.g. graphite, Ti, or stainless steel, as well as anodic and cathodic current collectors, which also serve the purpose of fastening the flowplate to the endplate.

Unlike the typical MEA electrolyzer, the cell has a dog bone shape, with the MEA being placed in the middle. The design is chosen in order to have a wide opening without any blockage of the scattered X-rays making it possible to measure very wide angles and thereby a large portion of the reciprocal space. This is indicated by the red line in Figure 1. The circular design was chosen to enhance

[†] To avoid confusion the term flowplate is used for the raw piece, whereas the assembly of the endplate, flowplate and current collector is called flowfield.

tomography capabilities by minimizing potential reconstruction defects. Sealing between the flowfield and the membrane is ensured by a Viton O-ring which is slightly lowered into the flowfield. As the O-rings in the two flowfields are not fully submerged, a gap is created when the two flowfields are pushed together. This gap ensures that the GDEs are not compressed too much, e.g. so it loses its porosity or the cell short circuits.

The inner diameter of the O-ring is 9 mm leaving room for a disk-shaped GDE with a 63.6 mm^2 area. The diameter of the cell is small enough to allow for high-energy X-ray imaging, scattering, and tomography experiments with sufficient contrast and resolution and with minimal issues related to secondary scattering, parallax effect and absorption. At the same time, the electrode area is still of a size comparable to most experimental work in the CO_2E and water electrolysis fields thus allowing investigations that are relevant to commercial devices.

In order to obtain the dog bone shape, the flowplates are shaped as rods with a collar for fixation and a pin for alignment in one end and channels going through to the other end where a serpentine flow channel ensures gas or liquid transfer to the GDE. The flow channel geometry was chosen in this case to be a single channel serpentine with relatively wide channel dimensions. Though the geometry of the flow path is known to be important in electrolysis devices[9], a simple design was chosen both to minimize blockage from any salt deposition that may occur on the gas fed side of the device and to enhance bubble removal. This design also allows for unhindered X-ray analysis of the part of the GDE that might bulge into the serpentine. The channels are 1 mm deep, 1.25 mm wide, and 5.6 mm long and the lands are 0.25 mm. The exact geometry can be seen in the insert of Fig. 1. The flowfield assembly is designed in a way that allows easy flowplate exchange, so the flowplate can be manufactured from different materials and with different channel geometry.

The current collector is a Cu ring with a chamfer fitting the collar of the flowplate such that when assembled they form a flush surface towards the endplate. A hole in the side of the current collector can be used to connect to a potentiostat. The flowplate and current collector are firmly attached to the endplate by three screws that go through the endplate into the threads in the current collector. Two alignment pins ensure that the three parts are fixed and that the gas/liquid channels are placed correctly. Two small O-rings slightly submerged into the endplate creates a sealed connection and press the collar of the flowplate towards the current collector to ensure a good electrical connection.

Our initial design used metal quick connectors for the connection of gas and electrolyte tubes into the flowfields, but initial tests of CO_2E with a silver catalyst indicated a rapidly increasing H_2 selectivity with time. While the CO_2RR selectivity could be regained temporarily by a nitric acid wash of the cell, the following experiments always resulted in a similar performance loss. It is believed this H_2 selectivity increase was related to contamination from the metal quick connectors (most likely from Ni coming off the steel). The metal inlets were exchanged with 1/16" PTFE tubes inserted through the endplate. Further tests did not show the rapid increase in H_2 selectivity, thus this replacement resolved the contamination issue. A pressure-tight sealing was made using IDEX SuperFlangeless flat bottom ferrules (M-644-03, M-650). The inlet tube is extended beyond the ferrule and partially into the o-rings, thus sealing the side towards the flowplate. This sealing avoids the gas/liquid contacting the endplate or any metal part except the flowplate itself.

We expect the overall cell design to be capable of working under both highly acidic as well as alkaline conditions, since all gaskets can be exchanged depending on the specific use, and similarly the flowplates can be manufactured in a large variety of materials, with good electrical conductivity being the only general requirement. It should be noted that only neutral and moderately alkaline conditions were tested in this work.

2.2. Assembly

Due to the long casing, assembling the cell has substantial complexities. When assembling the cell, the membrane is first inserted slightly into the casing and then pushed all the way in using the flowplate with the GDE placed on top. In order to stabilize the membrane upon insertion, we used a 200 µm thick gasket (3-D printed from Stratasys VeroClear RGD810) that is placed on the anode side as the membrane otherwise tends to stick to the side when inserted. The gasket eases the assembly significantly and allows relatively consistent results. We have successfully tested PTFE, PFA, and FEP gaskets of similar dimensions. When fully inserted, the flowplate is tightened flush to the casing. This ensures that the height of the MEA is always the same making further alignment easier. The cell is then rotated 180 degrees so the cathode flowfield can be inserted with the cathode GDE lying on the top. The compression of the MEA is controlled by the tightening of the cathode flowfield to the casing.

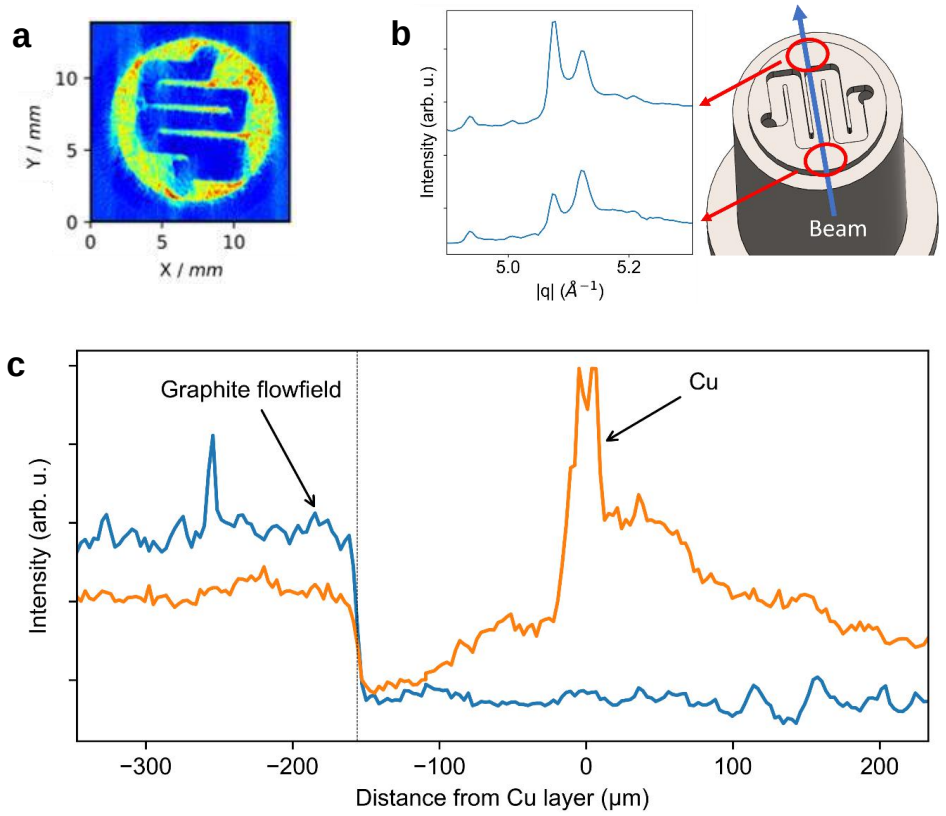

Figure 3. a) An example of an XRD-CT measurement taken at the height of the graphite flowfield. b) Example of a peak split from the graphite flowplate. The split comes when the beam diffracts on the two outer edges of the serpentine (reds circles), as these are distanced differently from the detector, and c) an example of how the surface of the land in the flow channel can be used to align the cell. The steeper the step in the graphite intensity is at -145 (dotted line), the more parallel is the cell and the beam. The orange line shows the Cu content indicating the height of the catalyst layer.

2.3. Alignment

The alignment of the cell for the grazing incident measurements is important in order to be able to investigate the different layers of the MEA correctly. The cell is mounted in a 6-axis alignment stage

so it can be moved, tilted and turned freely in all directions (x, y, z, θ, φ, χ), and thereby be aligned so the MEA is parallel to the beam. By using the polished land surface of the flowplate channels, it is possible to slowly tilt the cell, while scanning the height of the cell, until the signal from the surface of the land shows the steepest step function as shown by the example in Figure 3c. In order to minimize this iterative procedure, we have equipped the anode endplate with an edge fitting down in the holder. Thus the cell can be reproducibly mounted on the sample stage, giving a rough initial alignment of the cell.

2.4. Examples of data from an operando experiment

In a 2.5 h operando experiment, the cell was used for CO_2 electrolysis while WAXS scans were continuously acquired at various heights of the GDE by translating the cell in vertical direction. In this case, the line scan consisted of 50 different positions with a step size of 3 µm, and each line scan took around 100 s. In this way, we were able to obtain information on what happens inside the GDE (for more details, refer to Moss et al.[10]). Figure 4 shows 6 examples of WAXS patterns obtained at different positions in the beginning and toward the end of the experiment. The three patterns in Figure 4c are obtained at the height of the 150 nm thick catalyst layer and in all cases, clear peaks from the Cu catalyst can be seen. In the initial pattern obtained before the potential was applied peaks from both Cu and Cu_2O can be found, but after a very short time, the oxide phase disappears and the pattern does not change much from the beginning to the end of the experiment. This shows that the cell can be used to identify and follow the development of the crystalline phases of even a thin catalyst layer. Figure 4a and Figure 4b show patterns obtained approximately 90 µm and 45 µm from the catalyst layer towards the cathode flowfield. In both cases, a clear increase of the background at low q can be observed, which can be attributed to flooding of the GDE. In Figure 4a, the pattern obtained at the end of the experiments also shows the presence of a $KHCO_3$ phase caused by salt formations in the outer layers of the GDE. In total, it demonstrates how the cell can be used in operando experiments

to obtain important information not only on potential variations of the catalyst layer, but also of changes in the GDEs.

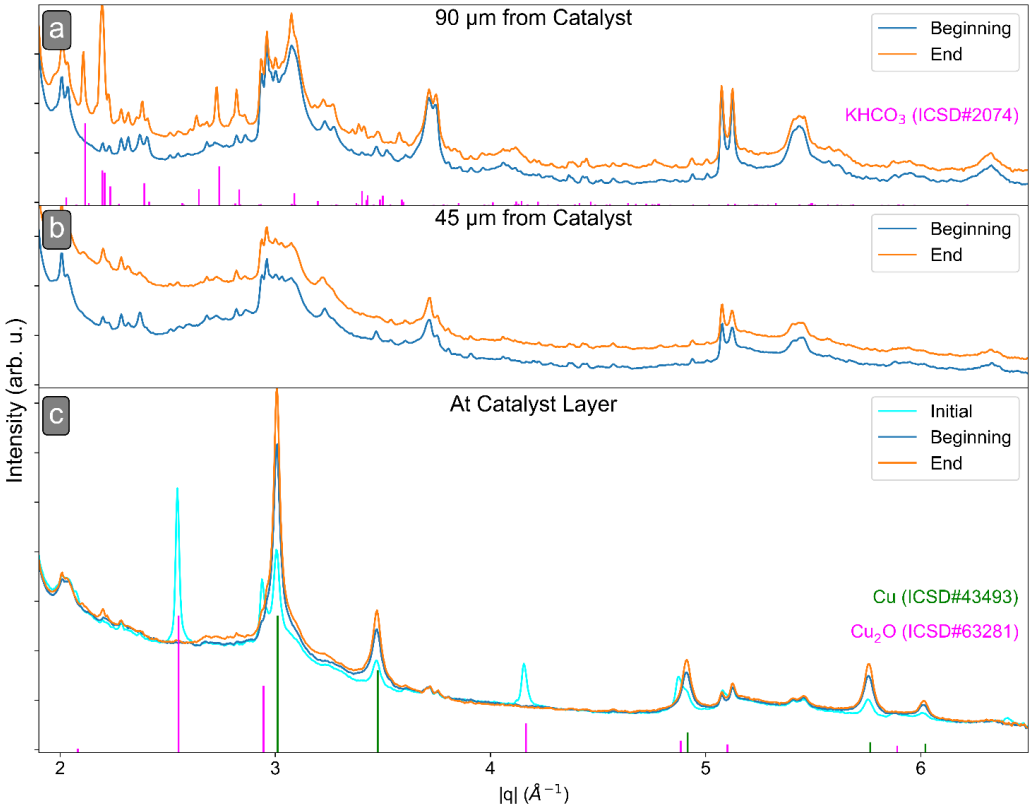

Figure 4 The figure shows patterns obtained from three different positions in the GDE at the beginning and towards the end of a 2.5 h experiment at 200 mA cm^{-2}. Subplot (c) shows patterns obtained at the catalyst layer position. The initial pattern contains both signs of Cu and Cu_2O, but the oxide phase disappears fast. In (b) obtained approximately 45 µm from the catalyst layer towards the cathode flowfield not much change can be seen except an increase in the background at low q caused by electrolyte flooding the GDE. Plot (a) shows a similar increase in the background, but also the presence of a $KHCO_3$ phase. Together the various patterns demonstrate how the cell can be used to identify changes inside a GDE.

2.5. Peak splitting and broadening

When scanning along the flow channels, we observed a set of split peaks from the graphite flowfield. The split occurs because the two ends are distanced differently from the detector, the so-called parallax effect (Figure 3b). The same effect is expected to occur with other elements of the cell, e.g. the catalyst layer, but here it will be seen as a peak broadening as the scattering occurs from a continuous film instead of the separated flowfield edges. This is one of the limitations of the cell that one should be aware of, but this can be accounted for during the post-processing of the data[11] and including this effect during the calibration of instrumental parameters.

2.6. Diffraction Tomography

We tested the cell to be used in a diffraction tomography experiment and found it highly suitable for the purpose. An example can be seen in Figure 3a and Figure 5. In such characterization, the pencil beam is scanned along the cell at different azimuthal angles, allowing reconstruction of the full diffraction pattern for each real-space voxel.[12–14] The circular geometry and relatively small width of the cell speeds the measurement process and it possible to obtain an acceptable resolution (in this case 69.5 μm but in principle down to the size of the X-ray beam) with a reasonable acquisition time (about 20 min per slice in this case, with increased time for increased resolution). However, we do in some cases observe damage to the center of the membrane after the tomography scans. While this can limit the tomography possibilities to an extent, carefully selected experimental conditions with respect to the total X-ray dose can mitigate this issue.

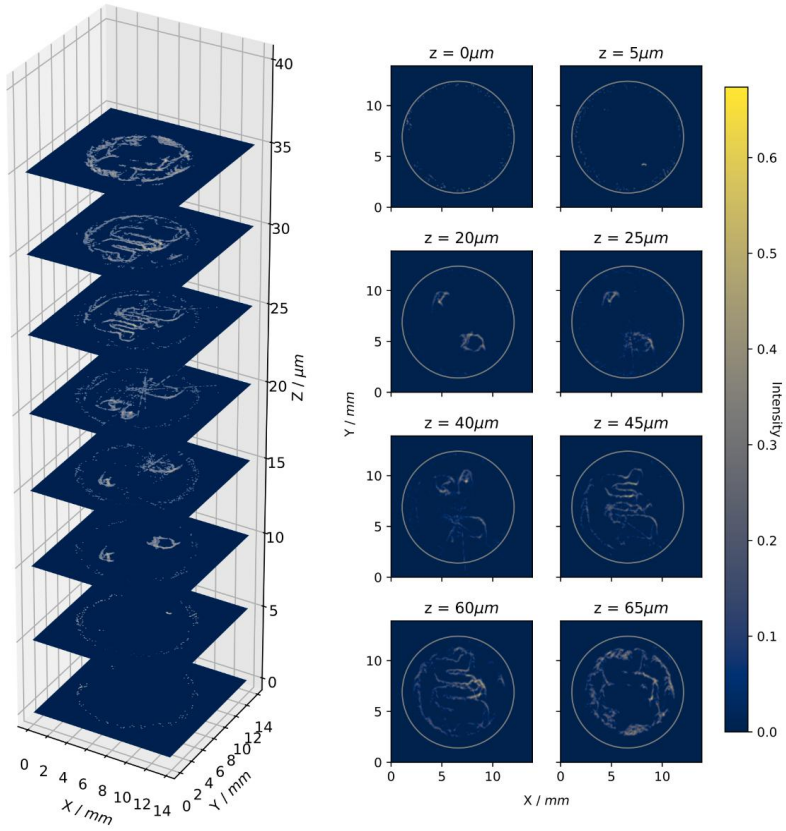

Figure 5. XRD-CT scan of the MEA's Cu catalyst layer before CO_2RR has taken place. The plotted intensity correspond to the surface oxide (Cu_2O) XRD peak (111), integrated in the range of q = 2.49 $Å^{-1}$ and q = 2.59 $Å^{-1}$. The dimensions of one voxel is 69.5μm and the dimensions of one slice is 200 x 200 voxels (13.9 x 13.9 mm^2). The protrusion of the catalyst layer into the flowfield is clearly detected.

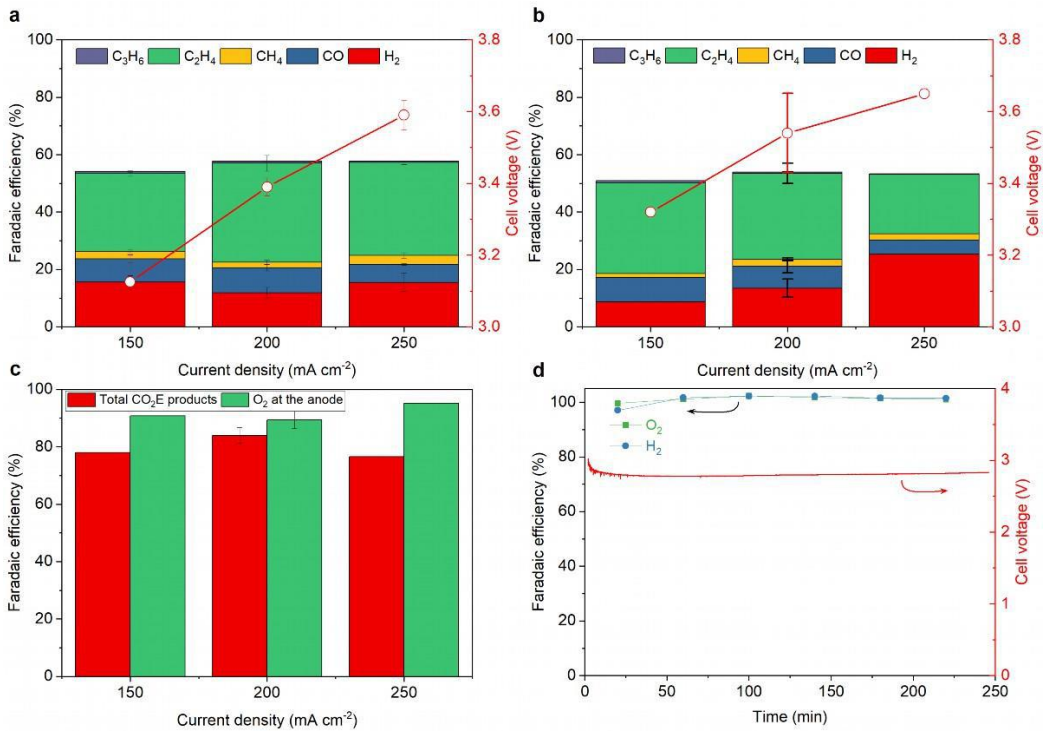

Figure 6. Comparison of electrocatalytic performance in terms of FE of gaseous cathodic products and cell potential over sputtered Cu GDEs (150 nm) in a MEA electrolyzer tested separately at two different locations: (a) without X-rays at DTU and (b) with X-rays at ESRF; (c) Comparison of total FE of CO_2RR products versus FE of O_2 at the anode in experiments performed during X-ray irradiation at ESRF; (d) shows an experiment where Ar was used instead of CO_2 showing a non-corroding anode as the H_2 and O_2 FEs are both 100%; The error bars in (a) show the standard deviation of three separate experiments where the 2nd GC injection was used to calculate the FE, while, the error bars in (b and c) for 200 mA·cm^{-2} show the standard deviation of four separate experiments. 150 and 250 mA cm^{-2} experiments shown in (b) (at ESRF) were only performed once due to time limitations.

2.7. Electrochemical Testing

In order to test if the electrolyzer can achieve commercially relevant current densities (≥ 200 mA cm^{-2}) for CO_2 reduction, we investigated the electrocatalytic performance of sputtered Cu GDEs at different current densities. Figure 6a shows that our MEA electrolyzer can produce a reasonable level of gaseous CO_2RR products including CO, CH_4, C_2H_4, C_3H_6, and H_2 during the initial stages of testing (data taken after 30 min of operation). We also see no indication that high energy (69 keV) X-ray illumination alters the electrocatalytic performance significantly. Figure 6a and Figure 6b show the cell performance in terms of faradaic efficiencies of gaseous products and cell potentials, with (6a) and without (6b) X-rays, at different current densities with all operating conditions such as catalysts (both cathode and anode GDE), AEM, and electrolyte kept identical. Furthermore, the experiments tested without X-rays were done at the Technical University of Denmark (DTU) whereas the X-ray irradiated experiments were done at the ID31 beamline of the European Synchrotron Radiation Facility (ESRF), demonstrating the reactor system is robust towards practical laboratory variations as well. In both cases in Figure 6a and Figure 6b, the total FE of products does not reach 100%. The explanation is mainly that the data does not include liquid product analysis. Figure 6c shows the total FE of CO_2RR products (red bars) at different current densities, including liquid products collected at the end of the experiment. With liquid product analysis being the total production of a 3 h experiment, and the gas products being the average of the continuous GC injections, the total faradaic efficiency is an estimated average of the entire experiment and we do therefore not expect the data to match 100% perfectly. The fact that the total FE gets to around 80% and not higher shows that there is still a significant fraction of the current not accounted for.

To account for the missing charge, we calculated the FE of oxygen (O_2) at the anode because if part of the CO_2RR products crosses the membrane and gets oxidized at the anode then the O_2 faradaic efficiency should also decrease. If we assume full anodic oxidation to CO_2, then there would be a one-to-one relationship between unaccounted faradaic efficiency at the cathode and non-O_2 evolution faradaic efficiency at the anode. This principle also assumes a non-corroding anode, which we show to be the case in Figure 6d where Ar was used instead of CO_2 so the only cathode reaction was HER. Here the faradic efficiencies of both H_2 and O_2 are 100%. Since the experiments with X-rays appeared to show the most substantial unaccounted for products, we analyzed the anodic O_2 evolution faradaic efficiency of these experiments. Despite Figure 6c confirming our hypothesis that O_2 faradaic efficiency at the anode does not reach 100% (and thus CO_2RR products are being oxidized) when comparing this to the total faradaic efficiency of CO_2E products as in Figure 6c, there is still a missing 5 to 15% FE. Evaporated liquid products (e.g. ethanol) were not analyzed at either the cathode or anode, which are potential sources for the missing faradaic efficiency.

3. Conclusion

We have presented a design for an electrolysis cell suitable for both water and CO_2 electrolysis with a geometric area large enough to be comparable to other cells, and with a design that allows for various X-ray diffraction and scattering techniques including tomography. The cell design has shown high repeatability in the electrochemical measurements, manageable X-ray background at high energies, and sufficiently easy assembly. The modular design with interchangeable flowplates of different materials makes the cell versatile and suitable for studying various electrochemical processes in MEAs at high current densities.

4. Methods

4.1. MEA setup and electrochemical measurements

For CO_2 electrolysis, a dry CO_2 gas (5N) was fed to the cathode flow-field at 30 sccm using a mass flow controller (Vöegtlin red-y smart series), and 60 ml of 0.1 M $KHCO_3$ anolyte was circulated at the anode using a digitally controlled diaphragm pump (KNF NF1.5TTDCB-4) set at 25% of its maximum speed (which roughly corresponds to 7.5 ml min^{-1}). For the cathode, a 150 nm layer of 6N sputtered Cu was deposited onto Sigracet 39 BB (Fuelcell Store), while, for the anode, a commercial IrO_2-based GDE (from Dioxide Materials, USA) was utilized. In all the experiments, an anion exchange membrane (Sustainion X37-50, Dioxide Materials, USA) activated in 1 M KOH solution and later kept in deionized water was used. All electrochemical experiments were performed in a two-electrode setup at a constant current. Current density of 150, 200, and 250 mA cm^{-2} were applied during galvanostatic measurements using a potentiostat (Biologic SP-300 and SP-240). For selectivity/faradaic efficiency calculations, the gaseous products formed at the cathode (and pre-washed into a deionized water chamber) were injected into an online GC (Agillent 6890A) equipped with a flamed ionization detector with a methanizer and a thermal conductivity detector for the detection of CO, CH_4, C_2H_4, C_3H_6, and H_2, respectively. High-purity argon (5N, Linde Denmark) was used as the carrier gas. The liquid products both collected at the cathode and the anode were detected using a liquid chromatograph (Agilent 1260 Infinity II) with 0.1 M $KHCO_3$ as a reference solution and 0.05 M H_2SO_4 as the internal solvent.

5. Acknowlegement

We would like to acknowledge the funding from Villum Fonden, part of the Villum Center for the Science of Sustainable Fuels and Chemicals (V-SUSTAIN grant 9455), as well as the ECOEthylene project from Innovation Fund Denmark (Grant# 8057-00018B). We acknowledge the European Synchroton Radiation Facility (ESRF) for the provision of synchrotron radiation using beamline ID 31.

6. References

1. Nitopi, S. *et al.* Progress and Perspectives of Electrochemical CO 2 Reduction on Copper in Aqueous Electrolyte. *Chem. Rev.* **119**, 7610–7672 (2019).

2. Carmo, M., Fritz, D. L., Mergel, J. & Stolten, D. A comprehensive review on PEM water electrolysis. *Int. J. Hydrogen Energy* **38**, 4901–4934 (2013).

3. Lu, Q. & Jiao, F. Electrochemical CO2 reduction: Electrocatalyst, reaction mechanism, and process engineering. *Nano Energy* **29**, 439–456 (2016).

4. Weng, L. C., Bell, A. T. & Weber, A. Z. Towards membrane-electrode assembly systems for CO2 reduction: A modeling study. *Energy Environ. Sci.* **12**, 1950–1968 (2019).

5. Ge, L. *et al.* Electrochemical CO2 reduction in membrane-electrode assemblies. *Chem* vol. 8 663–692 (2022).

6. Lees, E. W., Mowbray, B. A. W. W., Parlane, F. G. L. L. & Berlinguette, C. P. Gas

diffusion electrodes and membranes for CO2 reduction electrolysers. *Nat. Rev. Mater.* **7**, 55–64 (2022).

7. Farmand, M. *et al.* Electrochemical flow cell enabling operando probing of electrocatalyst surfaces by X-ray spectroscopy and diffraction. *Phys. Chem. Chem. Phys.* **21**, 5402–5408 (2019).

8. Hoffmann, H. *et al.* Development of a Modular Operando Cell for X-ray Imaging of Strongly Absorbing Silver-Based Gas Diffusion Electrodes. *J. Electrochem. Soc.* **169**, 044508 (2022).

9. Olesen, A. C., Rømer, C. & Kær, S. K. A numerical study of the gas-liquid, two-phase flow maldistribution in the anode of a high pressure PEM water electrolysis cell. *Int. J. Hydrogen Energy* **41**, 52–68 (2016).

10. Moss, A. B. *et al.* In Operando investigations of oscillatory water and carbonate effects in MEA-based CO2 electrolysis devices. *ChemRxiv* https://chemrxiv.org/engage/chemrxiv/article-details/634e8e6933997208578f58c9 (2022) doi:10.26434/chemrxiv-2022-54ccs.

11. Vamvakeros, A. *et al.* DLSR: A solution to the parallax artefact in X-ray diffraction computed tomography data. *J. Appl. Crystallogr.* **53**, 1531–1541 (2020).

12. Harding, G., Kosanetzky, J. & Neitzel, U. X-ray diffraction computed tomography. *Med. Phys.* **14**, 515–525 (1987).

13. Kleuker, U., Suortti, P., Weyrich, W. & Spanne, P. Feasibility study of x-ray diffraction computed tomography for medical imaging. *Phys. Med. Biol.* **43**, 2911 (1998).

14. Bleuet, P. *et al.* Probing the structure of heterogeneous diluted materials by diffraction tomography. *Nat. Mater*. *2008 76* **7**, 468–472 (2008).

B.2 In Operando investigations of oscillatory water and carbonate effects in MEA-based CO2 electrolysis devices

In Operando investigations of oscillatory water and carbonate effects in MEA-based CO_2 electrolysis devices

Asger B. Moss[a, †], Sahil Garg [a, †], Marta Mirolo[b], Carlos A. Giron Rodriguez [a], Roosa Ilvonen[b], Ib Chorkendorff[a], Jakub Drnec[b], Brian Seger[a, *]

[a]*Surface Physics and Catalysis (Surf Cat) Section, Department of Physics, Technical University of Denmark, 2800 Kgs. Lyngby, Denmark*

[b]*Experimental Division, European Synchrotron Radiation Facility, Grenoble, France*

[†]*Joint first authors: Asger B. Moss; Sahil Garg*

**Corresponding author: Brian Seger, Email: brse@fysik.dtu.dk*

Summary

Membrane electrode assembly (MEA) CO_2 electrolysis (CO_2E) is a promising route towards producing carbon-neutral chemicals, however, they often have stability issues related to flooding of the gas diffusion electrode (GDE). Thus, there is an urgent need to comprehend water management in these devices and to engineer electrodes that allow both stable and efficient electrocatalytic performance. Here, we investigated the possible causes of suppression in the CO_2 reduction reaction (CO_2RR) selectivity on Cu via *in operando* X-ray diffraction (XRD) analysis. The *in operando* XRD allowed us to monitor water and bicarbonate formation in the GDE, while in-line gas and mass chromatographs allowed us to correlate those changes to the cathode and anode product distribution during CO_2E. We found direct evidence for salt precipitation in the cathode GDEs, which causes water build-up and an increase in hydrogen evolution reaction (HER). We also observed that the increase in HER is related to a drop in total cell potential, caused by a shift in ion transport through the membrane from carbonates to more conductive hydroxide ions. Our results reported here also do not show any substantial catalyst-induced effects on CO_2RR. Thus this work suggests proper ion management is an important key to enhanced durability throughout the device.

Introduction

Storing renewable energy into chemical bonds/fuels via CO_2 electrolysis (CO_2E) is a promising approach to creating a carbon-neutral cycle while also curbing net CO_2 emissions. At present, copper-based membrane electrode assembly (MEA) electrolyzers allow a high rate of CO_2E to $\geq C_{2+}$ products.[1] However, the lack of stability, mainly seen as CO_2 reduction reaction (CO_2RR) being suppressed by the competitive hydrogen evolution reaction (HER), is a major factor delaying the deployment of CO_2E technology on a commercial scale.[2-6] Therefore, for the future development of these electrolyzers, it is crucial to investigate the exact cause of HER increase over time.

In recent years, many attempts have been made to determine what can cause the observed gradual selectivity change from CO_2RR to HER in a CO_2 electrolyzer.[2,3,6-8] Overall, it is believed that the issues arise from improper water management and the local reaction environment in the vicinity of the cathode.[9] For example, sufficient water is necessary to drive the CO_2E, but excess water can flood the gas diffusion electrode (GDE), which restricts CO_2 mass transfer, and shifts selectivity to HER.[5] The reductive potentials needed for CO_2RR lead to electrowetting of the GDE which provides a flooding mechanism.[2,7,10,11] Moreover, the highly alkaline environment created from the cathodic reactions will also equilibrate with CO_2 to form bicarbonate/carbonate (HCO_3^-/CO_3^{2-}) ions that easily permeate through anion exchange membranes (AEMs).[12,13] Besides lowering the CO_2 utilization, the CO_3^{2-} formation also exacerbates any CO_2 mass transport limitation at the cathode.[12,14] In addition, the hydroxyl groups produced at the cathode (from CO_2RR) can attack hydrophobic supports of the AEM, entailing potential durability issues. All these factors complicate the investigation of catalytic properties as it entangles CO_2 mass transport limitations, ionic conductivity, and water management.

Most of the cathode flooding mechanisms and concepts are based on fuel cell works[15-17] with only a few CO_2E studies showing indirect evidence of flooding in a flow cell (i.e. flowing catholyte between GDE and membrane) and zero-gap MEA-based CO_2 electrolyzers.[2,3,18,19] For instance, Leonard et al.[2] demonstrated both HER and electrochemical double-layer capacitance of the cathode GDE increased with the amount of charge passed through the GDE, where a higher electrochemical double-layer capacitance was attributed to a higher rate of cathode flooding.

Although there is a consensus that cathode flooding plays a role in affecting the CO_2RR/H_2 selectivity, an *in operando* visual inspection of a cathode GDE only allows the back surface to be analyzed. To the best of our knowledge, there has yet to be a direct *in operando* approach to show the flooding effect and its relation to product performance. Obtaining *in operando* results is especially important in CO_2E since the local reaction environment has been shown to vary with time and electrolysis conditions.[12] Furthermore, how a catalyst behaves and whether it changes due to these variations has also yet to be analyzed in-operando.

Another issue affecting CO_2RR/H_2 selectivity relates to salt depositions in the cathode GDE, which block gas flow to the catalyst.[20] There is a current debate as to if the salt deposits as alkali metal cation (K^+/Cs^+) carbonate[21-23] or bicarbonate,[20] however, this has only been investigated by computational models[23] or post mortem analysis.[24] Furthermore the three-way relationship between flooding, salt deposition, and variations in selectivity has rarely been investigated in depth.

In this work, we couple high flux 4th generation synchrotron X-ray source with superior phase contrast of diffraction phenomena to visualize the interior of an operational GDE to not only understand the relationship between selectivity, flooding, and salt deposition, but also to determine how this affects potential (at a constant current) and ion selectivity crossing through the membrane to the anode. Furthermore, this work analyzes structural changes within the Cu catalyst layer, such as how quickly it transitions from a surface oxide to metallic and whether it ripens, gets strained, or migrates within the GDE. It should be noted that the Bazylak group[18,19] has previously attempted to study both MEA and catholyte-based CO_2 electrolysis devices by X-ray radiography with a focus on gas bubble formations in the MEA and electrolyte layer respectively, however, they were unable to follow the evolution of different phases in the catalyst and to concomitantly analyze products, thus limiting the scope of their work.

One additional parameter that this work investigates is the oscillations that are often seen at CO_2 electrolysis devices devolving from CO_2RR to HER selectivity at the cathode. Oscillations typically occur at conditions on the borderline of stability, and thus while not typically consistent, they do provide transient conditions that allow for a much easier understanding of the processes leading to a loss in CO_2RR selectivity.

Results and discussion

Reactor performance

Figure 1 shows the reactor design and the measurement design: the synchrotron X-ray beam (5 $\mu m_{vertical}$ x 20 $\mu m_{horizontal}$) probed from the edge of the membrane to deep within the cathode GDE (~ 150 µm in total) by a continuous series of vertical line scans allowing for a comprehensive understanding of electrolyte, salt, and copper as a function of depth within the GDE. To accelerate durability issues related to a change in selectivity from CO_2RR to HER and limited time availability at the synchrotron, we did not use a Teflon gas diffusion layer[25] and low anolyte electrolyte concentrations[26] (e.g. 0.01 M), but rather a moderately hydrophobic carbon-based gas diffusion layer and a high concentration anolyte (0.1 M). Similarly, we used dry CO_2 instead of humidified CO_2.[6,27,28] Furthermore, we performed a series of operando experiments at different current densities (100, 150, 200, and 250 $mA \cdot cm^{-2}$) to show that these trends were comprehensive and not a function of a given current density regime.

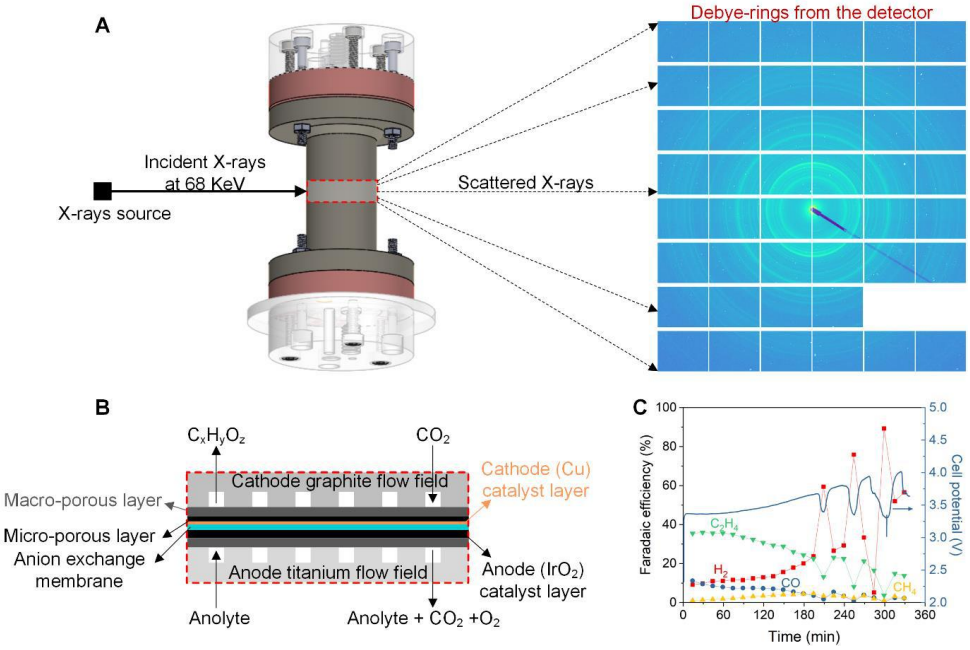

Figure 1. Sketch showing the *in operando* wide-angle X-ray scattering (WAXS) characterization of MEA CO_2 electrolyzers. A) scheme illustrating the design of MEA electrolyzer and the 2D diffraction pattern, B) enlarged view of the highlighted area in A) where

X-rays enter into the electrolyzer, C) FE of gaseous products of sputtered Cu GDEs at 200 $mA \cdot cm^{-2}$, without X-ray radiation. The experiment was performed with an inlet flow of 30 sccm of dry CO_2 on the cathode and 0.1 M $KHCO_3$ as an anolyte with Sustainion (X37-50) AEM. The incident X-ray beam size in A) was 5 x 20 μm^2.

The complexities of CO_2 electrolysis reactor designs entail a benchmark test is necessary to compare CO_2RR performance, especially given the X-ray cell in Figure 1 that was used for synchrotron work. Thus, without X-ray irradiation, experiments were done to show the performance of the cell. Without the need for beam alignment, this allowed us to test the cell immediately and produced clear and consistent results. Figure 1C shows concentrations of gaseous products from one of these preliminary tests with sputtered Cu using a conventional reactor design (used in our earlier studies)[13,29] at 200 $mA \cdot cm^{-2}$ over a ~ 6 hr test period. With liquid product analysis only being taken at the end of the experiment, the total faradaic efficiency is a convolution of the entire experiment. Nevertheless, it gives some insight into the electrochemical performance of the reactor, and Figure S1 shows the average faradaic efficiency for all products. It should be noted that while other works have proposed X-ray irradiation may influence CO_2RR performance,[19] we do not see any significant influence on performance related to X-ray irradiation (Figure S2).[30]

Figure 1C notably demonstrates a slow HER increase and C_2H_4 and CO decrease during the first 3 hr of the experiment. While methane increases slightly, its low overall faradaic efficiency entails it is difficult/unwise to analyze this further. Given that the only hydrophobic barrier used was the GDE, this decrease in overall CO_2RR was expected.[25] However beyond 3 hr, we found an oscillating trend in FE of gaseous CO_2RR products and HER, correlating well with the cell potential. These oscillations at the increased time were observed in approximately half of all samples tested. With oscillations often related to stability limits, this typically entails an inconsistent behavior: oscillations would occur after some time, but the frequency and intensity (in terms of voltage and productivity changes) would often vary.

To investigate both the increasing HER selectivity and the oscillating trends, we performed a series of *in operando* diffraction measurements using high-energy X-rays. By setting the current density and simultaneously measuring voltage, cathode, and anode selectivity, the state of Cu (oxidation level, micro-structure, particle size, and location), water content, and presence of crystalline $KHCO_3$ and K_2CO_3 via a variety of techniques, we gain unprecedented insights into the internal functioning of CO_2 electrolyzers. While we do expect flooding to be the main

cause of degradation, we wanted to ensure that the loss in CO_2RR selectivity did not arise from a change in the catalyst itself. To confirm this, we provide a detailed analysis in Supplementary Note 1 (including Figures S3 to S9) on how the Cu catalyst did not change (only native Cu_2O reduced to metallic Cu) and there was no IrO_2 crossover from the anode side to the cathode during CO_2 electrolysis.

Flooding of cathode GDE

The electrolyte distribution in the different parts of the cell, mainly GDE, is followed by deconvoluting the liquid phase diffraction pattern from the diffractograms.[31-33] We take advantage of the fact that the other solid amorphous phases do not change during the experiment and the change in the q-range 2.45 to 2.46 $Å^{-1}$ of diffractogram is mainly due to the electrolyte signal. Investigations of individual patterns confirm that the changes observed in the full q-range background match well with water. As an example, we show some diffraction patterns (Figure S10) and change in the background (Figure S11) at a single region in the GDE during different electrolysis time.

As seen in Figure 2, the overall electrolyte content in GDL increases slowly until ~100 min where it suddenly decreases. Given that the selectivity change seems to be correlating with the electrolyte content in the GDL, this slow increase of electrolyte content in the GDL is most likely the explanation for why we see a slow degradation in CO_2RR performance over time. For example, with GDL pores slowly filled with electrolyte, the CO_2 diffusion distance towards the catalyst layer increases, reducing CO_2 availability and causing a gradual shift from CO_2RR to HER. Interestingly, the electrolyte content is observed further toward the flow field than we expected. Recent studies reported that loss of GDE hydrophobicity during electrolysis (in addition to the formation of liquid products affecting the physical properties of the GDE) can cause the electrolyte to penetrate deeper into the GDE.[2,3,7] The electrolyte content seems to be highest in the outer layers of the GDL (> 50 µm), whereas there seems to be a relatively unchanged region closer to the catalyst layer (Figure 2). A similar trend is observed for all GDEs, and we expect this to be caused by the differences in PTFE content (25% vs. 5%) and pore size (<1 µm vs. 25-200 µm) of the micro-and macro-porous layers of the Sigracet 39 BB GDL resulting in different water management properties.[34,35] The degree of penetration of the microporous layer into the macroporous layer as well as GDL compression are unknown, thus an exact determination of the microporous/macroporous transition cannot be determined.

Nevertheless, this order of magnitude thickness does align with a relatively dry area between the catalyst and outer GDL layers.

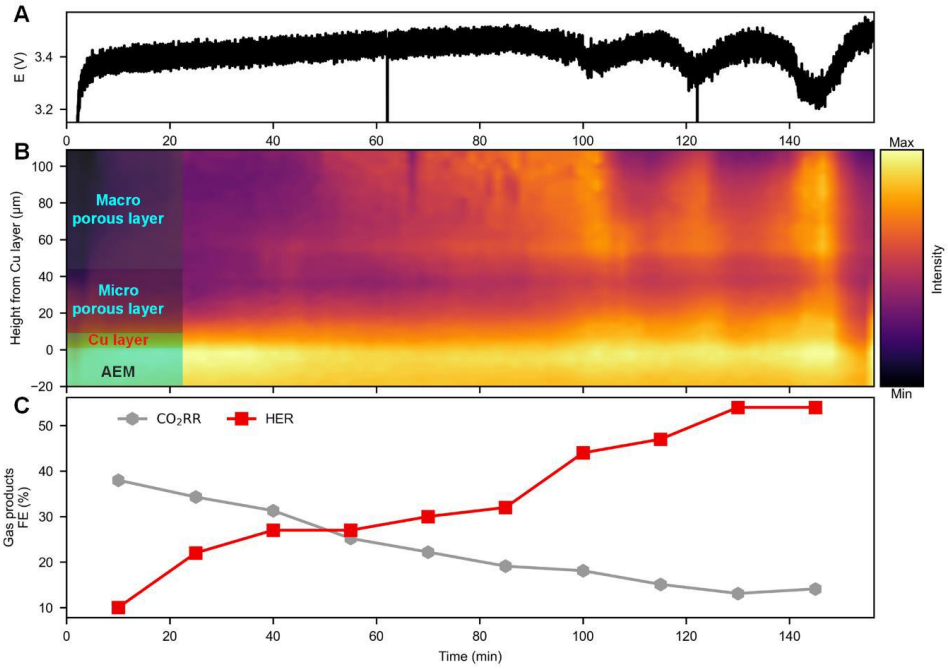

Figure 2. Change in (A) cell potential (E (V)), (B) electrolyte content, and (C) product selectivity of gaseous CO_2RR products and HER over electrolysis time. The experiment was performed at 200 $mA \cdot cm^{-2}$. A detailed version of the electrolyte plot and gaseous CO_2RR product selectivity is presented in Figures S12 and S13 of the Supplementary Information.

Initially, the slow increase in electrolyte content and the cell potential follow until around 90 min and both seem to correlate with a steady increase in HER indicating that slow flooding is causing this performance degradation. From around 90 min to 100 min the HER seems to increase faster, but at this point, the potential starts to decrease while the electrolyte content continues to increase. The initial correlation seems to break at this point indicating that a different mechanism is accelerating the performance degradation. Once the potential reaches a local minimum (~100 min), the potential starts to increase again. Shortly after (~105 min), the water content drastically starts to decrease. The oscillation repeats in roughly 20 min cycles with a 3-5 min delay between the minimal potential and maximum electrolyte content.

Such oscillations, both in terms of cell potential and electrolyte content in GDL could be caused by changes in the anode potential, e.g., from anode degradation or bubble formation, or could be due to changes in gas pressure and temperature in the electrolyzer. There are, however, no

indications that any of this is the cause. We measured the anode potential by putting a reference electrode in the inlet flow channel of the anolyte. The anode potential remained stable throughout the CO_2 electrolysis time, indicating that any change happening in the cell potential is either from changes in the cathode potential or membrane ohmic losses (Figure S14). Small periodic variations in the cathode inlet pressure (Figure S15) were observed, but with different periodicity (caused by a slight overpressure in the GC). Also, no variation in cathode flow-field temperature was observed during the electrolysis (Figure S15). It should be noted that the cells used for experiments shown in Figure 1C and Figure 2 were both tested with the same parameters, but their oscillations and CO_2RR selectivity trends varied significantly, pointing to the chaotic nature of the processes driving these fluctuations.

Figure 2C shows the faradaic efficiency of the cathodic gas products (Figure S13 shows the exact CO_2RR product breakdown from Figure 2). The FE of H_2 gradually increases during the first 80 min before further rapid increase at 100 min. For the next 15 min, the rate of H_2 selectivity increase slows down slightly before the start of the second cycle of acceleration, and then the deceleration of the H_2 selectivity increase. The slow sampling rate of the gas chromatograph dilutes the trends, but there is a notable correlation between the electrolyte content in the GDE and the level at which HER increases.

The aforementioned shift from a high device potential during primarily CO_2RR to a lower potential during the spike of H_2 selectivity provides an intriguing result as this is contrary to what is seen in the first 80 minutes, where as HER increases, there is a gradual increase in operating potential. At the local pH's produced during high current density CO_2RR,[36] it is well established that CO_2RR has a lower onset potential than HER (otherwise CO_2RR would not occur[37-39]). While this argument is in agreement with the first 80 minutes of the experiment, during the fluctuations there must be an additional factor in play causing a higher HER and lower voltage. For example, an ohmic resistance decrease in the membrane (or other places within the device) or fundamental variation in catalytic activity could potentially be the cause of lower cell potential and increased HER. The conductivity of the ion exchange membrane is well known to be a function of the ion being transferred. For instance, the conductivity of a Sustainion membrane X-24 membrane in $KHCO_3$ is 24 $mS \cdot cm^{-1}$ whereas the same membrane in KOH shows a conductivity of 66 $mS \cdot cm^{-1}$.[40] While this work uses a different version of Sustainion, we expect the trends to still hold. It is well established that analyzing the anodic CO_2 to O_2 ratio in CO_2 electrolysis devices works as a proxy to determine what species (i.e.

HCO_3^-, CO_3^{2-}or OH^-) is transferring through the membrane.[12,13,41] A CO_2 to O_2 ratio of 4 means HCO_3^- transfer, a ratio of 2 means CO_3^{2-}, and a ratio of 0 means OH^- transfer.

Since carbonates crossing over to the anode reacts quickly with protons and release CO_2, we cannot calculate the migration of carbonates by measuring the anolyte concentration. Instead, to understand if the membrane could be contributing to potential oscillations, we looked into the anodic CO_2 to O_2 ratio. To show these oscillations are current independent, the experiment was done at 150 $mA \cdot cm^{-2}$, and the results are shown in Figure 3 (Figure S16 shows a detailed version of Figure 3B). Again, we see the link between electrolyte content, cell potential, and faradaic efficiency of H_2, albeit much clearer. Figure S17 shows detailed cathodic gas product distribution from the GC whereas Figure S18 shows cathodic and anodic gas products from a mass spectrometer that was operated concurrently with the GC. In Figure 3D we can now see that the CO_2 to O_2 ratio is initially near 2 entailing carbonate transfer, which is expected of a device with a well-functioning cathode.[12,13] However at the point where we start seeing a change in potential, we see a drop in the CO_2 to O_2 ratio entailing a partial switch from a carbonate transfer to a hydroxide transfer. Given that OH^- conducts more efficiently through the membrane, this at least partially explains the drop in potential. Furthermore, at the point when the membrane again becomes more carbonate-rich (i.e. CO_2:$O_2 \approx 2$) the potential also increases again. It should be noted that the CO_2:O_2 ratio is a function of both anolyte equilibration time and GC measurement time, thus it is hard to quantify the lag between the CO_2:O_2 ratio and potential (also there was a lag of 9 min between the cathode and anode gas injection to the GC).

Another point to note is that during CO_2 electrolysis the surface is covered by a certain percentage of CO, and thus this is known to decrease H_2 evolution catalytic activity substantially.[37] In the case where the catalyst is CO_2 deficient, this will entail enhanced activity and should result in a lower device potential.[37] Given that a CO_2 deficiency will result in both an increase in membrane conductivity and a catalytic improvement for H_2 evolution, these two parameters are intrinsically coupled, and thus concluding the relative impact of each is beyond the scope of this work (especially since this involves a chaotic oscillatory system being analyzed).

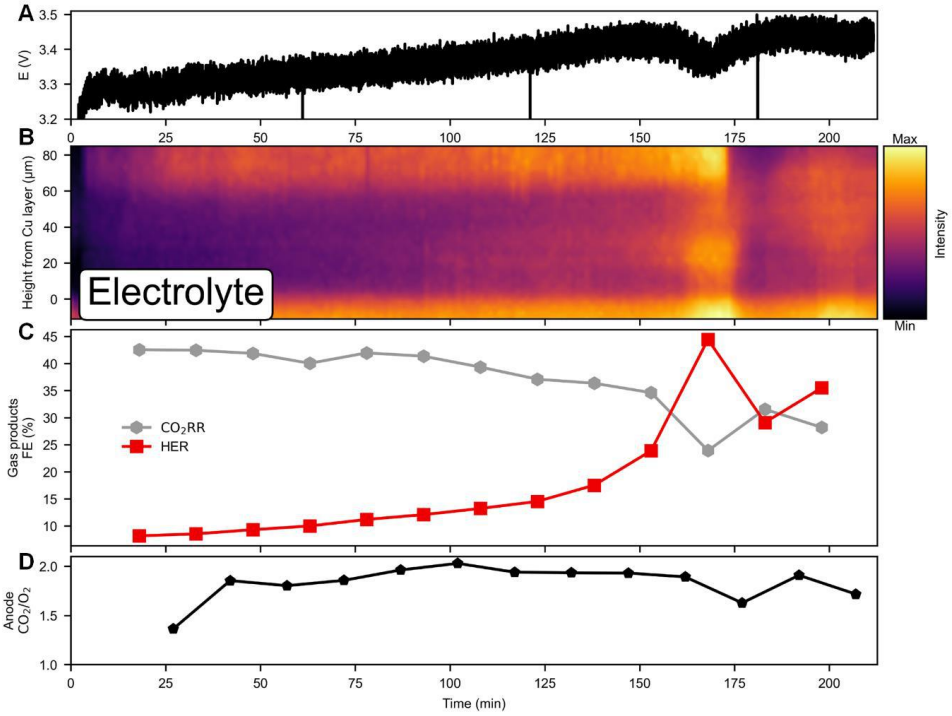

Figure 3. Change in (A) Cell potential (E (V)), (B) electrolyte content, (C) product selectivity of gaseous CO_2RR products and HER, and (D) CO_2/O_2 ratio at the anode over electrolysis time. The experiment was performed at 150 mA·cm^{-2}.

If the fundamental issue was mainly flooding of the cathode, this would dilute the concentration of cathodically produced hydroxyl ions (OH^-). The dilution of OH^-'s would lower the pH, entailing a shift towards HCO_3^- instead of CO_3^{2-}, and an increasing CO_2/O_2 ratio approaching 4.[41] However, Figure 3D shows just the opposite trend, this decrease can only occur by a lack of CO_2, entailing OH^- transfer through the membrane since this case would have a CO_2/O_2 ratio of 0. Another quite interesting observation, though less clearly visible, is that the potential and shift in selectivity seem to be preceding the flooding slightly. This effect was seen in all synchrotron experiments where fluctuations were clearly visible (see Figures S19-S22 for additional experiments). As it is well known that salt precipitation occurs during CO_2E and degrades performance,[20,22] our following experiments focused on monitoring salt formation and whether we could conclude that this was the instigator of the oscillations.

Salt precipitation in the cathode GDE

Salt depositions are in crystalline form, and thus can easily be isolated via their diffraction pattern (See supporting information for details). By operating another experiment, this time at 100 mA·cm^{-2}, we were able to achieve distinct oscillations while monitoring electrolyte and carbonate content as shown in Figure 4. Unfortunately, we do not have cathodic GC or MS data for this synchrotron experiment (due to a technical issue), however, the anode CO_2 to O_2 ratio (Figure S23) shows trends consistent with previous experiments.

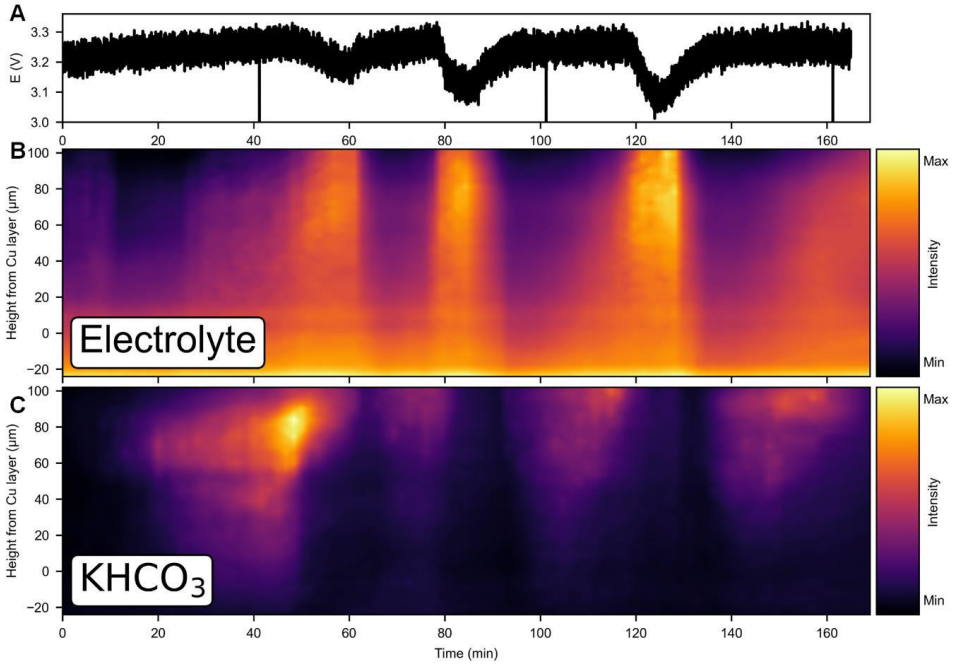

Figure 4. Changes in (A) cell potential (E(V)), (B) electrolyte content, and (C) salt precipitation in the cathode GDE over electrolysis time. The $KHCO_3$ salts were found by integrating two $KHCO_3$ peaks at 2.19 and 2.20 Å^{-1} and subtracting the background. The plot at the top shows the simultaneous change in full cell potential. This experiment was performed at 100 mA·cm^{-2}.

One of the most interesting characteristics of Figure 4 is that salt precipitation occurs preceding the substantial increase in electrolyte content. These results are in contrast to previous reports that assumed salt precipitation is a result of massive electrolyte flooding.[7,8] Even more interesting is that $KHCO_3$ was found (as validated by seeing all its XRD peaks - see Figure S24), but no XRD peaks attributed to K_2CO_3 were found. Previous reports[21-23,42] have indicated seeing K_2CO_3 at the cathode, and given that it is known that CO_3^{2-} is primarily transferring

through the membrane (see Figure 3 or Figure S23), it would be expected that any liquid electrolyte at the cathode would be in the form of K_2CO_3. While it is not clear why $KHCO_3$ deposits to begin with instead of K_2CO_3, one hypothesis is that there become localized areas of more neutral pH's, due to higher CO_2 concentrations near the flow field, thus allowing the formation of $KHCO_3$ and since the solubility of $KHCO_3$ is less than half that of K_2CO_3,[43] this leads to the salt deposition.

As we start (before electrolysis) with no potassium at the cathode and the solubility limit of both $KHCO_3$ (3.62 M at 25°C)[43] and K_2CO_3 (8.03 M at 25°C)[43] is significantly higher than the 0.1 M $KHCO_3$ used as anolyte, it is evident that a fair amount of potassium ions are transported from the anode to the cathode by electrostatic force. This will be counterbalanced by diffusion when the concentration at the cathode exceeds the concentration of the anolyte. At a certain concentration of potassium at the cathode, the two will outbalance and the net flux of potassium ions across the membrane is expected to be zero. This, of course, is under the assumption that potassium is not diffusing away from the membrane-electrode interface and into the GDE and flowfield, but this is exactly what we observe. The GDE can therefore be regarded as a potassium reservoir being filled up during the electrolysis reaction. This raises the question if the observed oscillations in potential and selectivity could be caused by changes in potassium concentration either at the cathode or the anode. Given the almost constant electric field across the membrane (as seen from the almost constant cell potential in all experiments), it seems unlikely that the electrostatic driving force for potassium transfer towards the cathode should change significantly during CO_2E. The osmotic driving force is of course changing as the concentration at the cathode side increases, but this is only until the concentration reaches the solubility limit. Hereafter a further potassium transfer would just fill up the GDE, as observed. We, therefore, do not expect any oscillating behavior of the potassium concentration in the vicinity of the cathode catalyst during the electrolysis. It is though relevant to ask if the concentration at the anode is lowered so much that the potassium flux is affected. Assuming that all of the cathode GDE volume (~ 0.015 ml) is filled up with potassium bicarbonate salt, 5.5% of the potassium in the 60 ml 0.1 M anolyte reservoir would be consumed (see Supplementary Note 2 for calculation). The concentration of the remaining anolyte would then be 0.094 M.

To exclude that such changes in anolyte concentration can cause oscillations, we performed a control experiment with 0.01 M $KHCO_3$ as the anolyte. The experiment shows similar cell potential and selectivity behavior during the first 3 h as seen in Figure S25. As expected,

oscillations occurred, though slightly later than what was observed in 0.1 M $KHCO_3$ experiments indicating any change in potassium concentration (irrespective of the initial concentration) in the anolyte would not cause the observed oscillations.

While finding a clear reason for the formation of $KHCO_3$ is challenging, there are highly plausible reasons for its disappearance once the electrolyte reaches the salt crystals. The most obvious is that the aqueous solution simply dissolves it, but a more subtle point is that this electrolyte is expected to be highly alkaline and lacking carbonates (as denoted by OH^- rather than CO_3^{2-} crossing over the membrane). This alkaline environment (i.e. KOH based) would entail that the $KHCO_3$ rapidly converts to the much more soluble K_2CO_3, which would help in solubilizing the $KHCO_3$ crystals and preventing the dissolved salt to precipitate even when the electrolyte level (in the GDE) is once again lowered.

To further confirm that salt precipitation is triggering the observed oscillations in CO_2RR, we did multiple CO reduction (COR) experiments. As expected, we do not see any oscillating phenomenon in cell potential and COR products/HER selectivity (Figure S26). In addition, no signs of salt precipitation were found in the cathode flow field post-COR.

Comprehensive analysis of oscillations

Based on the preceding analysis, we can link many of these effects to provide a comprehensive mechanism for the oscillatory nature seen during CO_2 electrolysis. Figure 5 summarizes the mechanism we feel is plausible based on this analysis. It is important to note that often some of these processes are taking place simultaneously and the order in which they are taking place may be slightly different than proposed. Nevertheless, this does give an overview of the major processes taking place.

Initially, we observe a small amount of electrolyte deep into the GDL and we see the formation of $KHCO_3$ crystals. This causes a blockage in the GDE preventing sufficient CO_2 access. We base the hypothesis that the salt crystals are blocking the CO_2 access on the fact that we see both a decrease in CO_2 reduction selectivity in favor of HER and a decreased carbonate crossing over the membrane. Thus, from a pure mass transfer standpoint, there appears to be a loss of CO_2 reaching the catalyst/membrane interface. This leads to anions transporting through the membrane shift to OH^-, causing a drop in membrane ohmic losses and thereby decreasing the overall cell potential. Additionally, the lack of CO_2 and its intermediate such as CO bound to the catalyst also increases catalytic activity and decreases the potential. Beyond this point, the electrolyte then floods the cathode. Given that the incoming cathode gas is dry CO_2, this

electrolyte/water must be coming from the anode, but the reason for this increased water penetration is still unclear. One factor that could lead to increased water penetration is the fact that membranes in the OH^- form are more hydrated than in the CO_3^{2-},[44] and this increased swelling could potentially lead to an increased water transfer from the anode to the cathode. This hypothesis is supported by clear observations of local water content increase inside the membrane (electrolyte heatmaps in Figures 2 to 4). However, more experiments would be needed to verify this effect. Another factor is that osmotic drag will naturally pull water from the anode to the cathode to hydrate the salts. Given the complexity of the system, there could be additional factors not accounted for, thus currently all that can be determined for certain is that water does return to the cathode.

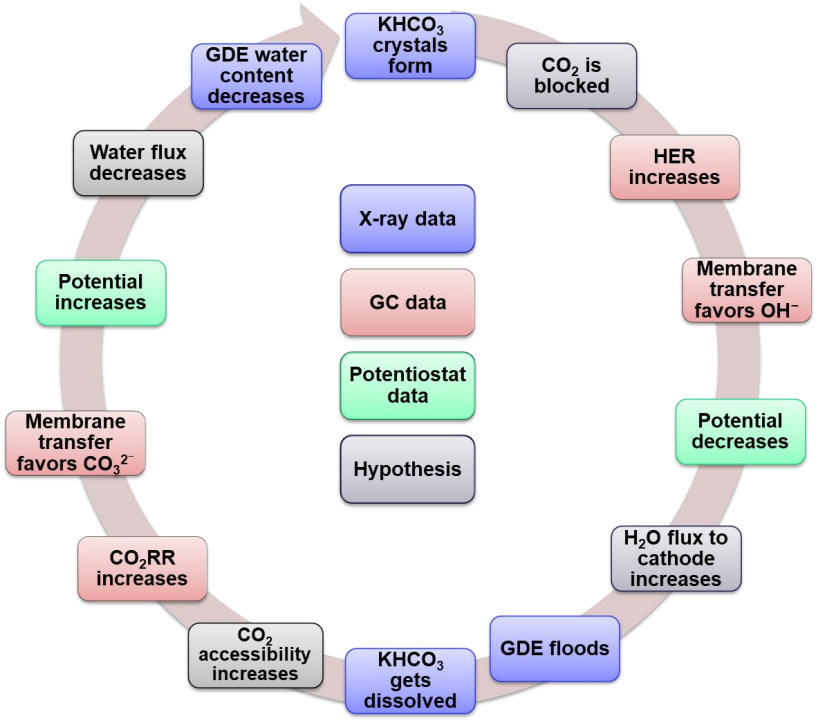

Figure 5. Proposed mechanism to illustrate the oscillating phenomenon of salt precipitation and dissolution causing a change in electrocatalytic performance of the CO_2 electrolyzer. It should be noted that the illustration only describes the oscillations. An underlying performance degredation due to slow flooding and potassium build up at the cathode should be added. The total observed phenomena would therefore be more like a degrading spiral.

Conclusion

While the oscillatory effects seen in this work are clearly not desired from an applied standpoint, these oscillations enabled us to gain deep fundamental scientific insight into the processes that lead to loss of selectivity to CO_2 products by analyzing these oscillations via monitoring a wide variety of parameters such as potential, cathode and anode products, Cu oxidation state, as well as location and intensity of Cu, electrolyte content and salt deposition in the GDE. Although our results showed that Cu is relatively stable (at least at the micro-scale), there is a highly interconnected relationship between electrolyte/water penetration into the GDE, salt deposition, membrane ion conduction (CO_3^{2-} vs. OH^-), and overall device potential at a given current density. Though this work opens new questions, it does clarify that mitigating salt deposition throughout the gas diffusion layer is essential to obtaining long-term stability. Thus, further works on durability should focus on enhanced reactor designs, salt management processes, and more resistant gas diffusion layers to help resolve these issues.

Experimental methods

Electrode preparation and zero-gap MEA setup

The cathode GDEs for all the experiments were prepared by sputtering a 150 nm layer of 6N Cu onto a Sigracet 39BB carbon paper (Fuel Cell Store) in a vacuum environment (10^{-5} ~ 10^{-6} Torr) at a deposition rate of ~ 1 Å s^{-1} under 5 sccm Ar, total pressure 3 mTorr, and at room temperature. The anode GDE was a commercial IrO_2-coated GDE (Dioxide Materials).

All electrochemical CO_2E tests were performed in a 0.64 cm^2 MEA-based CO_2 electrolyzer. Figure 1 shows a schematic description of the cell (for more details, refer to our X-ray cell article[30]). The MEA is assembled by placing the anion exchange membrane (AEM, Sustainion X37-50, Dioxide Materials) between the cathode and anode. The as-received AEMs were presoaked and activated in 1 M KOH for 24 h and then washed with deionized water (18.2 MΩ). After activation, the AEMs were stored in deionized water before use. The cell consists of a titanium serpentine flow field on the anode side and a graphite serpentine flow field on the cathode side. The two flow fields are inserted in a PEEK housing enabling X-ray diffraction experiments with the incident beam being in-plane with the MEA.

Electrochemical measurements

A dry CO_2 gas (for non-X-ray irradiated samples at DTU (Figure 1C) Linde, 5N, for X-ray irradiated samples at ESRF Air Products, 5N) was supplied to the cathode flow field with a flow rate of 30 sccm using mass flow controller (Vöegtlin red-y smart series), while, the anode was fed with 0.1 M $KHCO_3$ (Sigma-Aldrich, 99.99% metal basis). Cathode inlet pressure was measured using a pressure transducer (Brooks Instrument, SolidSense II Series). A constant volume of 60 ml anolyte was recirculated through the anode with a digitally controlled diaphragm pump (KNF NF1.5TTDCB-4) set to 25% corresponding to approximately 7.5 ml/min. The anolyte reservoir was purged with Ar (at 30 sccm) to carry the gases formed at the anode for gas chromatography analysis. All electrochemical measurements were performed under galvanostatic mode with a potentiostat (Biologic SP-300 and SP-240) and the cell voltages are reported without any *iR* correction. A leakless Ag|AgCl reference electrode was introduced before the anolyte inlet at the anode side to measure the anodic potential.

Product analysis

The outlet cathode gas stream was passed through a gas wash to extract the liquid CO_2RR products. All cathodic gas products such as H_2, CO, CH_4, C_2H_4, and C_3H_6 products were analyzed using a gas chromatograph (GC, Agilent 6890A) equipped with a thermal conductivity detector, flame ionization detector, and capillary columns (45m×0.530mm 40.0 Micron HP-PLOT/Q and 30 m×0.530 mm 15.0-micron HP-Molesieve). Argon (Linde, 5N) was used as a carrier gas in the GC. The gas chromatograph also analyzed gases such as CO_2 and O_2 at the anode side. The volumetric gas flow rates at the outlet of both the cathode and anode were measured by introducing a known concentration of N_2 (Linde, 5N) via a mass flow controller in the respective outlet stream and then subsequently calculated the concentration through a gas chromatograph. The liquid CO_2RR products both at the cathode (extracted from the gas wash) and at the anode (diffused through the anion exchange membrane) were quantified using a liquid chromatograph (Agilent 1260 Infinity II) with 0.1 M $KHCO_3$ as the reference solution and 0.05 M H_2SO_4 as the internal solvent.

In-operando X-ray measurements

Synchrotron wide-angle X-ray scattering (WAXS) measurements were performed at the ID31 beamline of the European Synchrotron Radiation Facility (ESRF) in Grenoble, France. The high-energy X-ray beam (68 keV) was focused ($5\mu m_{vertical}$ x 20 $\mu m_{horizontal}$) on the MEA in grazing incidence mode (beam parallel to the MEA layers), and the scattered signal was

collected using a Dectris Pilatus CdTe 2M detector positioned 710 mm behind the sample. The energy, detector distance, and tilts were calibrated using a standard CeO_2 powder and the 2D diffraction patterns were reduced to the presented 1D curves using the pyFAI software package.[45] To avoid the high, spotty, and randomly distributed signal arising from the gasket in the cell, iterative filtering has been implemented in the azimuthal integration (referred to as "sigma_clip" integration in the azimuthalIntegrator Module in the pyFAI package).

Rietveld refinements of the WAXS patterns were performed to extract the crystallite sizes, lattice parameters, and microstrains using the Fm3m structure of Cu metal and the GSAS-II software.[46] The instrumental parameters were determined by the refinement of a CeO_2 standard sample. As repetitive vertical scans across the cathode GDE and the membrane were performed during the experiment, the background subtraction consisted of removing the GDE signal from the catalyst signal.

Electrode characterization

The surface composition of the used cathode GDEs was determined using a Kratos Axis Ultra DLD X-ray photoelectron spectrometer (XPS). All the measured spectra were acquired using a monochromatized Al K_α radiation at 15 kV and 15 mA. The binding energy of the acquired spectra was calibrated using C 1s binding energy to 284.8 eV. Ion-scattering spectroscopy profiles of the cathode GDEs were also done to identify any contamination after CO_2 electrolysis.

Supplementary information

The authors declare that the data supporting the findings of this study are available within the paper and its Supplementary Information files. The processed data for all figures are available at https://figshare.com/s/164b8df7d20e8332c15d including integrated X-ray data. Raw X-ray data generated at the European Synchrotron Radiation Facility (ESRF) large-scale facility are available at https://doi.esrf.fr/10.15151/ESRF-ES-439498753 from 2024. Alternatively, this data can be available from the corresponding author upon request.

Acknowledgements

The research leading to these results has received funding from the European Union's Horizon 2020 research and innovation programme under grant agreement No 85144, (SELECT-CO_2) as well as the ECOEthylene project from Innovation Fund Denmark (Grant# 8057-00018B),

and the Villum Center for the Science of Sustainable Fuels and Chemicals grant 9455. We acknowledge the European Synchroton Radiation Facility (ESRF) for the provision of synchrotron radiation using beamline ID 31.

Author contributions

A.B.M. and S.G. carried out all electrochemical measurements, conducted data analysis, and wrote the manuscript with input from all co-authors. M.M. and J.D. assisted in performing *in operando* experiments (including data analysis) at ESRF and M.M. wrote the part on how *operando* measurements were performed. C.A.G.R. helped with electrochemical measurements performed at ESRF and liquid product analysis. R.I. helped with performing data analysis for the X-ray data. I.C. and B.S. conceived the project and oversaw its development.

Declaration of interests

The authors declare no competing interests.

References

1. Higgins, D., Hahn, C., Xiang, C., Jaramillo, T.F., and Weber, A.Z. (2019). Gas-Diffusion Electrodes for Carbon Dioxide Reduction: A New Paradigm. ACS Energy Letters *4*, 317-324. 10.1021/acsenergylett.8b02035.
2. Leonard, M.E., Clarke, L.E., Forner-Cuenca, A., Brown, S.M., and Brushett, F.R. (2020). Investigating Electrode Flooding in a Flowing Electrolyte, Gas-Fed Carbon Dioxide Electrolyzer. ChemSusChem *13*, 400-411. https://doi.org/10.1002/cssc.201902547.
3. Leonard, M.E., Orella, M.J., Aiello, N., Román-Leshkov, Y., Forner-Cuenca, A., and Brushett, F.R. (2020). Editors' Choice—Flooded by Success: On the Role of Electrode Wettability in CO_2 Electrolyzers that Generate Liquid Products. Journal of The Electrochemical Society *167*, 124521. 10.1149/1945-7111/abaa1a.
4. Weng, L.-C., Bell, A.T., and Weber, A.Z. (2018). Modeling gas-diffusion electrodes for CO_2 reduction. Physical Chemistry Chemical Physics *20*, 16973-16984. 10.1039/C8CP01319E.
5. Reyes, A., Jansonius, R.P., Mowbray, B.A.W., Cao, Y., Wheeler, D.G., Chau, J., Dvorak, D.J., and Berlinguette, C.P. (2020). Managing Hydration at the Cathode Enables Efficient CO_2 Electrolysis at Commercially Relevant Current Densities. ACS Energy Letters *5*, 1612-1618. 10.1021/acsenergylett.0c00637.
6. Wheeler, D.G., Mowbray, B.A.W., Reyes, A., Habibzadeh, F., He, J., and Berlinguette, C.P. (2020). Quantification of water transport in a CO_2 electrolyzer. Energy & Environmental Science *13*, 5126-5134. 10.1039/D0EE02219E.
7. Yang, K., Kas, R., Smith, W.A., and Burdyny, T. (2021). Role of the Carbon-Based Gas Diffusion Layer on Flooding in a Gas Diffusion Electrode Cell for Electrochemical CO_2 Reduction. ACS Energy Letters *6*, 33-40. 10.1021/acsenergylett.0c02184.
8. Li, M., Idros, M.N., Wu, Y., Burdyny, T., Garg, S., Zhao, X.S., Wang, G., and Rufford, T.E. (2021). The role of electrode wettability in electrochemical reduction of carbon dioxide. Journal of Materials Chemistry A. 10.1039/D1TA03636J.

9. Nesbitt, N.T., and Smith, W.A. (2021). Water and Solute Activities Regulate CO_2 Reduction in Gas-Diffusion Electrodes. The Journal of Physical Chemistry C *125*, 13085-13095. 10.1021/acs.jpcc.1c01923.
10. Jeanty, P., Scherer, C., Magori, E., Wiesner-Fleischer, K., Hinrichsen, O., and Fleischer, M. (2018). Upscaling and continuous operation of electrochemical CO_2 to CO conversion in aqueous solutions on silver gas diffusion electrodes. Journal of CO2 Utilization *24*, 454-462. https://doi.org/10.1016/j.jcou.2018.01.011.
11. Löwe, A., Rieg, C., Hierlemann, T., Salas, N., Kopljar, D., Wagner, N., and Klemm, E. (2019). Influence of Temperature on the Performance of Gas Diffusion Electrodes in the CO_2 Reduction Reaction. ChemElectroChem *6*, 4497-4506. https://doi.org/10.1002/celc.201900872.
12. Ma, M., Clark, E.L., Therkildsen, K.T., Dalsgaard, S., Chorkendorff, I., and Seger, B. (2020). Insights into the carbon balance for CO_2 electroreduction on Cu using gas diffusion electrode reactor designs. Energy & Environmental Science *13*, 977-985. 10.1039/D0EE00047G.
13. Larrazábal, G.O., Strøm-Hansen, P., Heli, J.P., Zeiter, K., Therkildsen, K.T., Chorkendorff, I., and Seger, B. (2019). Analysis of Mass Flows and Membrane Cross-over in CO_2 Reduction at High Current Densities in an MEA-Type Electrolyzer. ACS Applied Materials & Interfaces *11*, 41281-41288. 10.1021/acsami.9b13081.
14. Jeng, E., and Jiao, F. (2020). Investigation of CO_2 single-pass conversion in a flow electrolyzer. Reaction Chemistry & Engineering *5*, 1768-1775. 10.1039/D0RE00261E.
15. Hussaini, I.S., and Wang, C.-Y. (2009). Visualization and quantification of cathode channel flooding in PEM fuel cells. Journal of Power Sources *187*, 444-451. https://doi.org/10.1016/j.jpowsour.2008.11.030.
16. He, W., Lin, G., and Van Nguyen, T. (2003). Diagnostic tool to detect electrode flooding in proton-exchange-membrane fuel cells. AlChE J. *49*, 3221-3228. https://doi.org/10.1002/aic.690491221.
17. Liu, X., Guo, H., Ye, F., and Ma, C.F. (2007). Water flooding and pressure drop characteristics in flow channels of proton exchange membrane fuel cells. Electrochimica Acta *52*, 3607-3614. https://doi.org/10.1016/j.electacta.2006.10.030.
18. Shafaque, H.W., Lee, J.K., Krause, K., Lee, C., Fahy, K.F., Shrestha, P., Balakrishnan, M., and Bazylak, A. (2021). Temperature enhances the ohmic and mass transport behaviour in membrane electrode assembly carbon dioxide electrolyzers. Energy Conversion and Management *243*, 114302. https://doi.org/10.1016/j.enconman.2021.114302.
19. Krause, K., Lee, C., Lee, J.K., Fahy, K.F., Shafaque, H.W., Kim, P.J., Shrestha, P., and Bazylak, A. (2021). Unstable Cathode Potential in Alkaline Flow Cells for CO_2 Electroreduction Driven by Gas Evolution. ACS Sustainable Chemistry & Engineering *9*, 5570-5579. 10.1021/acssuschemeng.0c08993.
20. Endrődi, B., Samu, A., Kecsenovity, E., Halmágyi, T., Sebők, D., and Janáky, C. (2021). Operando cathode activation with alkali metal cations for high current density operation of water-fed zero-gap carbon dioxide electrolysers. Nature Energy *6*, 439-448. 10.1038/s41560-021-00813-w.
21. Mardle, P., Cassegrain, S., Habibzadeh, F., Shi, Z., and Holdcroft, S. (2021). Carbonate Ion Crossover in Zero-Gap, KOH Anolyte CO_2 Electrolysis. The Journal of Physical Chemistry C *125*, 25446-25454. 10.1021/acs.jpcc.1c08430.
22. Endrődi, B., Kecsenovity, E., Samu, A., Darvas, F., Jones, R.V., Török, V., Danyi, A., and Janáky, C. (2019). Multilayer Electrolyzer Stack Converts Carbon Dioxide to Gas Products at High Pressure with High Efficiency. ACS Energy Letters *4*, 1770-1777. 10.1021/acsenergylett.9b01142.
23. Xu, Y., Edwards, J.P., Liu, S., Miao, R.K., Huang, J.E., Gabardo, C.M., O'Brien, C.P., Li, J., Sargent, E.H., and Sinton, D. (2021). Self-Cleaning CO_2 Reduction Systems: Unsteady Electrochemical Forcing Enables Stability. ACS Energy Letters *6*, 809-815. 10.1021/acsenergylett.0c02401.
24. Endrődi, B., Kecsenovity, E., Samu, A., Halmágyi, T., Rojas-Carbonell, S., Wang, L., Yan, Y., and Janáky, C. (2020). High carbonate ion conductance of a robust PiperION membrane allows industrial current density and conversion in a zero-gap carbon dioxide electrolyzer cell. Energy & Environmental Science *13*, 4098-4105. 10.1039/D0EE02589E.

25. Dinh, C.-T., Burdyny, T., Kibria, M.G., Seifitokaldani, A., Gabardo, C.M., Arquer, F.P.G.d., Kiani, A., Edwards, J.P., Luna, P.D., Bushuyev, O.S., et al. (2018). CO_2 electroreduction to ethylene via hydroxide-mediated copper catalysis at an abrupt interface. Science *360*, 783-787. doi:10.1126/science.aas9100.
26. Kutz, R.B., Chen, Q., Yang, H., Sajjad, S.D., Liu, Z., and Masel, I.R. (2017). Sustainion Imidazolium-Functionalized Polymers for Carbon Dioxide Electrolysis. Energy Technology *5*, 929-936. https://doi.org/10.1002/ente.201600636.
27. Choi, W., Park, S., Jung, W., Won, D.H., Na, J., and Hwang, Y.J. (2022). Origin of Hydrogen Incorporated into Ethylene during Electrochemical CO_2 Reduction in Membrane Electrode Assembly. ACS Energy Letters *7*, 939-945. 10.1021/acsenergylett.1c02658.
28. Garg, S., Rodriguez, C.A.G., Rufford, T.E., Varcoe, J., and Seger, B. (2022 (just accepted)). How membrane characteristics influence the performance of CO_2 and CO electrolysis. Energy & Environmental Science.
29. Larrazábal, G.O., Okatenko, V., Chorkendorff, I., Buonsanti, R., and Seger, B. (2022). Investigation of Ethylene and Propylene Production from CO_2 Reduction over Copper Nanocubes in an MEA-Type Electrolyzer. ACS Applied Materials & Interfaces *14*, 7779-7787. 10.1021/acsami.1c18856.
30. Moss, A., Hätinen, J., Kúš, P., Garg, S., Mirolo, M., Chorkendorff, I., Seger, B., and Drnec, J. (2022). Versatile X-ray operando electrolysis cell. ChemRxiv. 10.26434/chemrxiv-2022-7v75p.
31. Martens, I., Vamvakeros, A., Chattot, R., Blanco, M.V., Rasola, M., Pusa, J., Jacques, S.D.M., Bizzotto, D., Wilkinson, D.P., Ruffmann, B., et al. (2019). X-ray transparent proton-exchange membrane fuel cell design for in situ wide and small angle scattering tomography. Journal of Power Sources *437*, 226906. https://doi.org/10.1016/j.jpowsour.2019.226906.
32. Martens, I., Vamvakeros, A., Martinez, N., Chattot, R., Pusa, J., Blanco, M.V., Fisher, E.A., Asset, T., Escribano, S., Micoud, F., et al. (2021). Imaging Heterogeneous Electrocatalyst Stability and Decoupling Degradation Mechanisms in Operating Hydrogen Fuel Cells. ACS Energy Letters *6*, 2742-2749. 10.1021/acsenergylett.1c00718.
33. Martens, I., Chattot, R., Wiegmann, T., Fuchs, T., Magnussen, O.M., Dubau, L., Maillard, F., and Drnec, J. (2021). Towards comprehensive understanding of proton-exchange membrane fuel cells using high energy x-rays. Journal of Physics: Energy *3*, 031003. 10.1088/2515-7655/abf43d.
34. Schweiss, R., Hofmeister, S., Meiser, C., Dan, D., Baumann, A., Kuster, T., Haak, N., and Bacher, S. Powering up fuel cells (Sigracet). https://www.sglcarbon.com/pdf/SIGRACET-Whitepaper.pdf.
35. Schweiss, R., Meiser, C., Damjanovic, T., Galbati, I., and Haak, N. SIGRACET® Gas Diffusion Layers for PEM Fuel Cells, Electrolyzers and Batteries. https://www.fuelcellstore.com/spec-sheets/sigracet-gdl-white-paper-new-generation.pdf.
36. Burdyny, T., and Smith, W.A. (2019). CO_2 reduction on gas-diffusion electrodes and why catalytic performance must be assessed at commercially-relevant conditions. Energy & Environmental Science *12*, 1442-1453. 10.1039/C8EE03134G.
37. Cave, E.R., Shi, C., Kuhl, K.P., Hatsukade, T., Abram, D.N., Hahn, C., Chan, K., and Jaramillo, T.F. (2018). Trends in the Catalytic Activity of Hydrogen Evolution during CO_2 Electroreduction on Transition Metals. ACS Catalysis *8*, 3035-3040. 10.1021/acscatal.7b03807.
38. Marcandalli, G., Villalba, M., and Koper, M.T.M. (2021). The Importance of Acid–Base Equilibria in Bicarbonate Electrolytes for CO_2 Electrochemical Reduction and CO Reoxidation Studied on Au(*hkl*) Electrodes. Langmuir *37*, 5707-5716. 10.1021/acs.langmuir.1c00703.
39. Resasco, J., Lum, Y., Clark, E., Zeledon, J.Z., and Bell, A.T. (2018). Effects of Anion Identity and Concentration on Electrochemical Reduction of CO_2. ChemElectroChem *5*, 1064-1072. https://doi.org/10.1002/celc.201701316.
40. Liu, Z., Yang, H., Kutz, R., and Masel, R.I. (2018). CO_2 Electrolysis to CO and O_2 at High Selectivity, Stability and Efficiency Using Sustainion Membranes. Journal of The Electrochemical Society *165*, J3371-J3377. 10.1149/2.0501815jes.

41. Larrazábal, G.O., Ma, M., and Seger, B. (2021). A Comprehensive Approach to Investigate CO_2 Reduction Electrocatalysts at High Current Densities. Accounts of Materials Research *2*, 220-229. 10.1021/accountsmr.1c00004.
42. Weng, L.-C., Bell, A.T., and Weber, A.Z. (2019). Towards membrane-electrode assembly systems for CO_2 reduction: a modeling study. Energy & Environmental Science *12*, 1950-1968. 10.1039/C9EE00909D.
43. Lide, D.R. (2007). CRC Handbook of Chemistry and Physics (CRC press).
44. Luo, X., Rojas-Carbonell, S., Yan, Y., and Kusoglu, A. (2020). Structure-transport relationships of poly(aryl piperidinium) anion-exchange membranes: Effect of anions and hydration. Journal of Membrane Science *598*, 117680. https://doi.org/10.1016/j.memsci.2019.117680.
45. Ashiotis, G., Deschildre, A., Nawaz, Z., Wright, J.P., Karkoulis, D., Picca, F.E., and Kieffer, J. (2015). The fast azimuthal integration Python library: pyFAI. J. Appl. Crystallogr. *48*, 510-519. https://doi.org/10.1107/S1600576715004306.
46. Toby, B.H., and Dreele, R.B.V. (2013). GSAS-II: the genesis of a modern open-source all purpose crystallography software package. J. Appl. Crystallogr. *46*, 544-549. https://doi.org/10.1107/S0021889813003531.